ELECTRICAL AND OPTICAL CHARACTERIZATION OF NANOSCALE MATERIALS FOR ELECTRONICS

A Dissertation

by

CHI-YUAN CHANG

Submitted to the Office of Graduate Studies of
Texas A&M University
in partial fulfillment of the requirements for the degree of

DOCTOR OF PHILOSOPHY

Approved by:

Chair of Committee,	James D. Batteas
Committee Members,	Dong Hee Son
	Hong Liang
	Paul S Cremer
Head of Department,	David H. Russell

December 2012

Major Subject: Chemistry

Copyright 2012 Chi-Yuan Chang

ABSTRACT

Due to a lack of fundamental knowledge about the role of molecular structures in molecular electronic devices, this research is focused on the development of instruments to understand the relation between device design and the electronic properties of electroactive components. The overall goal is to apply this insight to obtain a more efficient and reliable scheme and greater functional control over each component. This work developed a fabrication method for porphyrinoids on graphene-based field effect transistors (FETs), and a chemical sensing platform under an ambient environment by integrating a tip-enhanced Raman spectroscope (TERS), atomic force microscope (AFM), and electronic testing circuit.

The study is divided into three aspects. The first is aimed at demonstrating fabrication processes of nanoscale FETs of graphene and porphyrinoid composites based entirely on scanning probe lithography (SPL). A nanoshaving mechanism was used to define patterns on octadecanethiol self-assembled monolayers on gold film evaporated on graphene flakes, followed by metal wet etching and/or oxygen plasma etching to develop patterns on Au films and graphene, respectively. The integrity and optoelectronic properties were examined to validate the processes.

The second area of study focused on the development of the chemical sensing platform, enabling chemical changes to be monitored during charge transports under an ambient environment. The localized Raman enhancement was induced by exciting surface plasmon resonance in nanoscale silver enhancing probes made by thermal silver

evaporation on sharp AFM tips. As the system was designed along an off-axis illumination/collection scheme, it was demonstrated that it was capable of observing molecular decomposition on opaque and conductive substrates induced by an electric bias.

The third line of work proposed a novel TERS system and a probe preparation method. Silver nanowires mounted on AFM tips were used to locally enhance the Raman scattering. The observed Raman enhancement allows quick chemical analysis from a nanoscale region, and thus enables chemical mapping beyond the diffraction limit. Compared with other TERS geometries, the new optical design not only allows analysis on large or opaque samples, but also simplifies the design of the optical components and the alignment processes of the setup.

DEDICATION

To my parent and wife, who have always been there to support and encourage me.

TABLE OF CONTENTS

Page

ABSTRACT ii

DEDICATION iv

TABLE OF CONTENTS v

LIST OF FIGURES vii

LIST OF TABLES xi

CHAPTER I INTRODUCTION 1

1.1 Tip-enhanced Raman spectroscopy 5
1.2 The TERS mechanism 10
1.3 TERS instrumental arrangement 13
1.4 Graphene in nanoelectronics 15
1.5 AFM nanolithography 21
1.6 Summary 24

CHAPTER II EXPERIMENTAL METHODS 27

2.1 AFM 27
2.2 Confocal microscopy 29
2.3 Nanoshaving lithography 31
2.4 Electrical measurement 34

CHAPTER III PATTERNING OF GRAPHENE FIELD EFFECT TRANSISTORS BY SCANNING PROBE LITHOGRAPHY 38

3.1 Introduction 38
3.2 Methods 40
3.3 Results and discussion 41
3.4 Conclusion 57

Page

CHAPTER IV IN SITU MONITORING PLATFORM FOR NANOLITHOGRAPHY ON CONDUCTING PROBE ATOMIC FORCE MICROSCOPE COUPLED WITH TIP-ENHANCED RAMAN SPECTROSCOPY 59

4.1 Introduction 59
4.2 Experimental 62
4.3 Results and discussion 65
4.4 Conclusion 79

CHAPTER V NOVEL AND EASY-TO-USE TIP-ENHANCED RAMAN SPECTROSCOPY ON OPAQUE SUBSTRATES WITH A MICRO-SIZED MIRROR AND A SILVER-NANOWIRE TIP 80

5.1 Introduction 80
5.2 Experimental 82
5.3 Results and discussion 87
5.4 Conclusion 102

CHAPTER VI CONCLUSIONS AND OUTLOOK 103

REFERENCES 109

APPENDIX A 119

APPENDIX B 127

LIST OF FIGURES

FIGURE Page

1 Increasing number of transistors in a chip as predicted by Moore's Law.. 2

2 Length and time scale diagram between optical spectroscopy and scanning probe microscopy 6

3 Scanning on brilliant cresyl blue molecules adsorbed on Au (111) sample: (a) STM image, (b) topography profile along the arrow in (a), and (c) TERS intensity profile along the arrow in (a) 9

4 Processes of Raman and Rayleigh scattering 11

5 Electric field simulation of a gold tip placed next to a gold substrate surface at a distance of 2 nm 13

6 TERS instrumental arrangement: (a) side illumination, (b) bottom illumination, and (c) parabolic mirror illumination........ 14

7 Atomic arrangement of graphene 18

8 Graphene transistor: (a) resistivity altered by gate bias and (b) typical structure of a graphene transistor 20

9 AFM-based nanolithography: (a) dip-pen (b) nanogragrafting, and (c) nanoshaving 23

10 Principle of AFM operation: (a) normal force deflection, and (b) lateral force deflection 28

11 Schematic illustration of a confocal microscopy set up 32

12 Instrumental setup for nanoshaving nanolithography 34

13 Wire connection of electrical measurement: (a) on a probe station and (b) of equivalent electric circuit 36

Page

14 Schematic of the fabrication process for creating a graphene FET by AFM-based nanolithography: (a) deposition of graphene on an oxidized Si wafer, (b) deposition of Au on top of the graphene layer, (c) formation of an ODT SAM on the Au thin film, (d) patterning the ODT SAM by AFM nanoshaving, (e) transferring the ODT pattern onto the Au layer, (f) transferring the pattern further onto the graphene layer, (g) removal of the Au thin film, and (h) formation of electrode contacts by repeating the steps (b)~(g) 43

15 Optical and AFM images of graphene coated with Au/Cr layers: (a) optical microscope image of a graphene flake, (b) optical microscope image of the graphene flake coated with Au/Cr layers, (c) AFM topographic image of the graphene flake coated with Au/Cr layers and color scale, and (d) corrugated blisters in Au/Cr layers formed under very large tensile stress 45

16 Examples of patterned Au masks and graphene: (a) AFM topographic image of Au stripes used as a mask for graphene etching, (b) AFM friction image of graphene stripe underneath the Au stripes, and (c) cross-sectional profile along the white solid line in (b) 47

17 Images of markers and defects during etching: (a) scheme for triangulation locating method, (b) optical picture of markers with various sizes, (c) AFM topographic image of cured marker coated with Au/Cr, and (d) optical picture of defect formation when the graphene target was scanned without using markers 49

18 Raman spectra of (a) multilayer graphene, and (b) protected single-layer graphene before (black line) and after (red line) treatment of oxygen plasma 51

19 Characterization of graphene transistor: (a) AFM topographic image with false color, where the labels, Au and SiO2, indicate Au and oxidized Si wafer, respectively; (b) Raman mapping of graphene G band, where the white dash lines and blue dot lines indicate the edges of the gold electrodes and the graphene flake, respectively...................... 53

20 Electrical measuremnets of graphene transistor: (a) curve of source-to-drain current at various source-to-drain bias with a gate bias of 0 V, and (b) fitting curve of total resistance at various gate bias with a source-to-drain bias of 0.1 V 55

Page

21 Photo-gating current of porphyrin-graphene composite FET 57

22 Instrumental setup for the combination of conductive-probe AFM and TERS 63

23 Tip and sample characterization: (a) SEM picture of a silver-coated tip (inset: zoom-in picture near the tip apex), (b) AFM picture of MLG on Si (the spots A, B, and C indicate the positions for the AFM nanolithography), (c) AFM picture of Ag film on glass, (d) AFM picture of the sample in (c) spin-coated with R6G, and (e) AFM picture of MBA SAM on Au film 67

24 Raman spectra of MLG on Si wafer (red line), R6G on Agfilm (green line), and MBA on Ag film (blue line).. 69

25 TERS (red line) and Raman spectra without tip enhancement (blue line) of MLG on Si, R6G on Ag, and MBA SAM on Au 71

26 Bias on/off ratio of TERS intensity of (a) MLG on Si wafer, R6G on Ag film, and MBA on Ag film, and (b) R6G on Ag film over various biases applied between the tip and the Ag film.. 76

27 Sample characterization: (a) AFM topographic image of MLG on Si wafer after several nanolithographic steps (the spots A, B, and C indicate the positions for the AFM nanolithography.), (b) cross-sectional profile in the spot A in (a), (c) AFM friction image of MBA SAM on Au film before nanolithography, and (d) AFM friction image of MBA SAM on Au film after nanolithography 77

28 (a) Instrumental setup under objective lens, and (b) optical picture of the setup... 84

29 Optical images of a tip, a micro-sized mirror, and a sample under (a) white light illumination, and (b) laser illumination.................................... 85

30 (a) UV-Vis spectrum of silver nanowires suspended in aqueous solution, and (b) silver nanowires deposited on a filter 88

Page

31 Optical microscopic pictures of nanowire attachment: (a) a sharp and a blunt AFM tip, (b) a tip dipped into a thin layer of glue, (c) a tip coated with a small amount of glue, (d) a silver nanowire in contact with a tip pre-coated with glue, (e) a silver nanowire transferred on a tip, and (f) a silver nanowire fixed on a tip after adjustment 90

32 (a) AFM scanning on a calibration standard by a nanowire, and (b) its cross-sectional profile across the highest point.. 91

33 SEM pictures of a nanowire fixed on (a) a new tip, and (b) an old tip recycled several times 93

34 Raman spectra of R6g on silver film (a) at high spectral resolution, and (b) at a reduced resolution with and without tip enhancement............ 95

35 Raman spectra of R6g on silver film and on glass 97

36 Beam profile of a focused laser.. 98

37 (a) Lateral force image of R6g on silver film, (b) topographic image of R6g on silver film, (c) lateral force image of R6g on silver film after local oxidation nanolithography, and (d) topographic image of R6g on silver film after local oxidation nanolithography 100

38 (a) Confocal Raman line-scanning across the nanolithographic region, and (b) tip-enhanced Raman line-scanning across the same region........... 102

LIST OF TABLES

TABLE Page

1 Physical properties of graphene ... 18

2 Raman assignment of MLG on Si, R6G on Ag, and MBA on Ag ... 68

3 Tip enhancement calculation of MLG on Si, R6G on Ag, and MBA SAM on Au ... 73

CHAPTER I

INTRODUCTION

Pursuing better functionality, performance and lower cost has always been one of the goals of the semiconductor industry. Popularly known as Moore's Law, the number of transistors in a chip is predicted to approximately double every 24 months, as shown in Figure 1. This is achieved by reducing the sizes of the basic units in devices, offering the advantage of higher density, better performance, and lower power consumption. In past decades, Moore's law has described progress in the semiconductor industry relatively well,[1] but now the limit of the law is being reached. The ultimate limit of the law requires miniaturization near atomic levels at extremely high cost, with a new range of challenges emerging in terms of high-volume production, heat dissipation, new materials and lithographic integration.[2,3] Therefore, the escalating cost of product fabrication and relative equipment investment motivates investigation into alternative processes to extend Moore's prediction, including molecular-based electronics. One of the most obvious advantages is the scale of the molecules, ranging from 1 to 100 nm. A larger and more complex architecture can be formed by the design of specific intermolecular interactions by means of self-assembly and molecular recognition.[4] Due to the nature of molecules, they may have multiple stable and switchable states in 3-dimensional structures and oxidation states. Their properties can be used for transducing one energy form into another, and memorizing a piece of information in the applications of sensors,[5] transistors,[6,7] memory,[8] etc. In addition, there is the major advantage of the

ability to synthetically tailor molecules, which has been highly developed especially in organic and inorganic chemistry.[2,4] By the design of molecular composition and geometry, the properties of a molecule may be controlled to exhibit desired functions responding to external stimuli, such as light, electric potential and current, chemical environment, etc.

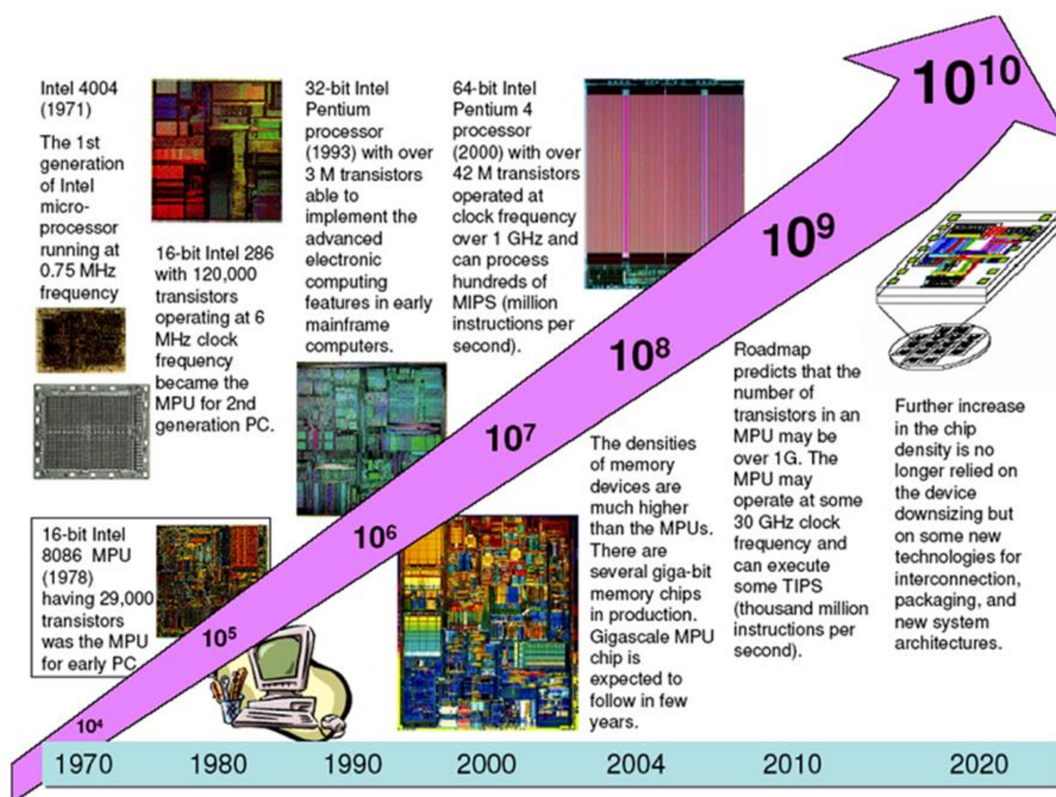

Figure 1. Increasing number of transistors in a chip as predicted by Moore's Law. Reprinted from ref. [9] with permission of Copyright (2007) from Elsevier.

Molecular assembly has great potential due to its ability to assemble structures in a controlled fashion. Unique processes arrange molecules into higher-order architectures with or without external guidance, due to the interaction between the molecules and the external control.[10-12] Self-assembled monolayers (SAMs) are an excellent example of a basic molecular assembly, in which a layer of molecules is reversibly chemisorbed onto a substrate, lowering the surface free-energy of the substrate. SAMs are an inexpensive and versatile surface modification technique widely used in applications for biology,[13,14] electrochemistry,[15,16] and material science.[17,18] Patterned SAMs are also useful as a base for building or controlling more complex structures, such as confining foreign molecules in the SAM matrix,[19] trapping and releasing cells,[20] etc. Fully understanding the processes in controlled molecular assembly provides valuable guidance to realize the techniques in practical applications.

There are still some issues in the field of molecular electronics that need to be overcome; specifically one important issue is maintaining the stability of a molecular device in demanding conditions.[21] This includes the stability of structures under operational conditions over time, and stable molecular contact with the electrodes. However, it is still a challenge to consistently create a junction with high carrier injection efficiency and excellent interface properties. A small difference in the fabrication technique leads to relatively large variations in the junction's properties, even when the same molecules and electrodes are used. Harsh conditions including high temperature, high current density, and a high electric field may cause a device to become unstable or even fail, due to accumulated energy inducing chemical changes in materials,

such as with oxidation reactions,[22] geometry switching,[23] or bond breaking.[24] Thus, understanding energy and charge transport in molecular junctions in a solid-state device environment, and the corresponding change introduced to the molecules is critical, and the information may provide crucial guidance to model molecular behavior and to develop reliable and multifunctional molecular-based devices.[25] In order to address this, lithography with controlled molecular assembly is helpful for determining practical fabrication approaches.

This also leads to a demand for developing tools for observing molecular behavior during operation and fabrication processes. Many analytical systems, such as scanning probe microscopy and electron microscopy, provide useful information about molecular devices, but these techniques are mostly performed after a certain change is introduced to the devices, and thus do not provide the chemical detail during the modification.[26] Therefore, monitoring ability during operation is limited. Inelastic electron tunneling spectroscopy combined with scanning tunneling microscopy can obtain vibrational spectra for the identification of analytes.[27] However, the requirement for current measurements at a cryogenic temperature in an ultrahigh vacuum may not reflect the same behavior of a molecular junction under ambient conditions, and is even intrinsically incompatible with some electronic operations. Several approaches, including infrared absorption, sum frequency generation, and high-resolution electron energy loss spectroscopy, have been proposed to characterize the chemical species on a sample surface,[28,29] but with these methods, resolving chemical composition on the nanoscale under ambient conditions remains a challenge.

1.1 Tip-enhanced Raman spectroscopy

Tip-enhanced Raman spectroscopy (TERS) is a potential candidate for the detection of changes in molecular structure during charge transport and fabrication processes with high sensitivity[30-32] and high spatial resolution,[33-35] in a vacuum, under ambient conditions, or even in a liquid environment[36], without any special sample treatment. Raman spectroscopy provides details of the vibrational states of the analyte molecules, which provides the information to identify these molecules and their chemical or physical changes, and importantly it is an optical technique that can be implemented under a suitable environment in a non-destructive fashion. Traditional Raman spectroscopy is limited by its low sensitivity and optical diffraction limit. Thus, an analysis of Raman spectroscopy is performed over an average of an ensemble or bulk collection of molecules on the micrometer scale. With the tip enhancement technique, Raman spectroscopy is able to overcome the weak sensitivity, producing information down to a single molecule level.[31] The enhancement is tightly confined near the tip apex, which improves the spatial resolution beyond the diffraction limit and the detection limit. In addition, the extension into the time domain may also be enabled by combining it with ultrafast pulses.[37] The strength of TERS is further increased by the integration of optical spectroscopy and scanning probe microscopy, so that information about nanoscale surface topography is simultaneously obtained. Figure 2 shows the comparison of the typical length and time scale between optical spectroscopy and scanning probe microscopy.

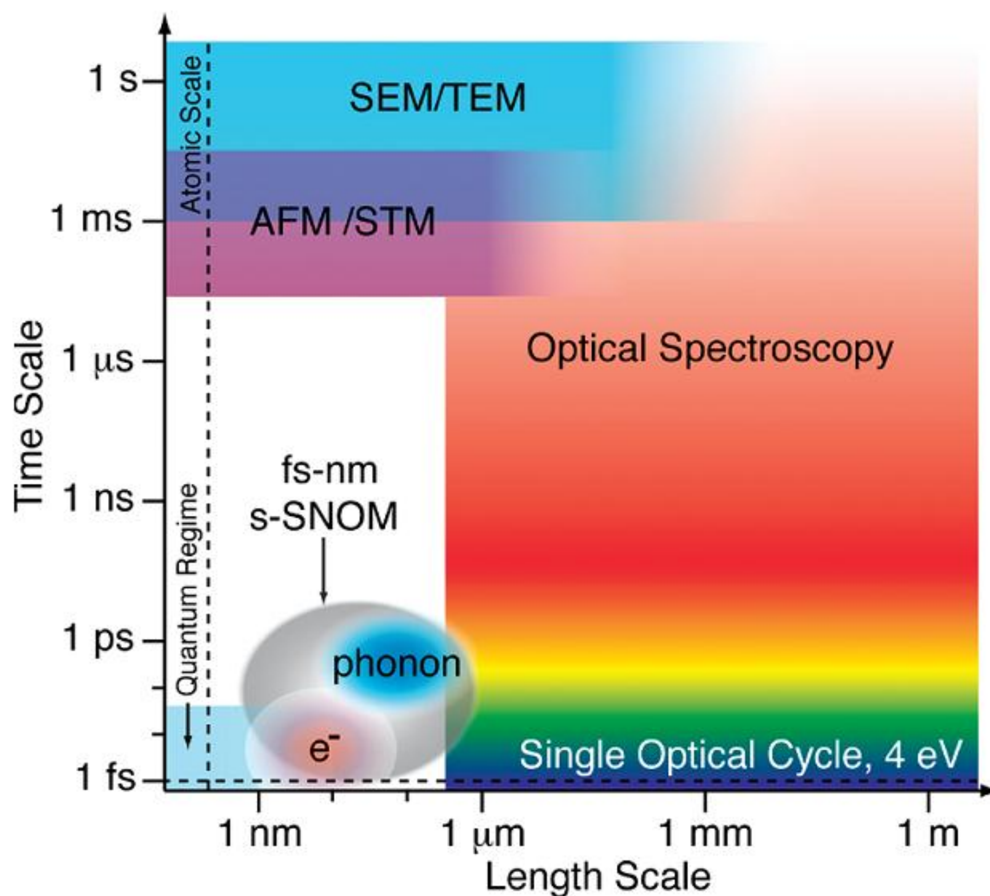

Figure 2. Length and time scale diagram between optical spectroscopy and scanning probe microscopy. Reprinted from ref. [37] with permission of Copyright (2012) from American Chemical Society.

Among the scanning probe microscopic methods, atomic force microscope (AFM) and scanning tunneling microscope (STM) are used to maintain a suitable distance between the tip and sample.[38-40] Of the two, AFM is frequently employed due to its compatibility with both conductive and nonconductive samples. AFM mainly relies on force feedbacks to control the tip-sample distance, and can function in contact,

tapping, and shear force modes. In AFM contact mode operation, a TERS tip is in direct contact with the sample, which gives a relatively stronger enhancement, but also increases the chances of tip contamination from samples.[41] For the AFM tapping mode, a tip is driven to vibrate at its resonance frequency and an averaged tip-sample distance is maintained.[42] The distance oscillation may be used to modulate the Raman enhancement for the signal filtration in the far field. For the shear force mode, the feedback from a tuning fork is used to maintain a small tip-sample distance.[43] STM, although limited to conductive materials, is a very sensitive technique that works by detecting a tunneling current through tip-sample gap to maintain the gap separation in a precisely controlled manner,[31] with the added benefit of the separation preventing tips from contaminating the sample.

The major methods to prepare TERS tips include electrochemical etching and vapor deposition. Electrochemical etching yields consistent TERS tips with a sharp apex [31,44] by having a thin metallic wire acting as an anode inserted in a ring cathode. This type of tip is generally used in STM and shear force mode AFM. For AFM taping and contact modes, TERS tips are typically prepared by coating a metallic thin film through vapor deposition. However, the coating stability and TERS reproducibility are still issues in this process due to the difficulty of controlling the deposition near the tip apex.[38,45]

The TERS applications are quickly expanding in the fields of biology, chemistry, material science, and physics. Due to label-free optical detection and the compatibility with ambient conditions, TERS provides the highly coveted insight into the structure, composition, and distribution in a non-destructive manner. TERS has been successfully

applied on probing biological molecules and interfaces, such as RNA,[30] DNA,[46] collagen,[47] cell walls,[48] viruses,[49] mitochondria,[50] and bacteria.[51] To monitor biological and biochemical processes, TERS still needs to overcome some challenges. When dealing with molecules of low Raman cross-section, a moderate enhancement is generally insufficient. However, strong enhancement or laser excitation may cause photo-degradation issues.[52] For example, many degraded products of biological molecules show Raman features similar to amorphous carbon, which may fluctuate in Raman shifts and intensities. The other critical issue in TERS is the prevention of tip contamination. Free of the problem mentioned above, TERS is an ideal approach to study solid materials. It has been demonstrated on various examples, such as strained silicon[53], silicon carbide,[54] gallium nitride nanowires,[34] carbon nanotubes,[55] graphene,[56] and with surface adsorbates.[57] The physical and chemical properties obtained from TERS allow nanoscale recognition of stress, crystal orientation and domain, as well as surface defects. This atomic and molecular arrangement may also be determined by X-ray and electron diffraction, but TERS does not suffer from low spatial resolution and radiation damage.

Many efforts were contributed in proving TERS sensitivity down to the single molecule level. In the field of surface-enhanced Raman spectroscopy (SERS), the detection of single molecules was indicated indirectly by statistics, spectral fluctuations of Raman signals and low analyte concentrations. In contrast, the imaging capability of TERS provides direct evidence to locate and identify analytes. In addition, molecular absorption on a flat surface can be better controlled than on the rough or aggregated

surface required in SERS. As shown in Figure 3, Steidtner and Pettinger[58] reported the high-resolution and sensitivity of brilliant cresyl blue chemisorbed on a gold surface in ultrahigh vacuum conditions, where the vacuum prevented the photooxidation of the analyte over a reasonably long period of time.

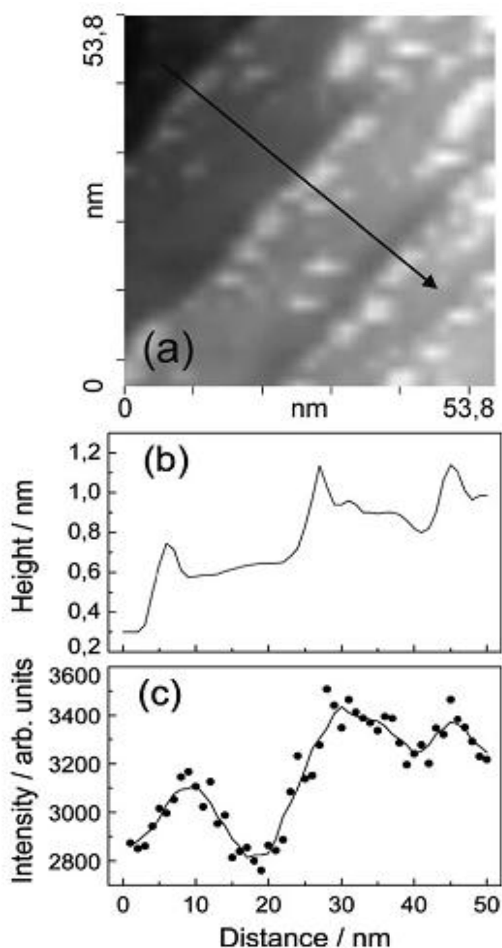

Figure 3. Scanning on brilliant cresyl blue molecules adsorbed on Au (111) sample: (a) STM image, (b) topography profile along the arrow in (a), and (c) TERS intensity profile along the arrow in (a). Reprinted from ref. [58] with permission of Copyright (2008) from American Physical Society.

1.2 The TERS mechanism

Raman scattering refers to a process in which the energies of the incident electromagnetic waves are changed upon interacting with matter, as shown in Figure 4. The process involves the absorption of incident photons and their subsequent emission from a material: the former excites the material from an initial quantum state to an intermediate state, and the latter relaxes the intermediate state to a final state. The energy difference corresponds to a transition between the initial and final states of the material, where a negative difference, labeled the Stokes Raman shift, is caused by exciting the material into a higher energy level, while the anti-Stokes Raman shift ends up at a lower level. As such, the shift in energy gives a chemical and physical fingerprint for material identification and analysis. The information is similar but complementary to that from infrared spectroscopy, due to their different selection rules. However, the Raman effect is extremely weak. A very small fraction of incident photons is inelastically scattered, which is often overshadowed by elastic Rayleigh scattering and fluorescence. Triple monochromators or optical filters are frequently utilized to remove Rayleigh scattering, and laser systems in the red and infrared range may mitigate the fluorescence problem.

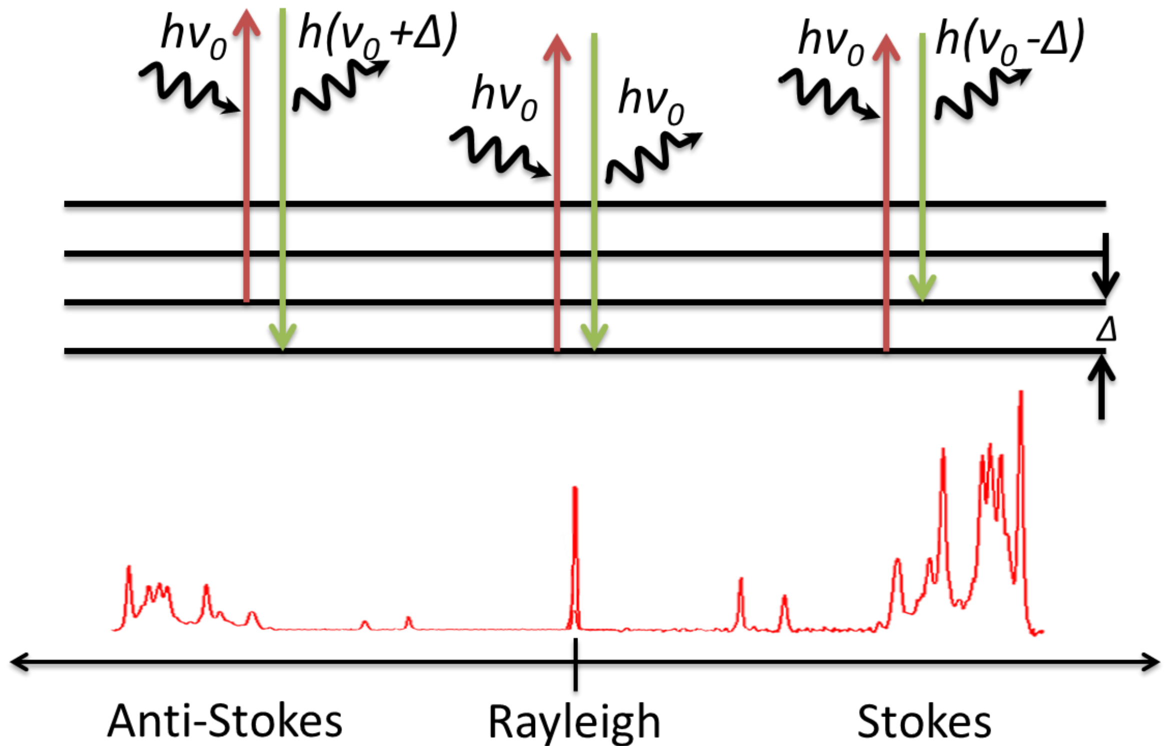

Figure 4. Processes of Raman and Rayleigh scattering.

The weak Raman effects can be greatly enhanced when a sharp metallic tip apex is brought in close proximity to the analyte of interest.[58] The enhancement for TERS is explained by the mechanisms of the electromagnetic enhancement and chemical enhancement.[38] The former mechanism, responsible for most of the enhancement, is correlated with the excitation of localized surface plasmons within the metal structures on the nanometer scale. These collective electron oscillations in the nanostructures additionally create a localized electromagnetic field with a much stronger field strength compared to its excitation field strength. The field enhancement is maximized when the

plasmon is in resonance with the excitation light. Silver and gold are widely used for tip materials due to their resonance frequencies, and their relatively smaller absorption at the resonance frequencies causes less damping of their plasmons leading to higher enhancement efficiencies. The spectral width of plasmon resonance is often larger than that of the Stokes shift in a typical Raman spectrum, and as such the enhancement mechanism works on the both fields of incident light and scattering. In other words, Raman processes close to the metallic tip apex may be greatly enhanced. The confined enhancement is shown in Figure 5. On the other hand, chemical enhancement refers to the process of charge transfer, occurring in direct contact between a metallic tip and analytes, which creates additional pathways and thus increases the scattering probability. Moreover, in principle both mechanisms confine the enhancement phenomenon to the close proximity of a metallic tip apex, which gives rise to the high sensitivity and high spatial resolution of TERS.

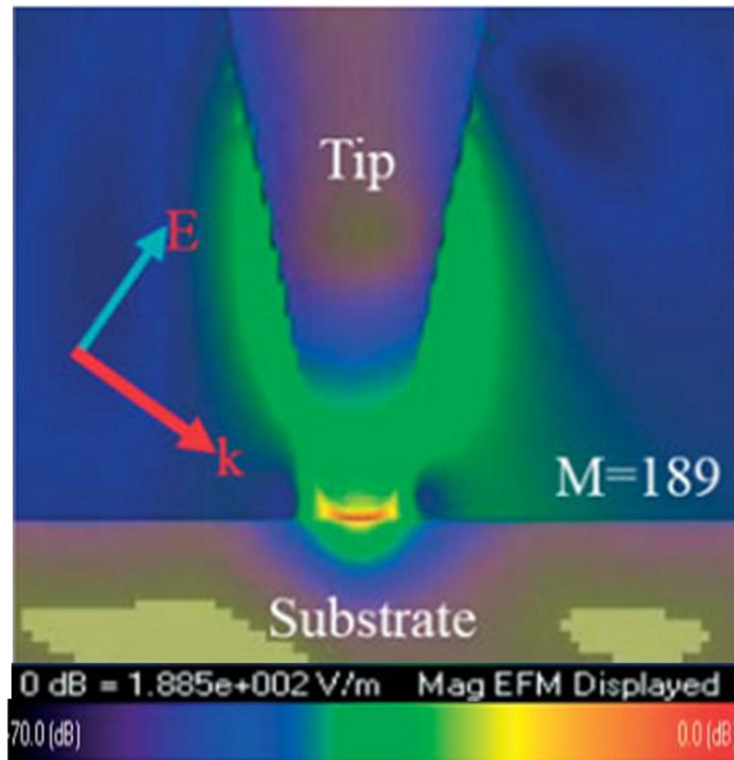

Figure 5. Electric field simulation of a gold tip placed next to a gold substrate surface at a distance of 2 nm. Reprinted from ref. [59] with permission of Copyright (2009) from John Wiley and Sons.

1.3 TERS instrumental arrangement

There are three major designs of the TERS instrumental arrangement, depicted in Figure 6, based on the angle between the TERS tip and the incident laser illumination with: 1) bottom illumination;[60,61] 2) side illumination;[62,63] and 3) parabolic mirror illumination.[64,65] In the bottom illumination setup, the laser is tightly focused on the tip through a transparent sample by a high numerical-aperture (NA) objective of an inverted microscope with a very short working distance. The geometry maximizes the signal

collection efficiencies due to its wide collecting solid angles. The p-polarization of the incident laser may be created by the high NA objective, especially when a radially distributed polarization in the laser beam is introduced. The small laser focus is another advantage due to the reduction of the background signal from the direct laser excitation.

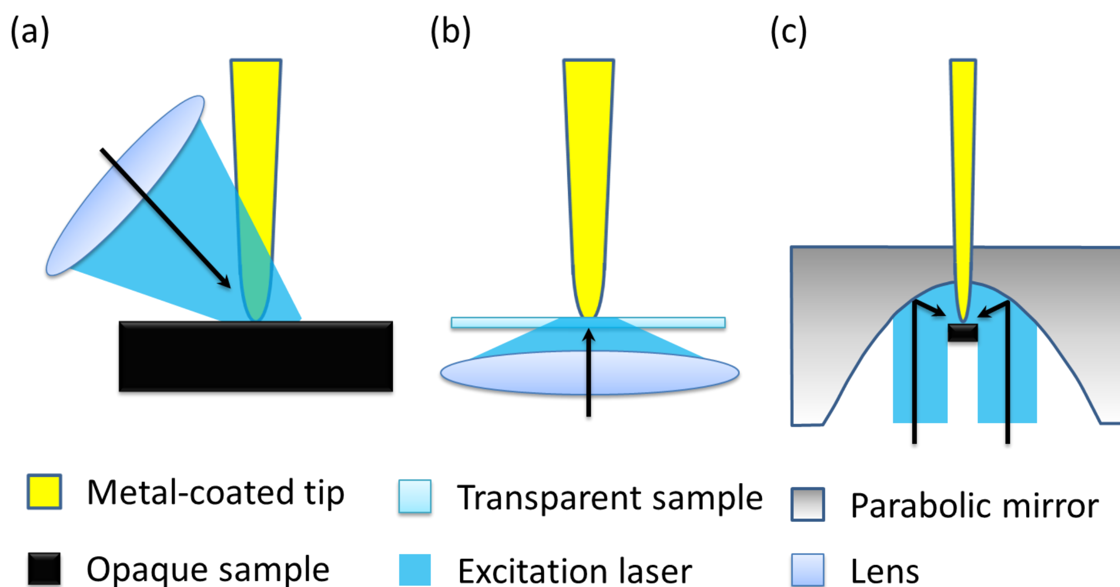

Figure 6. TERS instrumental arrangement: (a) side illumination, (b) bottom illumination, and (c) parabolic mirror illumination. The arrows indicate the direction of illumination.

The side illumination set up has a long-working-distance objective with a moderate NA that is generally used to excite the tip from the side with an angle of 40–60º relative to the tip axis. This also leads to advantages, as now an opaque sample may

be studied and the polarization of the incident laser can be aligned to the tip without any excess optical component changing the polarization distribution in the beam. However, the laser focus is relatively large due to the tilted focusing angle and the limited NA.

For parabolic mirror illumination, a collimated laser beam with a large diameter is brought into focus with a parabolic mirror from the bottom of the sample, and tightly focused to the tip-sample junction by reflection. Similar to bottom illumination, p-polarization is achieved by focusing a radially polarized beam. Parabolic mirror illumination has the advantage that a change in refractive index of the local media does not affect its focal position and that it has a high NA and tight focus.

Several limitations exist in the TERS instrumental arrangements. In the bottom illumination setup, sample transparency is required and the sample thickness is limited to within the working distance of the objective in use. In the side illumination configuration, sample dimensions are limited to the available space between the tip and the objective. For parabolic mirror illumination, lateral dimensions of samples have to be much smaller than the laser beam size, to minimize blockage of the laser and its scattered signal. In addition to the specific requirements, the complexity of all these arrangements increases the difficulty in the alignment process between all the components.

1.4 Graphene in nanoelectronics

Electron transport in molecular devices is mainly controlled by structural design, molecular junctions, and the surrounding environment. Investigations of the electronic characteristics have been performed extensively on either STM or electrode-molecule-

electrode geometries. In STM, the molecules are arranged on a conductive surface, and the STM tip is used to probe local electronic properties with a weaker coupling due to a vacuum tip-sample gap. The advantage of STM over the other platform lies in its ability to provide high-resolution images and local electronic information. However, it is difficult to shift the molecular level in the STM setup by using an additional gate electrode. In contrast, the second approach provides more degrees of freedom in the electrode arrangement and device design. The direct molecule-electrode contact allows the influence of the junctions and surrounding environment to be observed. However, one of the issues is the linkage stability between the molecules and the electrodes. Many techniques have been proposed to create a stable molecular junction, such as break junctions, crossed-wire junctions, and solid-state methods. In general, the first two techniques are not useful for practical device fabrication. Until recently, the process of electrode deposition on the molecules still caused electrical short circuits and damage to the molecules in solid-state methods. Wang *et al.*[21] suggested a novel route, by using graphene to form reliable electronic junctions with very high fabrication yield, good operational durability, and thermal stability regardless of molecular sizes and terminal functional groups. Unlike metal evaporation methods, a molecular contact with graphene does not suffer from these problems. The graphene contact, due to its excellent electronic properties, mechanical strength and chemical stability, outperforms molecular junctions with conductive polymers, such as PEDOT:PSS (Poly(3,4-ethylenedioxythiophene) poly(styrenesulfonate)) .[21] As such, many studies reported

potential applications for graphene electrodes in memory devices,[66] field-effect transistors,[67] light-emitting diodes,[68] and solar cells.[69]

Graphene is a single layer of graphitic carbon with a two-dimensional honeycomb lattice.[70] Figure 7 shows the atomic arrangement. Many studies have described the very interesting characteristics of graphene, such as its unique band structure,[71] remarkable carrier mobility and conductivity,[72] two-dimensional structure, as well as its optical,[73] thermal,[74] and mechanical[75] properties, summarized in Table 1. Recently, instead of mechanical exfoliation,[76] many approaches have been developed the manufacture of large-area graphene sheets, including thermal graphitization on silicon carbide,[77] chemical vapor deposition on metal substrates,[78] and growth from metal-carbon melts.[79] Compared with other carbon allotropes, such as carbon nanotubes and fullerenes, the two-dimensional structure of graphene simplifies the fabrication process to form a desired arrangement through standard semiconductor lithography. As such, many potential applications of graphene have already been reported, including high-frequency transistors, photon and chemical sensors, and transparent electrodes.[80-82]

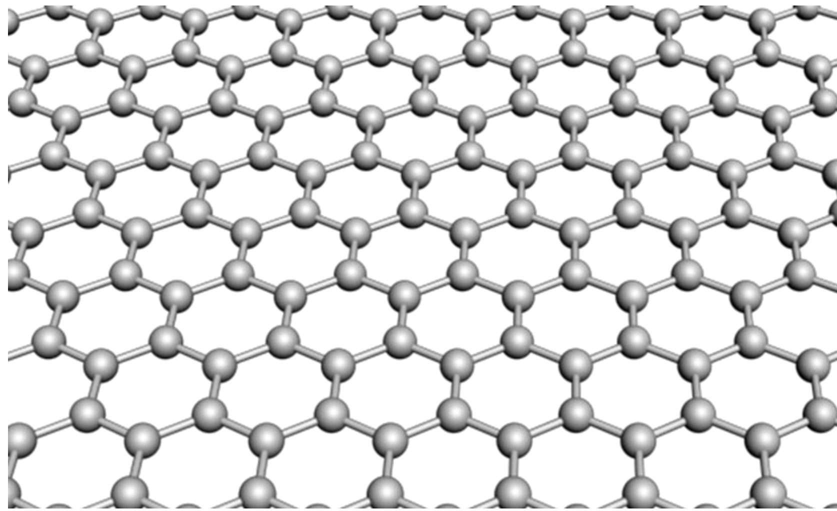

Figure 7. Atomic arrangement of graphene.

Table 1. Physical properties of graphene.

Physical properties	Values
Bond length[83]	1.42 Å
Optical absorption[73]	2.3 %
Thickness[83]	3.4 Å
Electrical resistivity[72]	10^{-6} Ω·cm
Carrier mobility[72]	Up to 200,000 $cm^2 V^{-1} s^{-1}$
Thermal conductance[74]	~ 25 $MW m^{-2}K^{-1}$
Mechanical strength[75]	130 GPa

The graphene band structure can be solved by tight binding approximation considering only the nearest-neighbor.[84] The linear energy dispersion close to Fermi level can be expressed as:

$$E(k) = \pm \hbar v_F |k|,$$

where $\hbar$ is the reduced Planck constant, v_F is the Fermi velocity, and k is the wave vector measured from the K or K' point in the reciprocal lattice space of graphene. The Fermi level is located exactly at the dispersion intersection in undoped graphene, where the electrical resistivity is a finite maximum due to its intrinsic minimum carrier density.[70] Figure 8a shows the relationship between the resistivity and the electron or hole densities introduced by a gate electrode in a graphene field effect transistor. A typical graphene transistor is shown in Figure 8b. When a positive bias relative to the graphene is applied on the gate, additional electrons will be injected into graphene framework, which therefore decreases the resistivity. A similar situation can also be observed along the negative side of the gate bias, but holes will be added. Based on Drude's model, the conductivity (σ), which is the inverse of the resistivity, can be expressed as:

$$\sigma = ne\mu,$$

where n is the charge carrier density, e is the elementary charge, and μ is the carrier mobility. Additional charge carrier density can be injected by applying a gate bias (V_G):

$$n = \frac{cV_G}{e},$$

where c is the specific capacitance of the dielectric layer. Therefore the carrier mobility can be obtained from the measurement of the relationship between the resistivity and the gate bias applied.

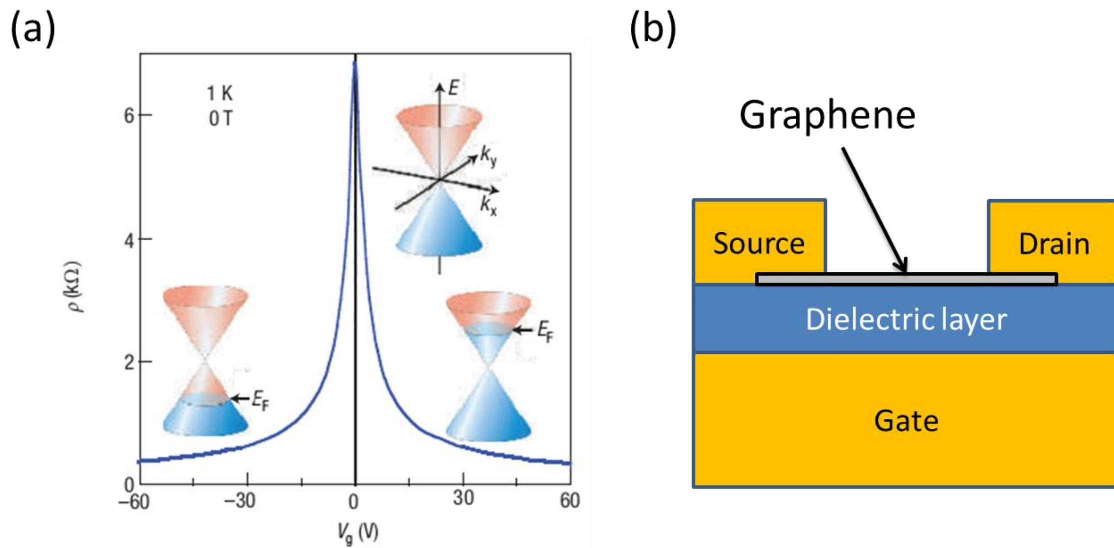

Figure 8. Graphene transistor: (a) resistivity altered by gate bias and (b) typical structure of a graphene transistor. Reprinted from ref. [70] with permission of Copyright (2007) from Nature Publishing Group.

The charge transport properties of graphene are mainly governed by the available carrier density and scattering mean free time, which may be modified by its surrounding situation. Other than the electric field effect, absorbates or the chemical environment may shift the graphene band structure but still maintain its linear dispersion.[85,86] Chemical doping can even be spatially controlled to create a desired potential surface, such as p-n junction, by adjusting the dopant distribution.[87] In addition, the energy band and dispersion may be further altered due to the breaking of the lattice symmetry.[88-90] Moreover, carrier mobility of graphene was found to be closely related to supporting materials.[91,92] Charged impurities at the graphene interface may increase the chance of carrier scattering, and thus decrease carrier mobility. As such, the choice of chemically

inert substrates or even the prevention of contact is a straight-forward way to increase the mobility. For example, the peak mobility for suspending graphene can reach over 200,000 cm^2/Vs,[91] and graphene on hexagonal boron nitride may also exhibit mobility up to 60,000 cm^2/Vs.[92] Fully understanding the role of neighboring components guides the design of molecular devices towards a direction of creating better and more useful functions, instead of limiting or impacting on their performance.

1.5 AFM nanolithography

Since the transport behavior of molecular system is largely determined by the surrounding material distribution, it is critical to pattern each component in a molecular device for the control and study of its properties. Nanolithography based on AFM has proven to be a useful method to guide molecular assembly with a resolution down to a few nanometers,[93] and is especially suitable for a laboratory scale. In general, the method uses a very sharp tip, with a radius of curvature of about 10 nanometers, to locally alter a region on a sample surface such that the chemical composition, surface morphology, or oxidation states are distinguishable from the rest of the sample surface. Due to the patterning mechanism, avoiding the usage of e-beam and polymer resist protect molecular structures from radiation damage[94] and polymer contamination.[83,85] There are several AFM nanolithography variations that can be distinguished based on their mechanisms, including dip-pen, nanoshaving, nanografting, electrochemical, and thermal nanolithography.[95-100] Figure 9 shows examples of some of these mechanisms, specifically: in dip-pen nanolithography, chemical compounds diffuse through a

meniscus at a tip-sample junction onto the sample surface in a controllable manner;[101] in nanoshaving and nanografting, chemical species at the tip-sample junction may be removed or replaced by the force exerted from the tip, respectively.[100] In addition, with external guidance, the kinetics of molecular assembly was observed to be accelerated and the surface defects and disorders were reduced.[102] In electrochemical nanolithography, redox reactions of chemical species within the meniscus at the tip-sample junction can be induced by an electrical bias externally applied between the tip and the sample. The patterning rate, determined by the modification kinetics, can be further boosted by up to 7 orders of magnitude by parallel writing techniques using two-dimensional tip arrays, as described by Salaita and Huo *et al.*[103] These mask-less creations of arbitrary patterns in ambient conditions make the technique an outstanding nanofabrication tool for day to day laboratory testing.

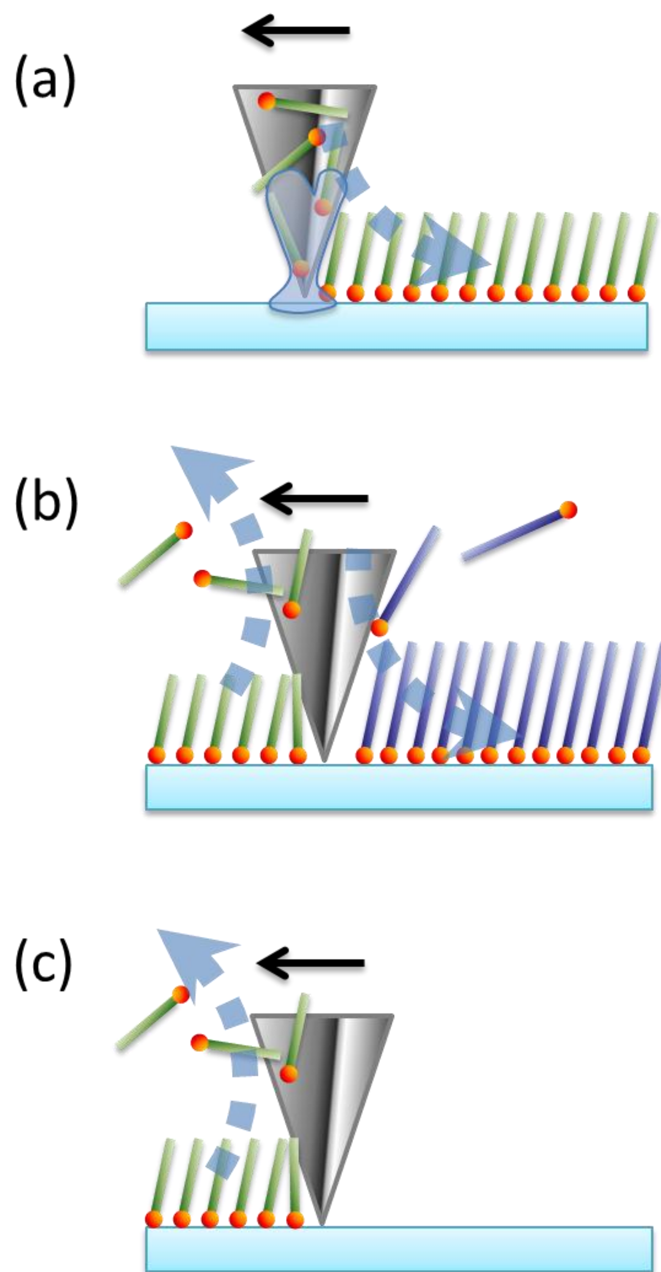

Figure 9. AFM-based nanolithography: (a) dip-pen (b) nanografting, and (c) nanoshaving. Black solid and blue dash arrows indicate tip moving and molecule packing/removing directions, respectively.

There are several other methods that can also achieve patterning molecular assembly, like photolithography,[104,105] electron-beam lithography,[106] and ion beam lithography,[107] where the molecules or polymers are exposed under irradiation, inducing chemical changes, such as protonation, oxidation, or degradation. However, the cost of the equipment and system maintenance can make these techniques less accessible for simple day to day laboratory testing. Two other means are micro-contact printing[108,109] and nanoimprint lithography,[110] where masters or masks are required, working by defining two regions: one blocking and the other permitting molecular assembly. However there are the disadvantages in the lack of patterning versatility and the difficulty of alignment between patterns.

1.6 Summary

The work in this dissertation has focused on addressing integrating patterning tools, characterization of molecular assembly at nanoscale during charge transport, and an electronic testing platform to obtain greater insight into molecule-based devices. A series of nanolithography approaches were demonstrated for the fabrication of simple graphene-based electronics, patterning both the desired graphene structure as well as the appropriate metal contacts. Using this approach, a transistor-like architecture was created and provides a versatile tool for the patterning of simple test structures without polymer resist contamination and radiation damage. The chemical changes induced by the charge transport were monitored by the TERS microscope on a series of molecular adsorbates on conductive substrates, such as rhodamine 6G on silver films,

mercaptobenzoic acid SAMs on gold films, and multilayer graphene on silicon. The new TERS system was proposed to overcome various long-existing issues in terms of sample limitations, complicated instrumental design, and difficulties in tip preparation. A micro-sized mirror was introduced under an optical microscope to reflect the laser onto the side of the tip, and chemically synthesized silver nanowires were used to prepare TERS-active tips.

In Chapter II, important experimental procedures regarding microscopy and nanolithography will be summarized. In Chapter III, the patterning technique and its relative lithographic processes will be discussed. The patterning method developed not only offers a simple, flexible, and low-cost method to create complex patterns for graphene FETs in a laboratory scale without using expansive e-beam or photolithographic equipment, but more importantly they provide a platform for the systematic study of molecular assemblies built upon the FETs. The electrical properties of the single-layer graphene FET and porphyrin-graphene composite FET made by this approach were studied. As such, the technique may provide a versatile platform for the further investigation of devices with graphene-molecular contacts and for constructing higher order structures.

In Chapter IV, the development of the chemical sensing platform enabling chemical changes to be monitored will be focused on. The combined platform of a side-illumination TERS and conductive-probe AFM was built to observe modification induced from AFM-based nanolithography. The local decomposition was observed

under harsh conditions. The silver-coated tip can enhance Raman signals in the range of 10^3 to 10^5, which provides reasonable sensitivity and spatial resolution.

Chapter V focues on a newly proposed TERS setup. Compared with other TERS geometries, the new optical design not only allows the analysis of large or opaque samples, but also simplifies the design of the optical components and the alignment processes of the setup. The use of a nanowire as an enhanced probe provides various advantages over the typical metal evaporation methods for TERS tip preparation. The surface plasmon polaritons of these crystalline nanowires have a consistent resonance wavelength, which is important for matching the excitation wavelength to improve the Raman enhancement.

Finally, Chapter VI provides a summary and future direction. Overall, the development in the fabrication and the chemical sensing of molecular devices has provided us with a useful system to investigate the role of each element. The knowledge gained here may lead towards the creation of better and more beneficial functions in future molecular devices. This report represents an analytical chemistry tool and a patterning approach for graphene-based devices.

CHAPTER II

EXPERIMENTAL METHODS

The primary techniques used in this dissertation include AFM, confocal microscopy, nanoshaving lithography, and electrical measurement. AFM was mainly used for high-resolution image scanning and maintaining an AFM tip in contact with the surface of the sample of interest. Confocal microscopy was for optical imaging and collection of Raman scattering and fluorescence. Controlled molecular assemblies and electrode arrangement were made by nanoshaving lithography. The electronic properties of a device made by the lithography can be obtained by electrical measurements. Each method will be described in detail in the following sections.

2.1 AFM

Since its invention in 1986 by Binning, Quate, and Gerber,[111] AFM has quickly developed into one of the most powerful techniques for high-resolution surface imaging and analysis. The ingenious setup has a sharp tip mounted on a cantilever that is brought into contact, or near contact, with a sample surface, where it performs a raster over a region of interest. As depicted in Figure 10, the operating principle relies on force sensing from the cantilever to trace the contact position and to map the topographic image over the scanned area. According to Hooke's law, the force is typically measured by a quadrant photodetector from a deflection in the laser reflection due to the bending of the cantilever. A piezoelectric actuator controlled by a feedback loop is used to

maintain a suitable relative position between the tip and the sample. Various tip-sample interactions can be used as feedback mechanisms, such as van der Waals forces, magnetic forces, and electrostatic forces, making it is possible to image additional surface properties like friction, adhesion, elastic properties, magnetic properties, and sample conductivity.

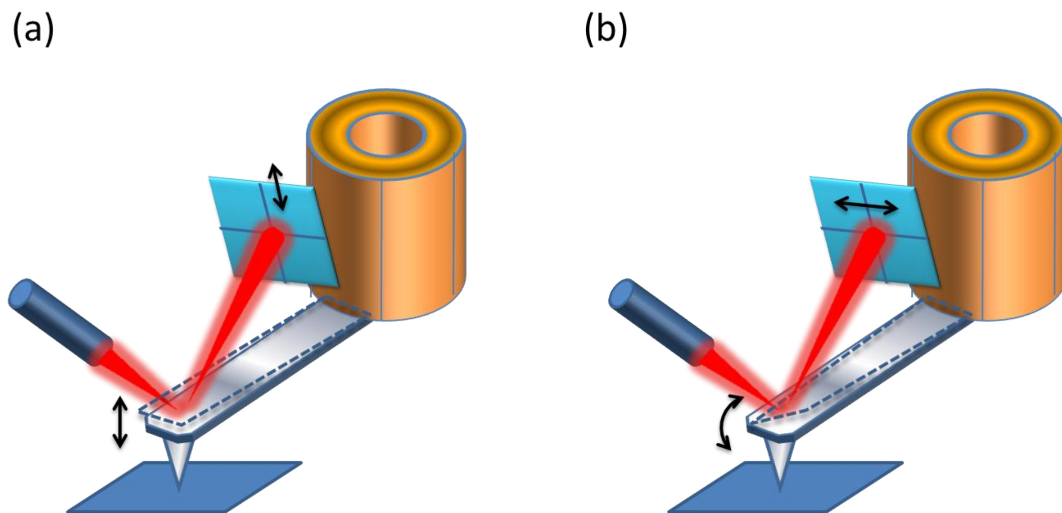

Figure 10. Principle of AFM operation: (a) normal force deflection, and (b) lateral force deflection.

This work used a WITec AFM alpha 300 and an Agilent 5500 AFM with contact and tapping modes as the major operating methods. Under contact mode, a constant repulsive force applied vertically to the samples was maintained by adjusting the relative

positions of the tip and the samples during scanning. The adjustment motion was recorded as sample surface topography. Friction images may be obtained simultaneously by detecting lateral forces. The contrast in friction can be used to evaluate mechanical and surface properties preliminarily. The basic operating parameters of the AFM may need to be modified to fit the environments of the different experiments. To prevent lateral forces from changing surface topography, cantilevers with spring constants below 1 N/m were chosen. When performing in liquid, a liquid cell was refilled with the desired solution until a liquid immersion objective or a nose cone was immersed, in order to provide a feedback laser path free from the influence of the liquid-air interface. Under tapping mode, a cantilever was driven to vibrate at its resonant frequency by a piezoelectric element. A constant damping in the oscillation amplitude due to tip-sample interaction was maintained by the feedback loop control system. The lateral forces were reduced to a negligible level, and thus, this mode minimized sample damage. Images based on phase shifts between the free oscillations and the damped oscillations were collected at the same time. The phase contrast can be used to distinguish local viscoelastic and adhesive properties of samples

2.2 Confocal microscopy

Confocal microscopy is an optical technique that achieves higher spatial resolution than conventional microscopy by using point illumination and a spatial pinhole to block out-of-focus light from the samples. Two or three-dimensional structures of a sample can be reconstructed from confocal scanning over the entire

sample volume. For the setup in the lab, as shown in Figure 11, an Ar ion laser at 488 nm was used as a point light source and introduced to the main optical axis in the microscope by an optical fiber coupler. The coupler contained a pinhole, a collimation lens, and a beam splitter. The pinhole confined the width of the excitation point. The beam splitter reflected only the light with a wavelength close to the laser wavelength. The collimated laser beam was focused onto a sample by an infinitely corrected objective lens. Because only one point in the sample is illuminated at a time, confocal microscopy provides several advantages including: reducing the depth of field, eliminating image degradation by blocking out-of-focus regions, and allowing the collection of serial optical sections from thick samples. The light produced from the focused volume, including reflection, fluorescence, and Raman scattering, was collected with the same objective and focused by a tube lens onto another pinhole. The second pinhole greatly increased the intensity contrast between the focal volume and the region out of focus. Depending upon experimental needs, a long-wavelength-pass filter or a notch filter can be inserted between the tube lens and beam splitter to remove the excitation laser. The collected signals penetrating the second pinhole were sent through fiber optics to a spectrometer, equipped with a thermoelectrically cooled CCD (Andor DV401-BV).

The images and three-dimensional structures can be reconstructed from the raster scanning. The scanning was achieved by moving samples on a 3-axis piezoelectric scanning stage, while the rest of the microscope was kept still. The detected intensity or spectral response represented pixel brightness, and the complete image or structure was

obtained pixel-by-pixel. Slower scanning may produce a better signal-to-noise ratio and thus better imaging quality. Typical scanning rates varied from 40 ms/pixel to a few sec/pixel. The maximum scanning range was 100 × 100 × 20 μm. In addition, a sliding prism can also be inserted between the tube lens and the pinhole to direct the light to a color video camera. In this situation, another lamp producing a white light was usually used to illuminate the whole imaging field of the samples and to form a conventional microscopic image.

2.3 Nanoshaving lithography

Nanoshaving lithography is a straightforward patterning technique utilizing the AFM. In this process, materials from a sample are displaced by an AFM tip, which creates pits or trenches along the path that the tip traverses. In the case of alkanethiol SAMs on gold, the bonds between sulfur and gold, with a bond strength of 184 kJ/mol[112], are significantly weaker than the C−C bonds, which have a bond energy of 618 kJ/mol. Under a load higher than the threshold of 0.4 GPa,[113] the alkanethiol linkage is susceptible to cleavage. Solvents such as ethanol are frequently used to carry displaced molecules away. The instrumental setup is shown in Figure 12, with the WITec AFM alpha 300 and liquid cell. The liquid cell was filled with ethanol until a liquid immersion objective was immersed, which allowed a feedback laser path free from the influence of the liquid-air interface. Tips purchased from Mikromesh(CSC37-AlBS) with a spring constant of 0.65 N/m were used to provide sufficiently high load for nanoshaving

nanolithography on the SAMs without any tip pretreatment.1-Octadecanethiol (ODT) SAMs were then patterned in pure ethanol by the tips based on the patterning design.

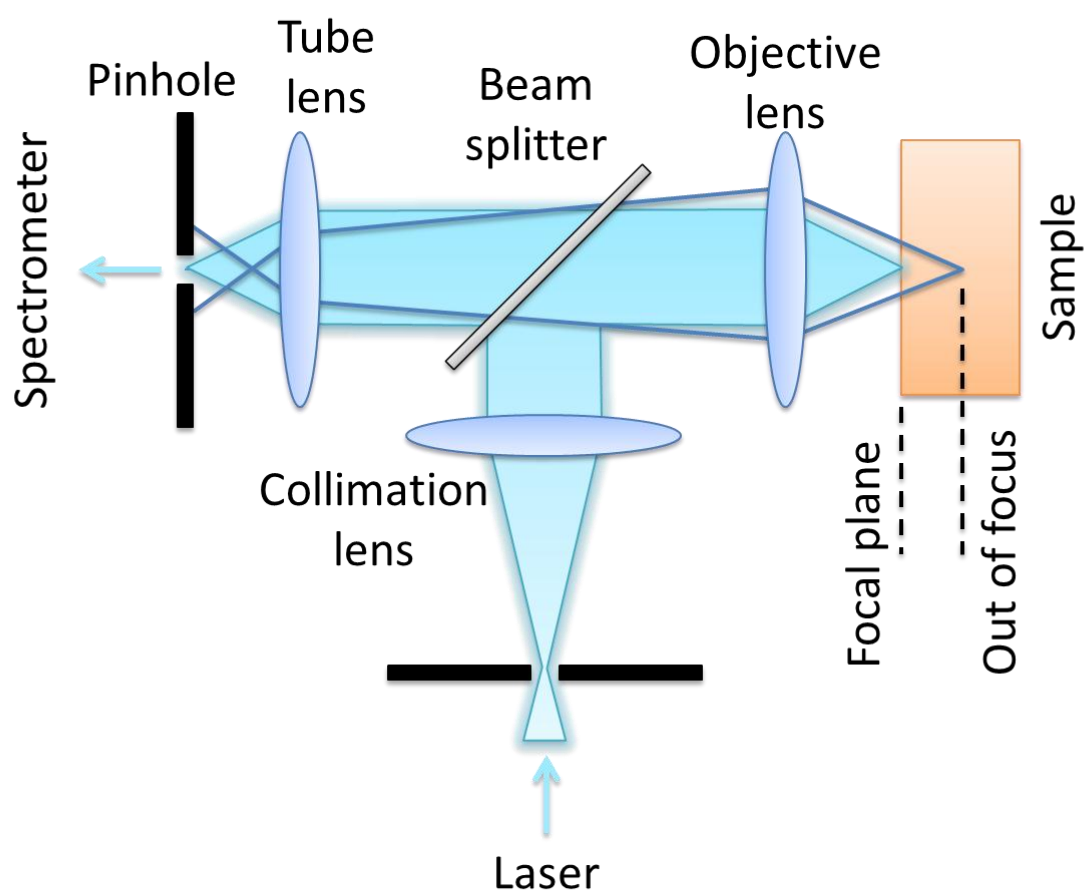

Figure 11. Schematic illustration of a confocal microscopy set up.

Alkanethiol SAMs on gold were prepared prior to the nanoshaving steps. Sample substrates (glass or silicon wafer) were first cleaned by sonication in isopropanol, then acidic piranha cleaning, and finally by an alkaline piranha cleaning. Cr and Au films were deposited on the substrates through vacuum thermal evaporation (BOC Edwards Auto 306) at the rates of ca0.01 nm/s and 0.03 nm/s, respectively. The thickness of the Cr and Au layers, monitored by a quartz crystal microbalance, were maintained at a nominal 5 nm, and 20 nm, respectively. ODT SAMs on Au were prepared immediately after the thermal evaporation by immersing the coated samples in 1 mM ODT ethanol solution for at least 12 hr. After the ODT monolayer was patterned, the same patterns can be transferred to the metallic layers by selective etching. The patterned sample was immersed in the Au etchant containing 20 mM $Fe(NO_3)_3 \cdot 9H_2O$ and 30 mM thiourea in aqueous solution for 2 ~ 10 min. Due to the blockage of the alkane chain, Au atoms linked with ODT react with the etchant very slowly. Thus, the exposed region can be dissolved before the protected region is damaged. Then the Cr layer under the now removed Au film was further etched by the Cr etchant consisting of 3.8 % ceric ammonium nitrate and 3.5 % acetic acid in aqueous solution for 20 ~ 120 sec. After etching, the samples were rinsed with plenty of water to remove any residue, and stored in vacuum.

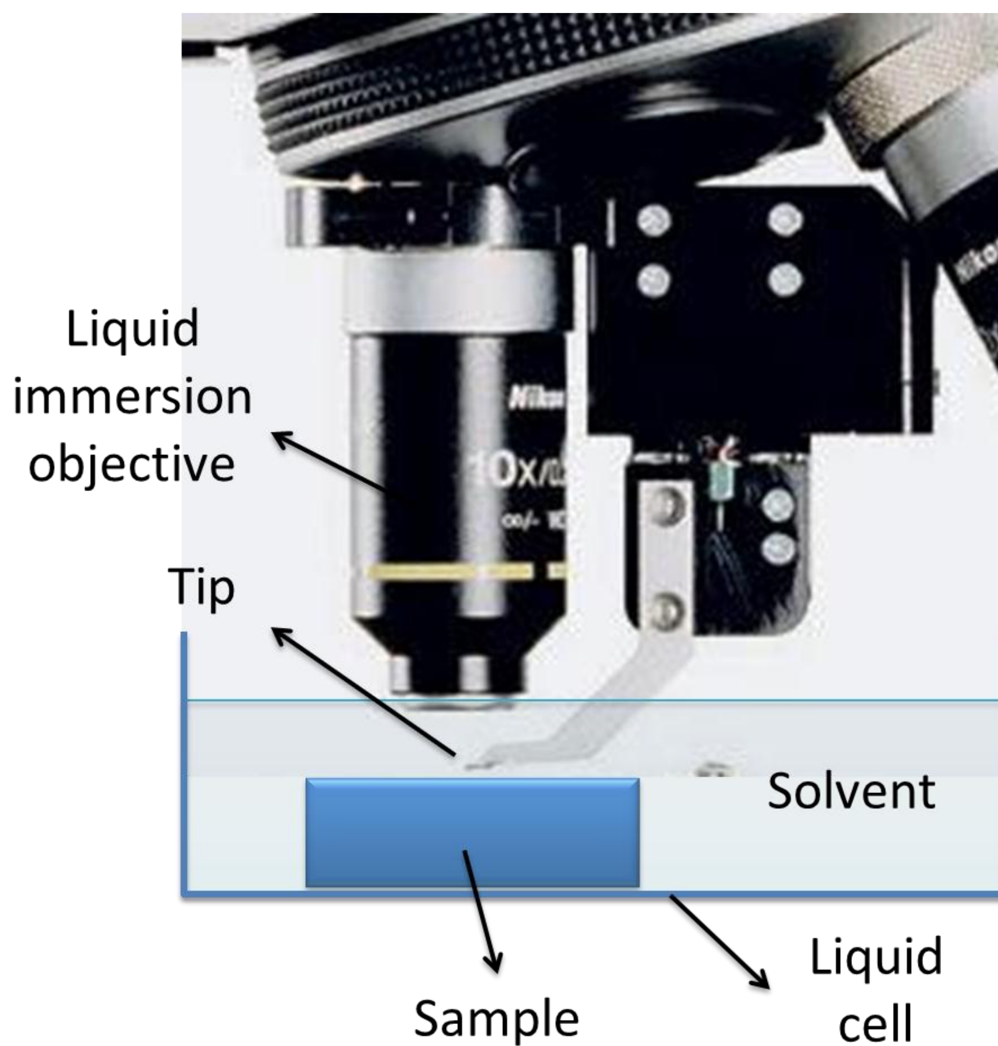

Figure 12. Instrumental setup for nanoshaving nanolithography.

2.4 Electrical measurement

The electrical measurement was collected by a lock-in amplifier (Stanford Research Systems SR830), a custom-built probe station, and a computer. A sample containing the source, a drain, and gate electrodes was connected to the lock-in amplifier

through the wires in the probe station, as shown in Figure 13a. The equivalent electric circuit is depicted in Figure 13b, where the sample was connected in series to a small resistor with a known resistance, *r*. Based on the lock-in amplifier, both the in-phase and out-of-phase signals can be obtained. The measured voltage $\vec{V}_r$, and the current $\vec{I}_r$, across the small resistor can be expressed as:

$$\vec{V}_r = \left|\vec{V}_r\right| \cdot e^{i(\omega t+\theta_r)},$$

$$\vec{I}_r = \frac{\left|\vec{V}_r\right|}{r} \cdot e^{i(\omega t+\theta_r)},$$

where ω is the reference frequency, *t* is the time, θ_r is the phase difference related to the reference generated in the lock-in amplifier. The sample resistance $\vec{Z}_R$, can be assumed:

$$\vec{Z}_R = \left|\vec{Z}_R\right| \cdot e^{i(\theta_R)} = R + iX,$$

where θ_R is the phase difference related to the reference, *R* is the real part of the resistance, and *X* is the imaginary part of the resistance. The current $\vec{I}_r$, across the sample and the small resistor can also be expressed as:

$$\vec{I}_r = \frac{\left|\vec{V}_{Ref}\right| \cdot e^{i(\omega t)}}{(R+r)+iX},$$

where $\vec{V}_{Ref}$ is the voltage output of the reference. By comparing the equations above, the following expressions can be obtained:

$$R = \frac{\left|\vec{V}_{Ref}\right| \cdot r}{\left|\vec{V}_r\right|} cos\theta_r - r\ ,$$

$$X = \frac{-\left|\vec{V}_{Ref}\right| \cdot r}{\left|\vec{V}_r\right|} sin\theta_r\ ,$$

$$\left|\vec{V}_R\right| = \frac{\left|\vec{V}_r\right| \cdot r}{r} \left|\vec{Z}_R\right| ,$$

where $\left|\vec{V}_R\right|$ is the absolute value of the voltage across the sample.

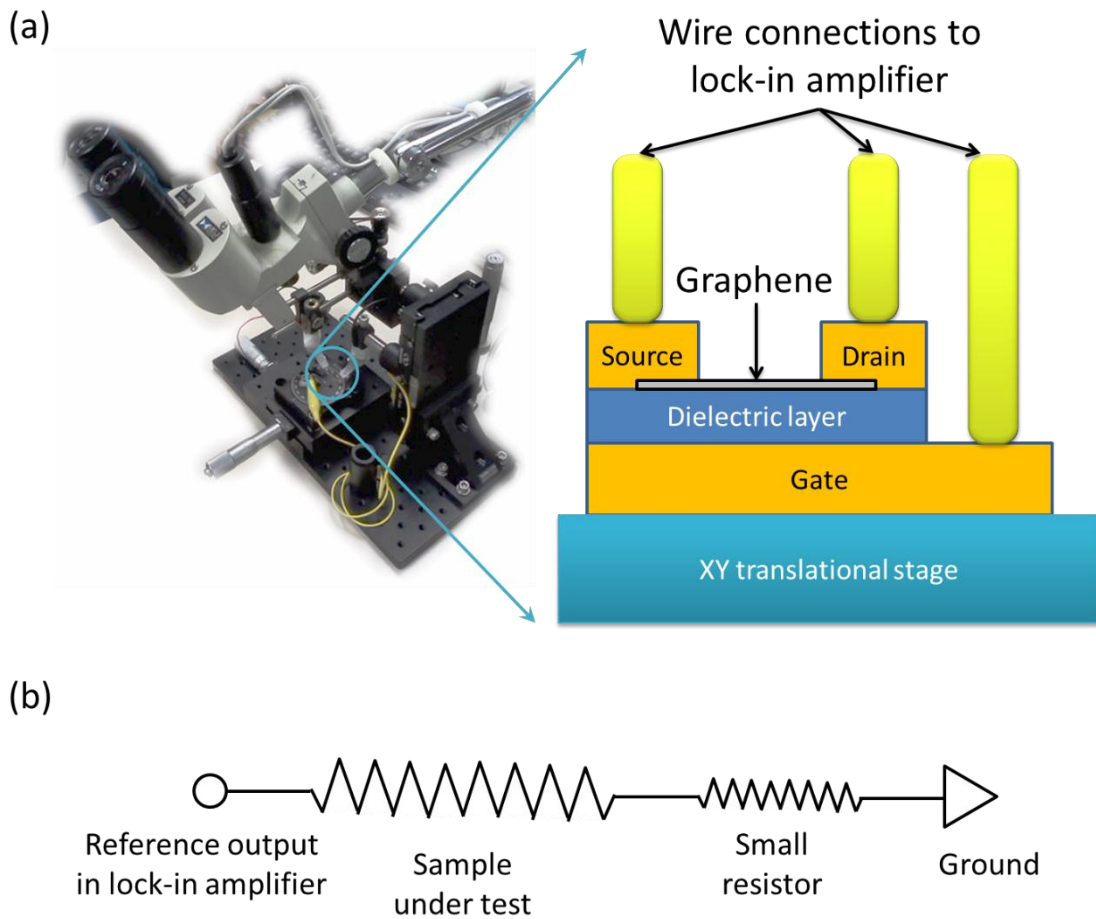

Figure 13 Wire connection of electrical measurement: (a) on a probe station and (b) of equivalent electric circuit.

It should be noted that the real part of the sample resistance, R, does not equal the resistance of a conductive channel in the sample, for example, the graphene channel. Based on Drude's model, the real part of the sample resistance, R, can be expressed as:

$$R = R_c + \frac{L/W}{n_c e \mu_{e,h}},$$

where R_c is the contact resistance, L and W are the length and width of the graphene stripe, μ_e and μ_h are the electron and hole mobility, respectively, e is elementary charge, and n_c is the charge carrier concentration (electrons or holes) in the graphene stripe. The n_c can be calculated approximately as:[114]

$$n_c = \sqrt{n_0^2 + \left(\frac{c'|V_g - V_D|}{e}\right)^2},$$

where n_0 is the charge carrier concentration at the Dirac point, c' is the specific capacitance of the silicon dioxide layer, V_g is the gate voltage, and V_D is the Dirac voltage. As such, further electronic properties can be obtained by varying the gate voltages.

CHAPTER III

PATTERNING OF GRAPHENE FIELD EFFECT TRANSISTORS BY SCANNING PROBE LITHOGRAPHY

3.1 Introduction

Graphene has drawn significant attention since the "scotch tape method" was revealed by Geim *et al.* in 2004,[76] enabling a facile route to laboratory scale fabrication and testing of graphene structures. Since then, many studies have described the very interesting properties of graphene, such as its unique band structure,[71] remarkable carrier mobility and conductivity,[72] as well as its thermal[74] and mechanical properties.[75] Recently, many approaches have been developed for large-area fabrication of graphene sheets, including thermal graphitization on silicon carbide,[77] chemical vapor deposition on metal substrates,[78] and growth from metal-carbon melts.[115] Compared with other carbon allotropes, such as carbon nanotubes and fullerenes, the two dimensional structure of graphene simplifies the lithographic processes needed to form a complex electronic arrangement through CMOS-compatible fabrication techniques. As such, many attractive applications of graphene have already been reported, including high-frequency transistors, optical and chemical sensors, and transparent electrodes.[80-82] Photolithography and electron beam (e-beam) lithography are often used to precisely create nanoscale structures for these applications. However, the cost of the equipment and the system maintenance can make these techniques less accessible for simple day to day laboratory test structures. Moreover, contamination from the corresponding resist

materials used in such techniques[85] and the damage from electron radiation can limit these lithographic methods as they impact the electronic properties of the fabricated structures.[94]

Recently, several methods have been proposed for the pattering of graphene to achieve either selective etching or electrode contact fabrication. Masubuchi *et al.* demonstrated the use of local anodic oxidation lithography to selectively remove carbon atoms near the apex of a metallic atomic force microscope (AFM) tip under a DC bias.[116] Wang *et al.* also showed out that graphene patterns could be etched by masks fabricated via dip-pen nanolithography.[117] However, these two strategies still employed e-beam lithography or photolithography to make electrodes linked to graphene layers before or after graphene patterning. As such, the polymeric resists needed to be used were found to contaminate the graphene structures.[83] Approaches for making direct metallic contacts have been realized by stencil lithography[118] and nano-soldering.[119] The former utilizes a silicon shadow mask during metal evaporation to direct the deposition of electrodes onto a graphene flake, while the later forms a metallic contact when a thin wire of an indium-tin alloy melts on graphene layers on a heated stage. Both of these approaches need additional lithographic methods to pattern graphene.

Alternative patterning approaches such as nanolithography based on AFM has been developed to make fine structures with feature sizes down to < 10 nanometers.[100] The main patterning mechanism relies on using a sharp AFM tip with a radius of curvature of < 10 nm to locally manipulate materials near the tip-sample junction. For example, in dip-pen nanolithography, an “ink” is transferred from the AFM tip apex onto

a sample surface in a controllable manner,[101] through techniques such as nanoshaving and nanografting, while chemical species on a sample surface may be removed or replaced, respectively under the tip apex.[100] The patterning rate, determined by the tip speed, can be further boosted up to 7 orders of magnitude by parallel writing techniques using two dimensional tip arrays, as described by Huo *et al.*[103]

In order to facilitate measurement and testing of nanoscale graphene based electronic devices in the laboratory without the need for e-beam, here we demonstrate the fabrication of nanoscale graphene field effect transistors using a combination of scanning probe lithography and simple oxygen plasma etching to afford patterning of both the desired of graphene structure as well as the appropriate metal contacts. This approach in essence allows anyone with an AFM and an optical microscope to fabricate simple test structures, such as field effect transistor (FET) architectures, without polymer resist contamination.

3.2 Methods

All graphene flakes were mechanically exfoliated and deposited on an oxidized silicon wafer with nominal 90 nm silicon dioxide formed by dry thermal oxidation. The number of layers for each flake was confirmed by its optical contrast and Raman scattering. Cr and Au films were further coated on graphene samples through vacuum thermal evaporation at the rates of ca 0.01 nm/s and 0.03 nm/s, respectively. ODT SAMs on Au were prepared immediately after the thermal evaporation by immersing Au-coated graphene sample in 1 mM ODT ethanol solution for at least 12 hr. ODT monolayer was

patterned in pure ethanol by tips based on patterning design. All tips were purchased from Mikromesh (CSC37-AlBS, spring constant: 0.65 N/m) without any tip modification. After ODT monolayer was patterned, the sample was immersed the Au etchant containing 20 mM $Fe(NO_3)_3 \cdot 9H_2O$ and 30 mM thiourea in aqueous solution for 2 ~ 10 min. Cr layer under Au film was further etched by the Au etchant containing 3.8 % ceric ammonium nitrate and 3.5 % acetic acid in aqueous solution for 20 ~ 120 sec. After the metal mask was patterned, the exposed graphene regions would be removed in an oxygen plasma chamber for 10 min (Harrick 18W 0.1 torr). In the final step, the metal mask was reshaped to form electrodes linked the patterned graphene flakes by repeating the previous nanolithographic steps.

All the optical microscopic pictures, AFM images, and Raman spectra were recorded by a combine system of confocal Raman and atomic force microscope equipped with a thermo-electric cooled spectrometer (Andor DV401-BV). The Raman spectra were collected under a 488 nm Ar ion laser with a controlled power less than 1 mW for 10 sec. The thickness of a SiO_2 layer grown by thermal oxidization was measured by an auto-nulling spectroscopic imaging ellipsometer (Nanofilm EP3-SE). The electrical characterization was performed on a home-made probe station with a lock-in amplifier (Stanford Research SR830) through a standard lock-in technique.

3.3 Results and discussion

A flow chat of the patterning process is illustrated in Figure 14, with the details describe later in the text. Briefly, graphene flakes were mechanically exfoliated and

deposited on an oxidized silicon wafer, prepared with a nominal 90 nm thick SiO_2 gate oxide formed by dry thermal oxidation. The number of layers for each flake was confirmed by its optical contrast[120] and Raman scattering using Raman microspectroscopy.[121] A Cr adlayer (~ 5 nm) followed by an Au film (~ 20 nm) were deposited on the entire surface (including regions with graphene) through vacuum thermal evaporation. Octadecanethiol (ODT) SAMs on Au were formed by immersing the Au-coated sample in 1 mM ODT ethanol solution for at least 12 hr. Selecting a region over the desired graphene feature to be used for device fabrication, a portion of the ODT monolayer was removed by AFM nanoshaving in pure ethanol to create the basis for the desired electrode pattern. The uncovered Au regions were then etched away with an Au etchant of ferric nitrate and thiourea solution, which was used due to its less toxicity and higher selectivity as compared to cyanide-based etchants.[122] The remaining Cr adlayer under Au film was etched by a Cr etchant containing ceric ammonium nitrate and acetic acid. After the metal layers were patterned as a mask, the exposed graphene regions were then removed by oxygen plasma etching. To form electrodes linked only by the patterned graphene flakes, the remaining metal linkage between the electrodes was removed by repeating the previous nanoshoaving step. The final structure of the graphene FET consists of a thin graphene stripe, two metallic electrodes linked to the stripe, and a silicon back gate spaced by silicon dioxide. Here we now describe the entire process and the electrical characterization of the test structures in detail.

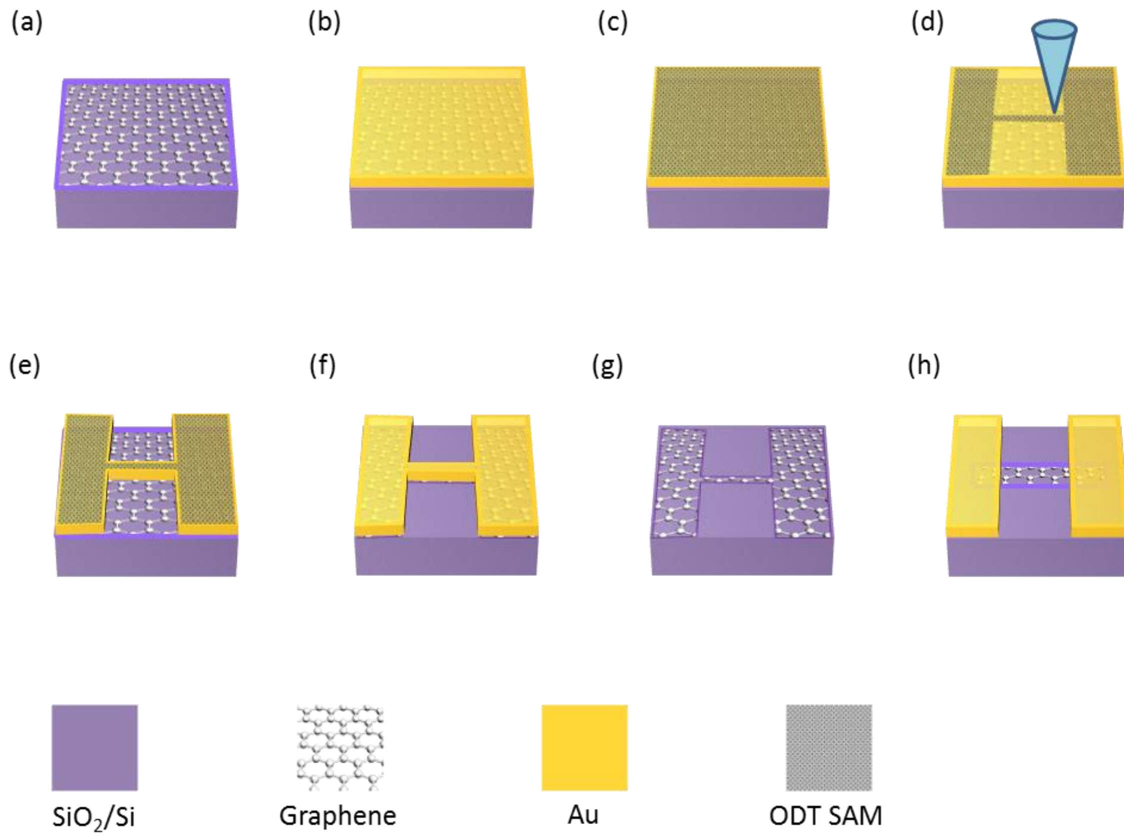

Figure 14. Schematic of the fabrication process for creating a graphene FET by AFM-based nanolithography: (a) deposition of graphene on an oxidized Si wafer, (b) deposition of Au on top of the graphene layer, (c) formation of an ODT SAM on the Au thin film, (d) patterning the ODT SAM by AFM nanoshaving, (e) transferring the ODT pattern onto the Au layer, (f) transferring the pattern further onto the graphene layer, (g) removal of the Au thin film, and (h) formation of electrode contacts by repeating the steps (b)~(g). The square patterns in the bottom represent the materials used in the flow chart.

Patterning graphene and metal electrode layers

A few steps need to be accomplished prior to the nanolithographic processes.

Figure 15a and 2b show an example of a single-layer graphene flake before and after

Au/Cr coating. Although the optical contrast was lower than that prior to metal deposition, the flake with thin Au/Cr coating was still able to be readily observed under an optical microscope (N 100 X, 0.9 NA objective). Interestingly, the thickness of the graphene flakes over the substrate with the metal coating was observed to be 3.5 nm (compared with 0.34 nm, the thickness of a single-layer graphene) in the AFM scanning image, as shown in Figure 15c. Similar increased thickness was also reported in literature.[76] We also observed that the intrinsic stress of the deposited metallic layers built up during thermal evaporation. Figure 15d shows an extreme example where the metallic layers exhibited some corrugated blisters under very large tensile stress. The metal films tended to peel off on top of larger graphene/graphite flakes, because larger stress was able to accumulate and to overcome the adhesion to the flakes. Such intrinsic stresses of metal thin films can arise from grain boundary restructuring due to a number of factors including environment, lattice expansion during growth, interface lattice mismatch, and surface stress due to the reduced coordination.[123] As shown in Figure 15c, the issue can be substantially mitigated by increasing the adhesion by the addition of an intermediate Cr layer, and by optimizing the parameters during thermal evaporation, such as suitable deposition rate and temperature. Similarly, Wang *et al.* reported that coating a thin layer of Au may also shift the position of graphene/graphite flakes and thus cause wrinkles and cracks, although they hypothesized that this phenomenon might be due to Au atoms impinging and intercalating into the flake.

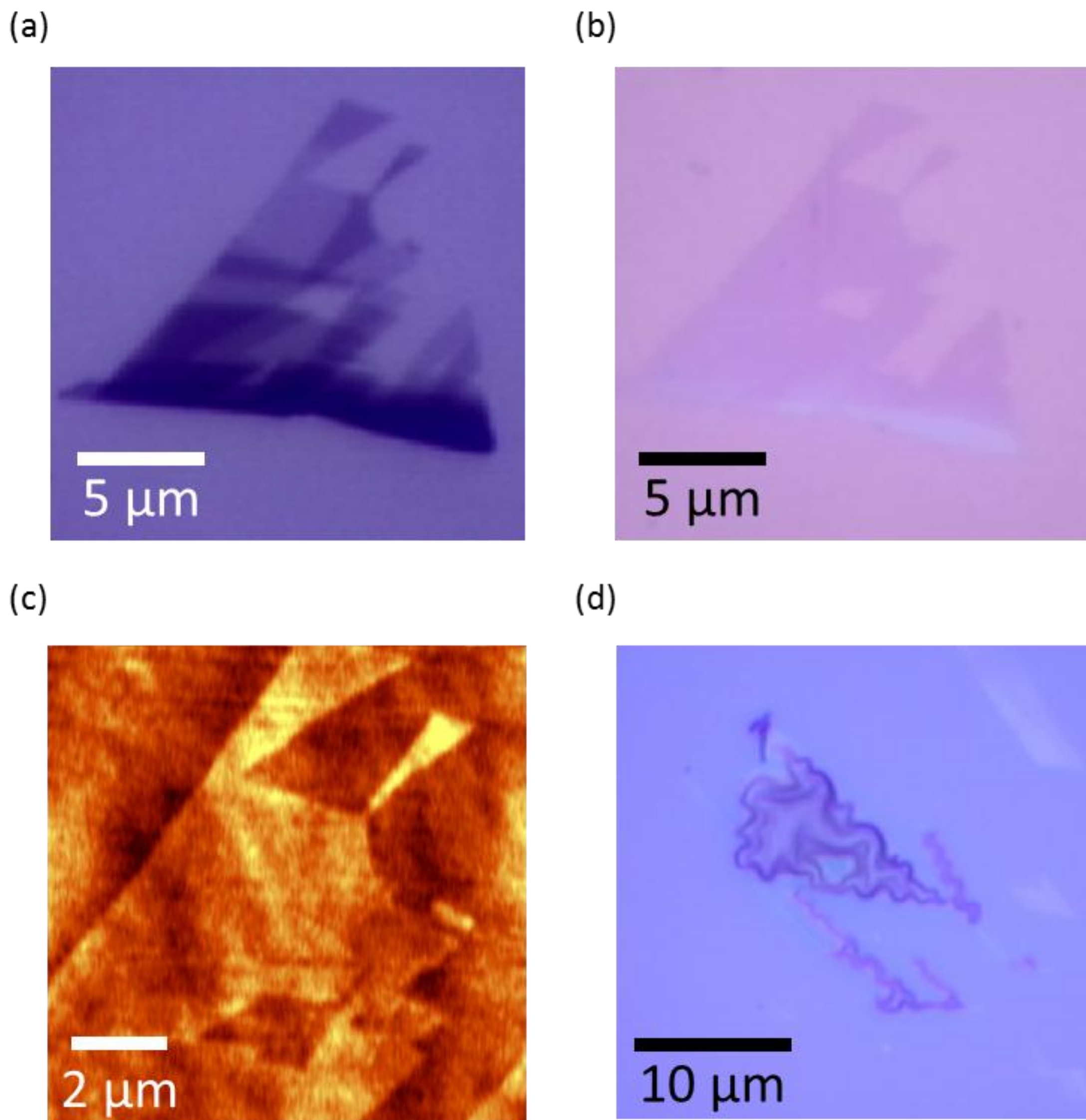

Figure 15. Optical and AFM images of graphene coated with Au/Cr layers: (a) optical microscope image of a graphene flake, (b) optical microscope image of the graphene flake coated with Au/Cr layers, (c) AFM topographic image of the graphene flake coated with Au/Cr layers and color scale, and (d) corrugated blisters in Au/Cr layers formed under very large tensile stress.

Using nanoshaving, any pattern can be produced at a moderate rate with minimal geometric limitations depending on the patterning capabilities of the AFM being used. A sharp AFM tip was used to apply sufficient force (> 10 nN) selectively breaking the bonding between ODT molecules and the Au layers. The solvent molecules, such as, ethanol, were responsible for carrying ODT molecules away from the binding sites. This process created a negative tune compared with nanoshaving paths. Without the protection of ODT molecules, the exposed metal layers may be removed after etching steps, and the patterns in graphene layers may also be developed after oxygen plasma treatment. It should be noted that the patterning rate in our processes, determined by tip moving speed, was in the range of 20 ~ 100 μm/sec, which is 2 ~ 3 orders of magnitude faster than other AFM-based nanolithography, such as dip-pen and local anodic oxidation nanolithography.[116,124] As such, even a complicated design can be finished within a reasonable time. Simple examples of graphene and Au patterns were demonstrated, including stripes and gaps, shown in the AFM topographic image (Figure 16a). The minimum feature size of was 130 nm in width. The metal layers were further removed on purpose to observe the underlying pattern of graphene stripes. The graphene stripe covered by the 130 nm Au mask had a thinner width of 100 nm, shown in the AFM lateral force image (Figure 16b) and its cross-sectional profile (Figure 16c). The width difference between the Au mask and the graphene stripe was attributed to the effects of undercutting during etching, and AFM tip broadening, in which the lateral feature is widened due to the tip-sample convolution.

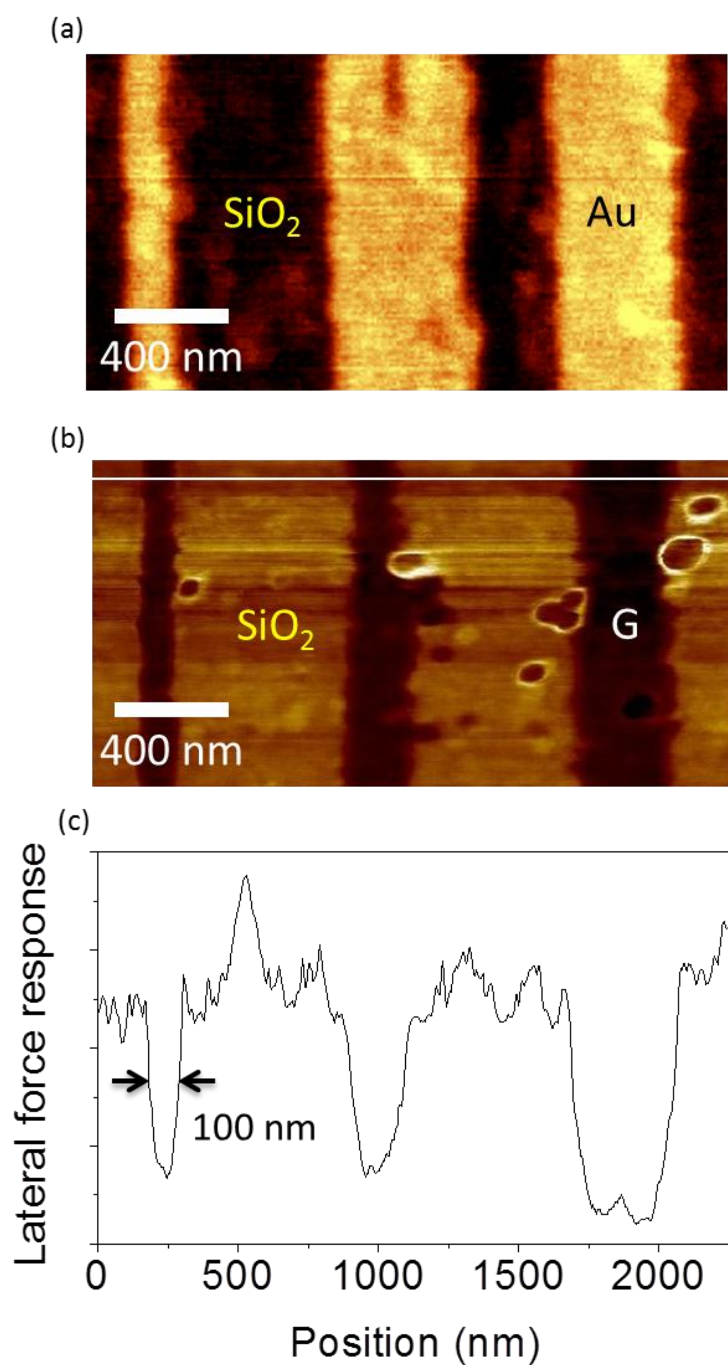

Figure 16. Examples of patterned Au masks and graphene: (a) AFM topographic image of Au stripes used as a mask for graphene etching, (b) AFM friction image of graphene stripe underneath the Au stripes, and (c) cross-sectional profile along the white solid line in (b)

Lithographic alignment and graphene integrity

To optimize feature placement, alignment between each patterning layer can be achieved by the triangulation through the use of markers. The target position of a graphene flake was determined by at least two makers inserted between an oxidized Si substrate and deposited metal layers, where the target coordinates were calculated from the angles to the target from the known markers and the known distance between the markers (Figure 17a). Once the position was obtained, all the coordinates of shaving paths were calculated relative to that point. Figure 17b shows some markers deposited on an oxidized Si wafer surface by epoxy dip-pen nanolithography. The marker size can be controlled in the range of a few micrometers in diameter by its transferring time. A few markers with different sizes after the deposition of metal layers are shown in Figure 17c, where the larger ones provided the quick guidance under a low-magnification optical microscope and the smaller ones increased the locating precision. We chose silver-filled epoxy (Epo-Tek H31) simply because of its suitable viscosity and adhesion as well as its obvious optical contrast on many sample substrates (*e.g.* Si wafers and glass slides). Interestingly, the diameter of an epoxy dot on an oxidized Si wafer surface tended to shrink after thermal curing and the deposition of metal layers probably due to its deformation and change in density. Typically, the smallest marker of *ca.* 400 nm in diameter was achieved consistently. This alignment method provides two major advantages: 1) quickly locating targets, and 2) avoiding unnecessary AFM scanning directly on the targets. AFM scanning slightly disturbs the integrity of the ODT SAMs, which weakens their protection against metal etchants. As such, some defects may form

along AFM scanning traces during etching steps. Figure 17d shows the defect formation in the scanning rectangular region, when the metal etching time was prolonged on purpose.

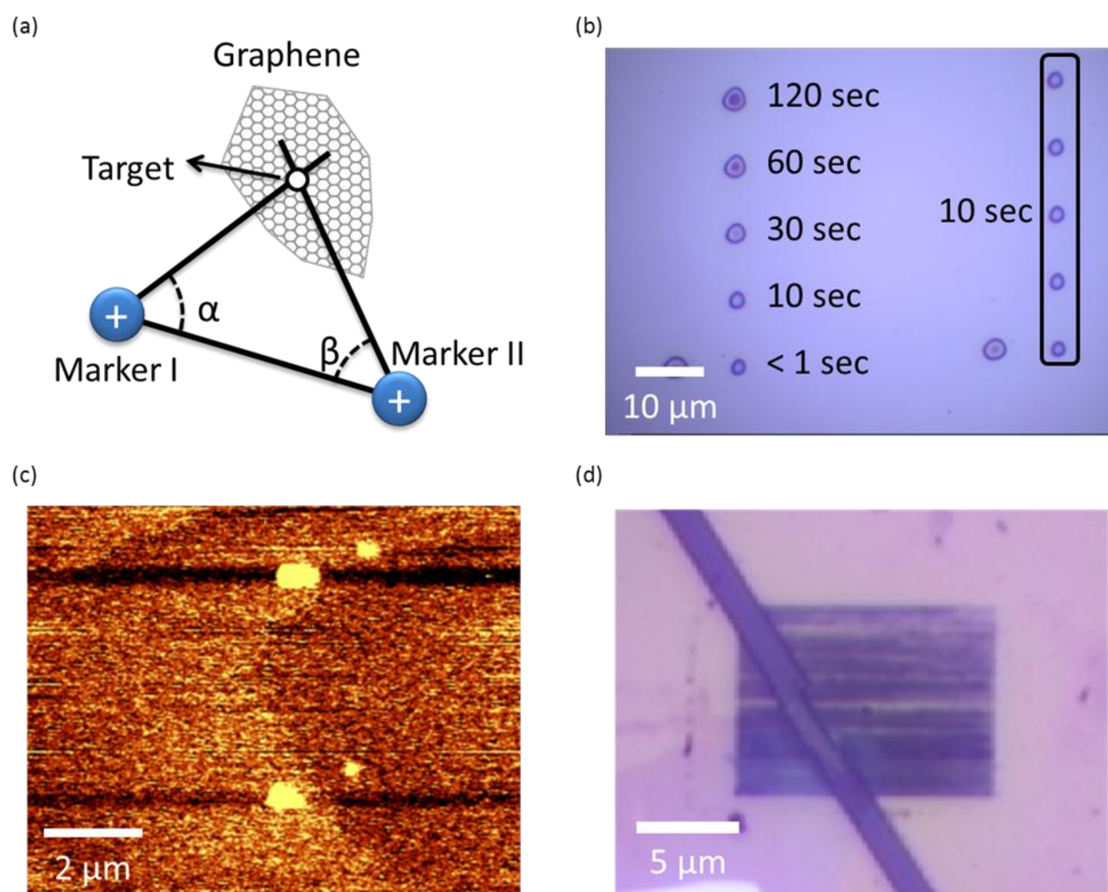

Figure 17. Images of markers and defects during etching: (a) scheme for triangulation locating method, (b) optical picture of markers with various sizes, (c) AFM topographic image of cured marker coated with Au/Cr, and (d) optical picture of defect formation when the graphene target was scanned without using markers.

Au/Cr was chosen as the electrode and mask materials, because Au is electrically conductive and chemically inert enough under the harsh condition during oxygen plasma treatment. In addition, alkanethiol molecules, including ODT, easily form uniform SAMs at room temperature on the Au surface for creating patterns of the metallic layers. As an intermediate layer, Cr provided good conductivity and adhesion for Au on both the SiO_2 and graphene regions. To further confirm the graphene integrity protected by the Au/Cr layers through the whole processes, Raman spectra were collected in the beginning before and after the patterning processes on two graphene samples: 1) multilayer graphene without Au/Cr protection and 2) single-layer graphene protected by the Au/Cr layer (Figure 18). Initially, no obvious D band was observed in the spectra for both of the graphene samples (black solid lines in Figure 18a and 18b), indicating that the pristine samples had almost no defects in their structures. Without the protection, no peaks were observed in the spectrum at the original position of the graphene flake after oxygen plasma treatment (red solid line in Figure 18a), indicating that the multilayer graphene was completely etched away. To reduce optical attenuation of the protected single-layer graphene sample, an additional wet etching step for the Au/Cr layers was performed before the Raman spectrum were recorded. The spectrum (red solid line in Figure 18b) did not show any obvious change after the processes. Regardless of the number of graphene layers, it is evident that exposed graphene would be completely removed, and the structure could be well-preserved by the Au/Cr layer after the oxygen plasma treatment. It should be noted that no heating step was involved in the processes,

with even the thermal evaporation step maintained at a sample temperature below 100 °C.

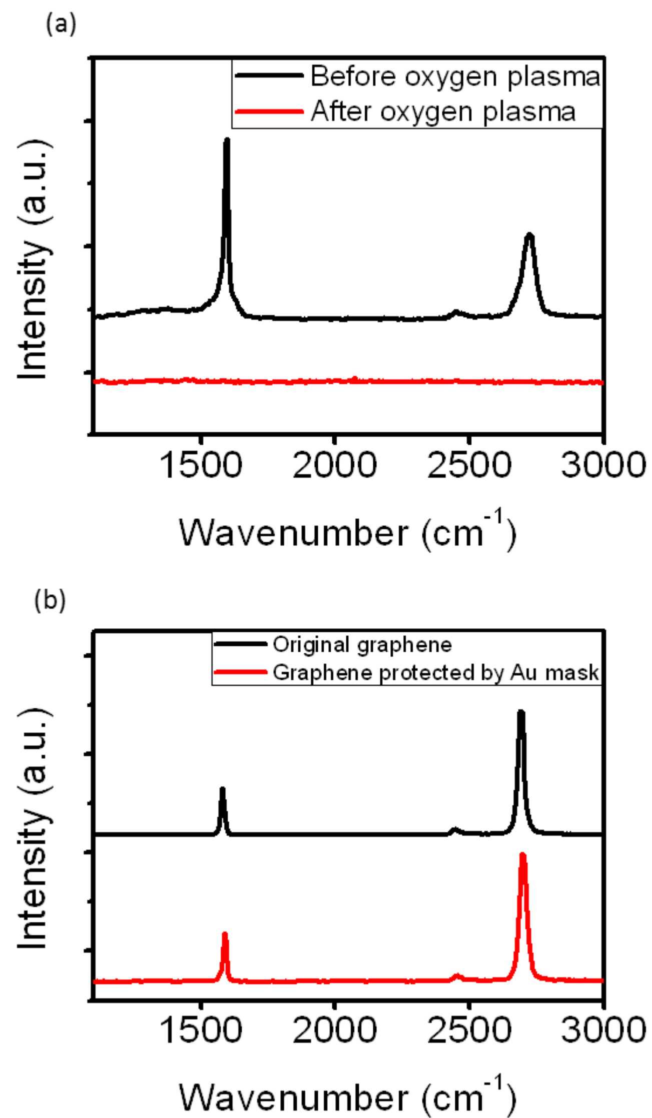

Figure 18. Raman spectra of (a) multilayer graphene, and (b) protected single-layer graphene before (black line) and after (red line) treatment of oxygen plasma.

Characterization of the graphene FET

The graphene field effect transistors were obtained through the fabrication processes described above. As shown in Fig 14h, the architecture contained a single-layer graphene stripe linked to two Au/Cr electrodes on top of a silicon substrate spaced by a thermal silicon dioxide layer. The number of the graphene layers was confirmed by Raman microspectroscopy prior to the fabrication processes. The final structure is shown in the AFM topographic image (Figure 19a), where the exposed stripe between both the electrodes had a width of ~ 130 nm and a length of ~ 480 nm. Relative to the electrode positions, the whole graphene flake was revealed by confocal Raman mapping of the graphene G band (Figure 19b). Although the optical resolution is diffraction-limited, the mapping clearly indicated that the thin stripe was connected to the electrodes from both the stripe terminals. The Au/Cr electrodes were served as the source and drain electrodes, with the silicon substrate as a back gate. The conductivity of the graphene stripe, proportional to the density of the charge carriers in the graphene stripe, can be tuned based on gate bias, spacing between the gate and the stripe, and the spacing materials. The specific capacitance, *c'*, can be expressed as:

$$c' = \frac{\varepsilon_r \varepsilon_0}{d},$$

where ε_r is the dielectric constant, ε_0 is the vacuum permittivity, and d is the thickness of the SiO_2 layer. The thickness of the oxide layer was determined to be 94.4 nm by spectroscopic ellipsometry. Based on the dielectric constant (3.9) of the thermally-grown silicon dioxide, its corresponding specific capacitance was estimated to be 36.6 nF/cm^2.

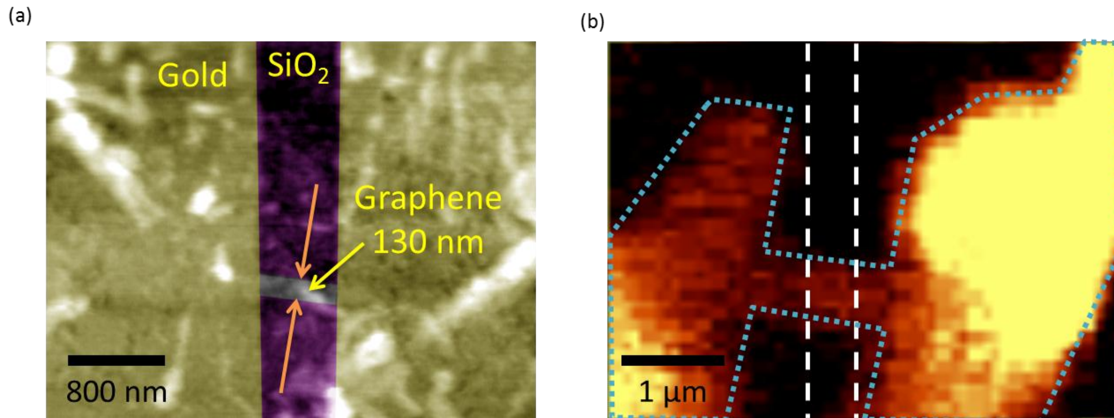

Figure 19. Characterization of graphene transistor: (a) AFM topographic image with false color, where the labels, Au and SiO2, indicate Au and oxidized Si wafer, respectively; (b) Raman mapping of graphene G band, where the white dash lines and blue dot lines indicate the edges of the gold electrodes and the graphene flake, respectively.

The electronic properties of the graphene were measured using standard lock-in techniques. The linear current–voltage characteristic shown in Figure 20a clearly depicts a constant total resistance of the graphene FET within the range of 0 to 0.9 V in ambient condition with $V_G = 0$ V. The constant resistance is also an indicator that good ohmic contacts between the electrodes and the graphene stripe can be made by this method. The total resistance (including the contact resistance and the resistance of graphene stripe) was ca. 2.79 kΩ, and the maximal current density was ca. 7.1×10^8 A/cm^2 assuming the thickness of single-layer graphene equals 0.34 nm. In order to further analyze the electrical properties of the graphene stripe, two-terminal resistances under various back gate voltages were measured (Figure 20b). Based on Drude's model, the two-terminal resistance R_t can be expressed as:

$$R_t = R_c + \frac{L/W}{n_c e \mu_{e,h}},$$

where R_c is the contact resistance, L and W are the length and width of the graphene stripe, μ_e and μ_h is the electron and hole mobility, respectively, e is elementary charge, and n_c is the charge carrier concentrations (electrons or holes) in the graphene stripe. The n_c can be calculated approximately as:[114]

$$n_c = \sqrt{n_0^2 + \left(\frac{c'|V_g - V_D|}{e}\right)^2},$$

where n_0 is the charge carrier concentrations at the Dirac point, c' is the specific capacitance of the silicon dioxide layer, V_g is the gate voltage, and V_D is the Dirac voltage. The fitting of the equations on measurements is also shown in Figure 20b. The modeling equations agreed very well with our experimental data. The electron and hole mobilities of this device were estimated to be 1580 and 1670 $cm^2/V{\cdot}s$, respectively. The corresponding minimum conductivity was 360 μS, calculated when V_g was equal to V_D. the lower values of the mobilities might be due to some absorbents and in the wet chemistry processes. The Dirac point away from 0 V indicated the p-type doping from the absorbents introduced in the ambient environment, which also decreased the carrier mobility[85].

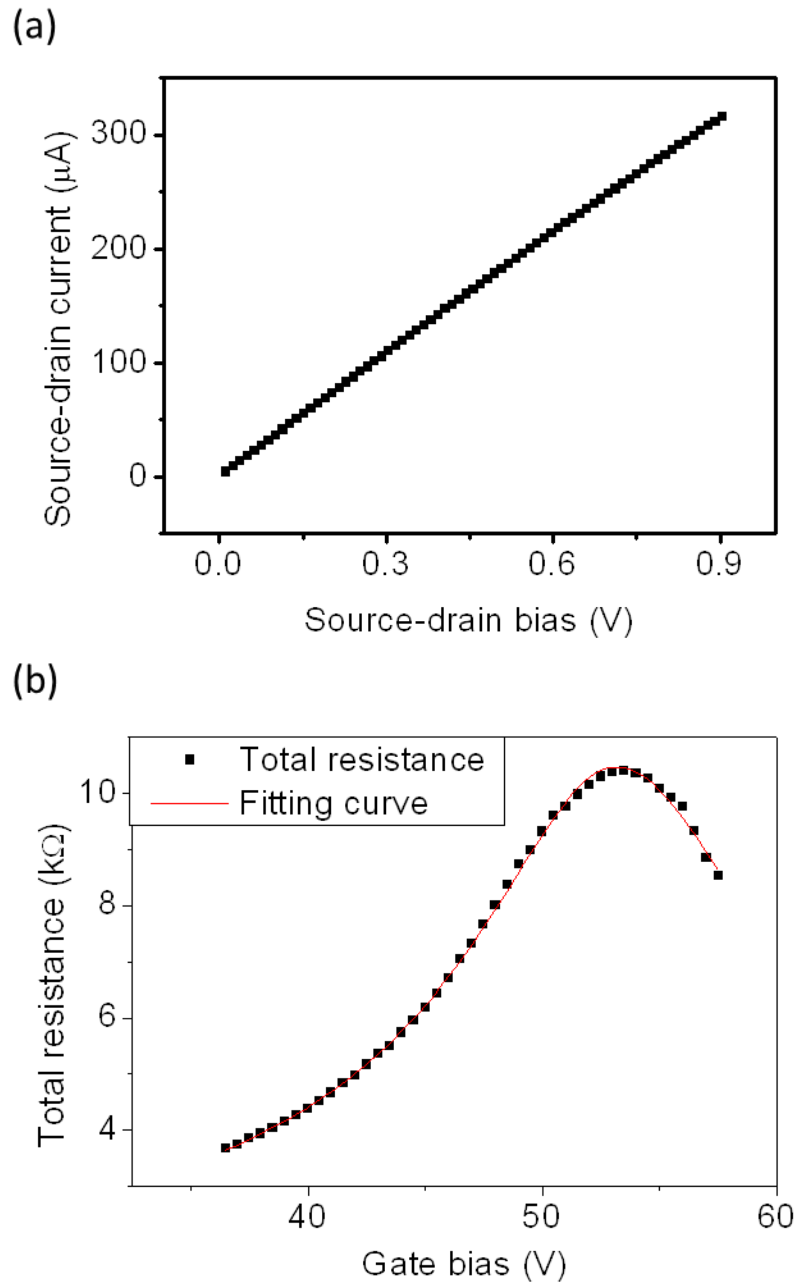

Figure 20. Electrical measuremnets of graphene transistor: (a) curve of source-to-drain current at various source-to-drain bias with a gate bias of 0 V, and (b) fitting curve of total resistance at various gate bias with a source-to-drain bias of 0.1 V.

A photo-sensing experiment was demonstrated for the optoelectronic applications. A composite FET of porphyrin and graphene was made by drop-casting 1 uL of 1mM tetra-*tert*-butyl phthalocyanine acetone solution on a graphene FET. The photo-gating behavior shown in Figure 21 was measured continuously at a sampling rate of 8 Hz. A source-drain bias of 0.141 V and a gate bias of 57.5 V were applied. An optical shutter in front of an incandescent lamp was turned on and off periodically at a frequency of 0.05 Hz to create a square wave of illumination intensity. The whole FET was illuminated under the power density of 42 mW/cm^2 when the shutter was on, while the off power density was 6.4 $\mu W/cm^2$ due to our lab environment. When the composite FET was exposed to light, the excited phthalocyanine molecules near the graphene channel may further alter the charge carrier concentration in the graphene channel. In this example, the charge carrier concentration was controlled at the hole doping region. The current was decreased immediately when the composite FET was illuminated. As such, the photo-gating introduced electron doping to the graphene, and thus depleted the available charge carriers.

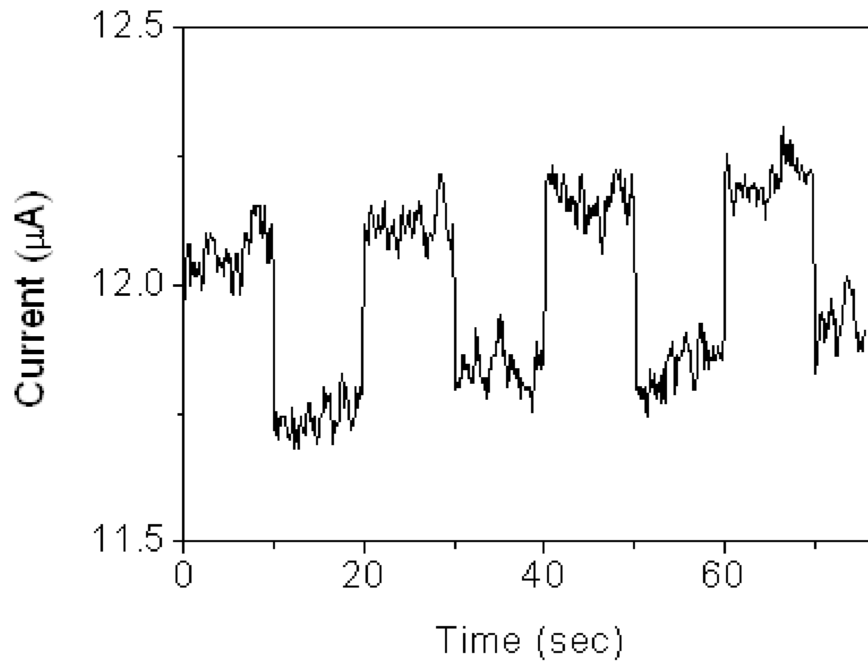

Figure 21. Photo-gating current of porphyrin-graphene composite FET.

3.4 Conclusion

In conclusion, we reported the patterning technique of graphene and electrode layers based on AFM nanoshaving nanolithography. The technique not only offers a simple, flexible, and low-cost method to create complex patterns for graphene FETs without using expansive e-beam or photolithographic equipment, but also produces a reliable contact between each layer even under a large current density. Moreover, the original structure of the graphene crystal can be well-preserved as well. The electrical properties of the single-layer graphene FET and porphyrin-graphene composite FET

made by this approach were tested. As such, the technique may be used in the related fields, such as chemical sensing and graphene electronic applications.

CHAPTER IV

IN SITU MONITORING PLATFORM FOR NANOLITHOGRAPHY ON CONDUCTING PROBE ATOMIC FORCE MICROSCOPE COUPLED WITH TIP-ENHANCED RAMAN SPECTROSCOPY

4.1 Introduction

Nanopatterning of surfaces using atomic force microscopy (AFM) has been proven to be a useful method to create surface features with a resolution down to a few to tens nanometers.[93] In general, AFM based lithographies use a very sharp tip, with a radius of curvature of about 10 nanometers, to locally define a region where chemical composition, surface morphology, or oxidation states are altered relative to the surrounding surface. Based on the manipulating mechanisms, AFM nanolithography includes nanoshaving, nanografting, dip-pen, as well as electrochemical and thermal nanolithography.[95-99,125] The modification can be further characterized *in situ* by various AFM techniques, such as contact-mode or tapping-mode AFM, lateral force microscopy, electrostatic force microscopy, etc. These AFM-based techniques mainly rely on the force contrast between the modified and unmodified regions due to different tip-sample interactions, while local chemical information requires further spectroscopic identification.

Several significant challenges to monitoring nanolithography processes are that the AFM measurements can not be performed during the processes, and do not provide the chemical detail of the modification. As such, the resulting modifications can only be

detected by the contrast between the modified and unmodified regions after the nanolithographic steps have been performed. In addition, the AFM image contrast arises from various complicated factors, such as physical and chemical properties of samples, water meniscus formation, tip material and shape, contact area, as well as surface structure. It is difficult to fully understand the detail of the modification.[26] Inelastic electron tunneling spectroscopy (IETS) combined with scanning tunneling microscope can obtain vibrational spectra for identification of analytes with high sensitivity, good spectral resolution, and high spatial resolution.[27] However, IETS requires current measurements across analytes at very low temperature, which is intrinsically incompatible to AFM nanolithography. Several approaches, including infrared absorption, sum frequency generation, and high-resolution electron energy loss spectroscopy, have been proposed to characterize the chemical species on a sample surface.[28,29] Among these methods, resolving chemical composition in a nanoscale under ambient conditions remains a challenge.

Alternatively, tip-enhanced Raman scattering (TERS) has been recently proposed to identify molecular composition in the nanometer scale by analyzing the enhanced Raman scattering (RS) near the apex of a metal-coated tip.[126] Typically, RS provides vibrational spectra to directly identify analyte molecules. It should be noted that RS is an optical technique under various environments, such as air[32] water,[36] and vacuum,[127] which allows TERS to be measured simultaneously with AFM nanolithography. Wide choice of TERS excitation wavelength[39,128,129] from deep UV to visible light makes it even compatible to photolithography. *In situ* modification and detection on the same

AFM instrument also provide a convenient platform for pattern creation and characterization. Moreover, recent investigations also indicate the spatial resolution of TERS can reach about 10~20 nanometers,[58,130,131] which matches the resolution of AFM nanolithography. Several studies have shown the detection sensitivity has been improved to reach a single-molecular level by the same mechanisms of surface-enhanced Raman scattering including the electromagnetic mechanism and the chemical enhancement.[31,32,132,133] The former mechanism, responsible for the majority of the enhancement, relies on the localized field amplification near the metallic tip apex when the localized surface plasmon at the apex is in resonance with the RS photons and the excitation laser. The later mechanism describes that the charge transfer, occurring in direct contact between a metallic tip and analytes, creates additional RS pathway and thus increases the RS probability.

In this paper, we demonstrate that the modification induced by AFM nanolithography can be monitored simultaneously on the same platform by TERS. The modification was carried out by applying an electric bias between a conductive tip and a conductive substrate, while the TERS analysis was performed at the same time on the combination platform of conductive-probe AFM and TERS. Several model samples, including multilayer graphene on silicon wafer (MLG on Si), rhodamine 6G on silver films (R6G on Ag), and self-assembled monolayers of mercaptobenzoic acid on gold films (MBA SAM on Au), were chosen to demonstrate this concept.

4.2 Experimental

The system designed for conductive-probe AFM and TERS is shown in Figure 22. This system consists of a commercially available AFM (WITec alpha 300), electronic components for providing electric bias, and an optical setup for TERS measurement. The optical setup is similar to the setup reported by Yi et al.[131] The collimated beam of a 488 nm Ar ion laser was focused to the apex of a silver-coated tip for RS excitation at the angle of 60° relative to the tip axis by a long-working-distance objective (Obj, Mitutoyo 10X Infinity-Corrected Long WD Objective). The power of the laser before the objective was controlled at relatively low levels to prevent samples from photo-degradation. Two movable mirrors were inserted before the objective in order to tilt the optical axis and to control the position of the focused laser spot coarsely. Two cameras, responsible for top view and side view (Figure 22 TC and SC), were mounted to the optical path to help the alignment process. Scattering photons near the tip apex were collected by the same objective and focused onto a spectrometer (Andor DV401-BV). An edge filter (Figure 22 FT, Semrock long-pass edge filter LP02-488RE-25) was inserted before the spectrometer to remove Rayleigh scattering. The tip and the sample substrate were linked to a power supply (Figure 22 PS, Xantrex XTS1J-4X) and a current meter (Figure 22 A, Mastech MAS-344) equipped with a current amplifier (Femto, DLPCA-200) for the electrical measurements. All the information including images, spectra, AFM data, and electrical bias were recorded simultaneously.

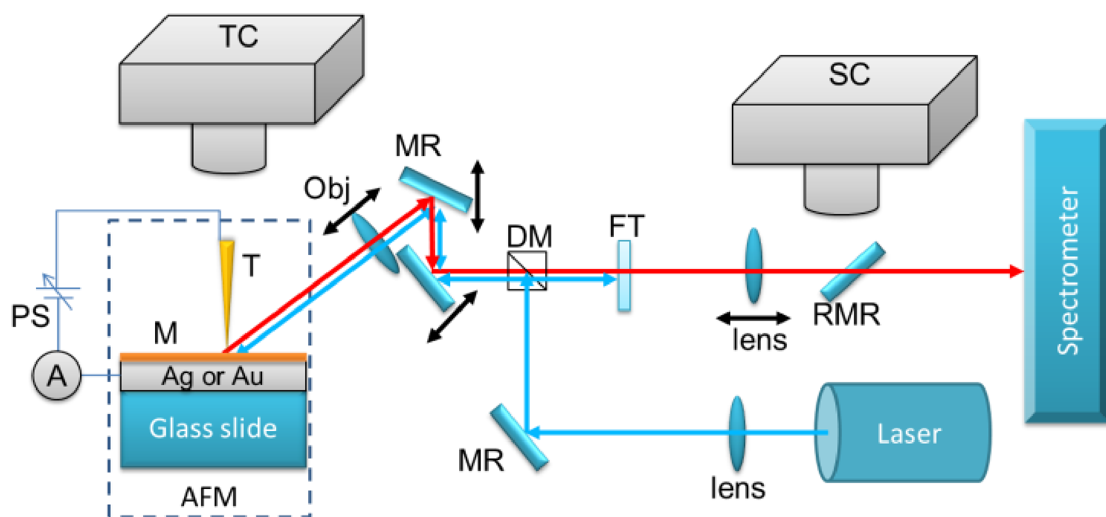

Figure 22. Instrumental setup for the combination of conductive-probe AFM and TERS. A: current meter; AFM: atomic force microscopy; DM dichroic mirror; FT: Raman filter; M: analyte molecules; MR: mirror; Obj: long-working-distance objective; PS: power supply; RMR: removable mirror; SC side-view camera T: silver-coated tip; TC: top-view camera. Red lines, blue lines and black lines indicate Raman scattering, laser beam, and movable direction of optical components, respectively.

The alignment between the AFM tip and the focused spot of the laser was achieved through the following steps. First, the tip was approached on the sample substrate and the contact point was recorded by the top and side camera. Then, the focused spot was adjusted coarsely to the position of the contact point by controlling two movable mirrors and the objective. Finally, the tip position was located with fine adjustment by the piezo-actuator according to the intensity of the inelastic scattering signal monitored by the spectrometer. When the AFM tip and the focused spot of the laser were in a good alignment, the inelastic scattering was maximized and the laser scattering from the tip-substrate junction observed in the camera was also maximized.

All tips (Nanoseosors ATEC-CONT) were coated with nominal 5 nm of chromium for better adhesion and then nominal 50 nm of silver for TERS by thermal evaporation. The thickness of each layer was monitored by quartz crystal microbalance (QCM) equipped in the evaporation chamber. These tips protrude out from the very end of the lever, allowing the tip-sample junction to be accessible to the optical setup from the side without being blocked by the lever. The metal deposition rate was set at ~0.01 nm/s to prevent tips from deforming during coating. Due to the ready oxidation of silver in air, the tips were stored in a vacuum desiccator immediately and used within one day to prevent them from suffering inconsistently diminished TERS activity. The sample substrates, glass cover slides, were modified by coating layers of chromium (5 nm) and silver (50 nm), or of chromium (5 nm) and gold (50 nm) under the same conditions as the tips.

The MLG samples were mechanically exfoliated from highly ordered pyrolytic graphite (SPI) and deposited on silicon wafer (Virginia Semiconductor). R6G samples were prepared by spin-coating 2.5×10^{-5} M R6G (Sigma) ethanol solution on silver-coated glass at the spin rate of 2000 rpm for 2 min. MBA samples were prepared in two methods. For the MBA SAMs on gold films used for TERS experiments, a gold-coated glass was immersed in MBA (Aldrich) ethanol solution at the concentration of 1×10^{-3} M for 12 hr. to absorb a uniform MBA monolayer. The as-prepared SAM samples were rinsed with copious amount of ethanol to remove excess MBA, and dried under strong N_2 gas. For the MBA coated on silver film used for Raman references, a silver-coated

glass was spin-coated with 1×10^{-3} M MBA ethanol solution at the spin rate of 2000 rpm for 2 min.

4.3 Results and discussion

Morphologic characterization

In order to alter the local chemical composition by an electrical bias and monitor TERS signal at the same time, both the tip and the substrate are required to be conductive, and the tip has to be TERS-active. The surface of the tips and the sample substrates were deposited by chromium and then silver through thermal evaporation to ensure their conductivity, TERS activity, and adhesion. The typical scanning electron microscope (SEM) images of a silver-coated tip are shown in Figure 23a. The continuously grainy structure of the silver coating covers the whole surface of the AFM tip uniformly, which ensures the tip with good conductivity. Previous study[58] has already pointed out that the spatial resolution of TERS is about or less than the size of the tip apex. The tip radius estimated from the SEM image is about 46 nm, which provides not only strong enhancement of RS but a spatial resolution in nano scale. During the thermal evaporation, a fast coating rate (> 0.1 nm/sec) may cause the deformation of the tips due to heat transfer. As such, the coating layer may have poor adhesion to the tip surface and thus part of the surface may not be coated especially near the tip apex. Therefore, the coating rate was set at ~0.01 nm/s to increase the reproducibility of tips with good TERS activity.

The analytes were prepared as a thin and smooth layer to decrease variations and artifacts in the Raman signals and to ensure strong plasmonic coupling between the tips and sample substrates. The MLG samples were characterized by AFM and shown in Figure 23b. The MLG sample has a very smooth surface and its thickness near the spot A is ~34 nm. For the silver-coated glass, the surface topography and the thickness of the coated layers on the glass slides are shown in Figure 23c. The grooves in the images were created to measure the film thickness. The averaged thickness of the metallic layers was ~73 nm, with a root-mean-square roughness of 3.9 nm measured over 36 μm^2. Following the addition of R6G to the surface, the film thickness was found to be ~75 nm (Figure 23d), indicating that merely a thin film has been added to the surface. The AFM picture of MBA SAM (Figure 23e) also indicates a smooth monolayer is formed on a gold film.

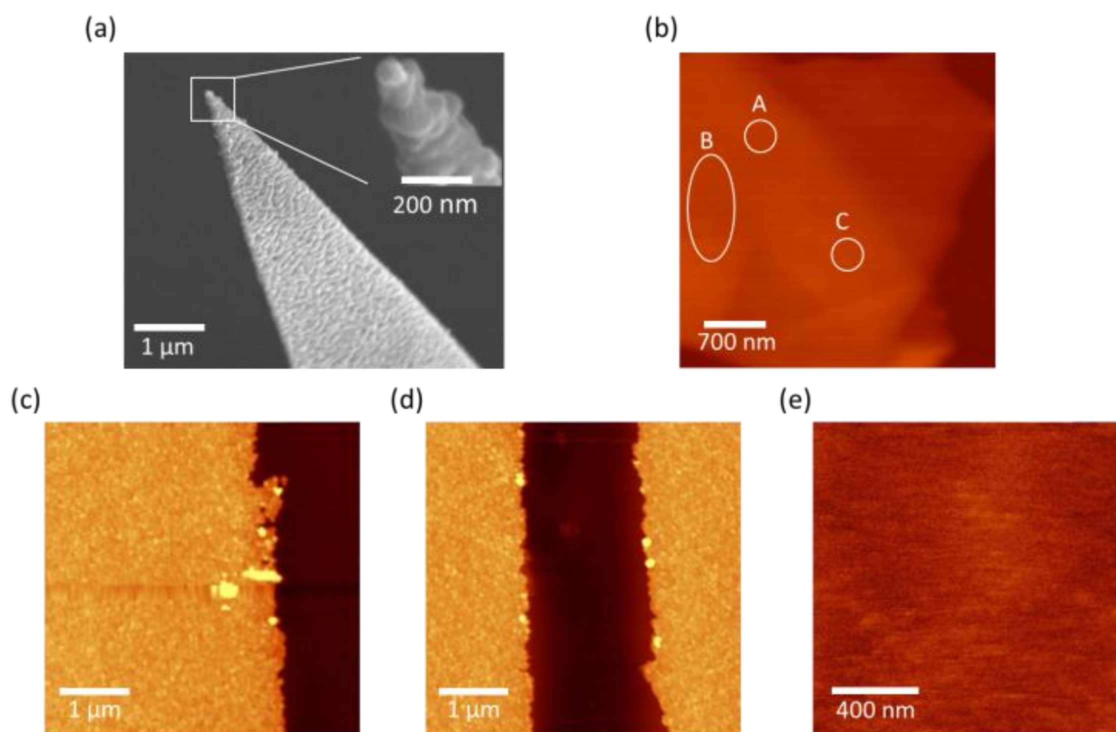

Figure 23. Tip and sample characterization: (a) SEM picture of a silver-coated tip (inset: zoom-in picture near the tip apex), (b) AFM picture of MLG on Si (the spots A, B, and C indicate the positions for the AFM nanolithography), (c) AFM picture of Ag film on glass, (d) AFM picture of the sample in (c) spin-coated with R6G, and (e) AFM picture of MBA SAM on Au film,

Raman signal gain due to tip-enhancement

Typical Raman spectra of MLG on Si, R6G on Ag, and MBA on Ag are shown in Figure 24. These spectra are in good agreement with those reported in literature,[134-136] and the characteristic peaks are assigned and summarized in Table 2. The Raman spectra of MLG on Si were averaged over 100 sec under the excitation power density of 5.3×10^5 W/cm^2, the R6G spectra were averaged over 500 sec under the excitation power of 4.4×10^3 W/cm^2, and the MBA spectra were averaged 25 sec under 9.5×10^4 W/cm^2.

The total collection time and excitation power varied among these samples mainly because of the differences in their Raman cross-sections, photo-stability, and desired signal-to-noise ratios. The angles of the incident laser and the collection were along the sample surface normal for the optimal collection efficiency. We used silver films as substrates for R6G and MBA, because silver will quench fluorescence from R6G and increase Raman signal dramatically. Thus, their spectra showed reasonable signal-to-noise ratios and flat backgrounds.

Table 2. Raman assignment of MLG on Si, R6G on Ag, and MBA on Ag.

MLG on Si		R6G on Ag*		MBA on Ag*	
Stokes-shift (cm^{-1})	Assignment	Stokes-shift (cm^{-1})	Assignment	Stokes-shift (cm^{-1})	Assignment
1578	G band	609	C-C ring ob.	1080	As.
2731	2D band	773	C-H ob.	1181	C-H bending
		1129	C-H ib.	1367	COO- s.
		1189	As.	1586	As.
		1361	As.		
		1508	As.		
		1574	As.		
		1649	As.		

* as: aromatic C-C stretching; ib: in-plane bending; ob: out-of-plane bending; s: stretching.

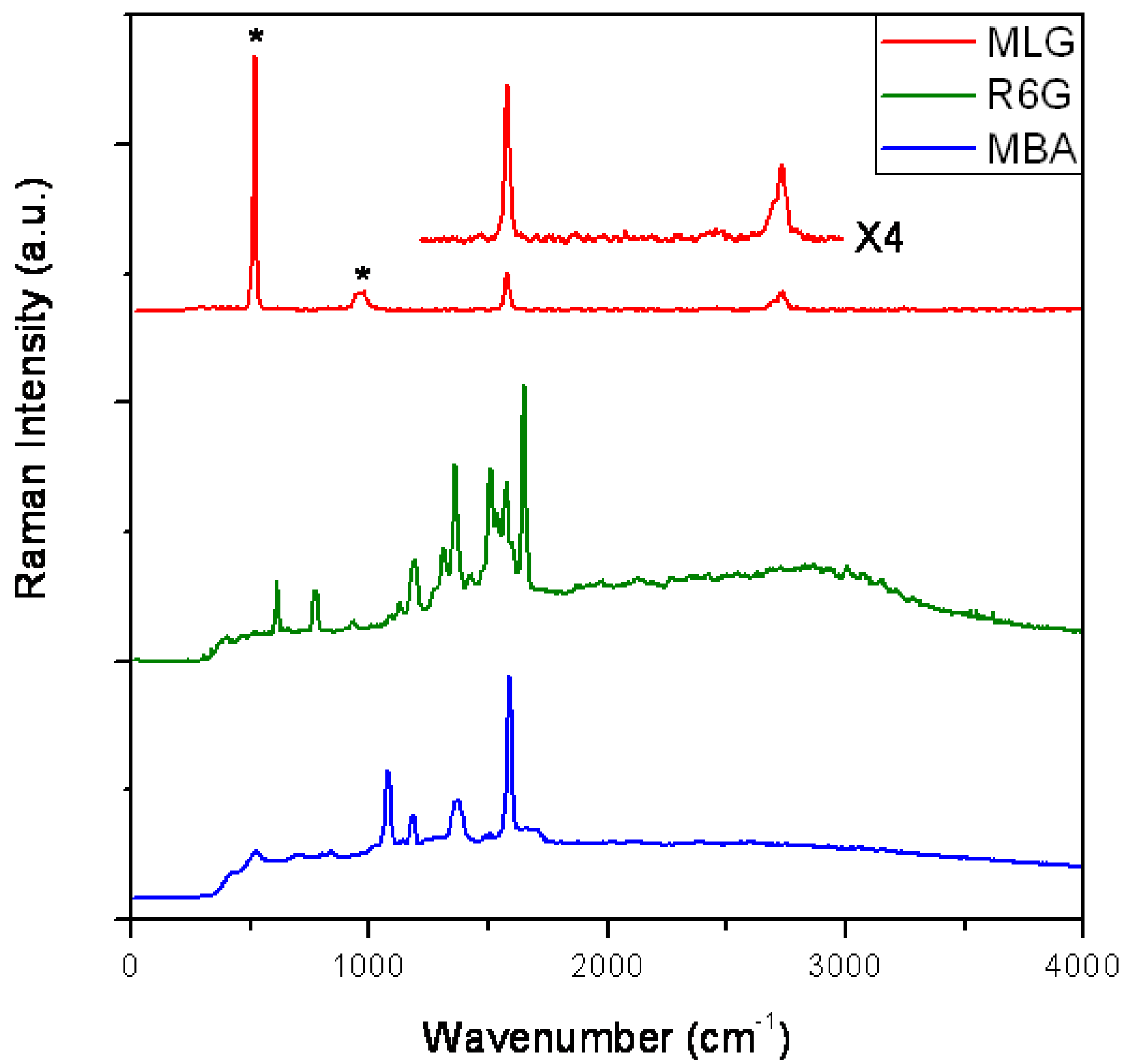

Figure 24. Raman spectra of MLG on Si wafer (red line), R6G on Ag film (green line), and MBA on Ag film (blue line). * indicates the peaks from silicon wafer.

The tip enhancement is shown in Figure 25 for the samples: MLG on Si, R6G on Ag, and MBA SAM on Au. Comparing the spectra when the tip is in contact (red lines) with the spectra when the tip is retracted (blue lines), it is obvious that the Raman intensity is increased among all samples when the silver-coated tip is in contact. Especially in the case of MBA SAM on Au, the enhancement is much stronger than that in the other samples, because the smallest gap between the tip and the substrate yields the strongest tip-substrate coupling.[127] Due to the need of a short collection time (1 sec), the spectral resolution among these spectra was reduced to 20 cm^{-1} to achieve reasonable signal-to-noise ratios. In order to ensure that the tips did not influence the collection of normal Raman spectra, the tip was retracted for at least 100 μm away from the sample surface, when the Raman spectra without the tip enhancement were collected. During the removal of the tip, the AFM force feedback was turned off to maintain the sample position and the same alignment relative to the laser beam.

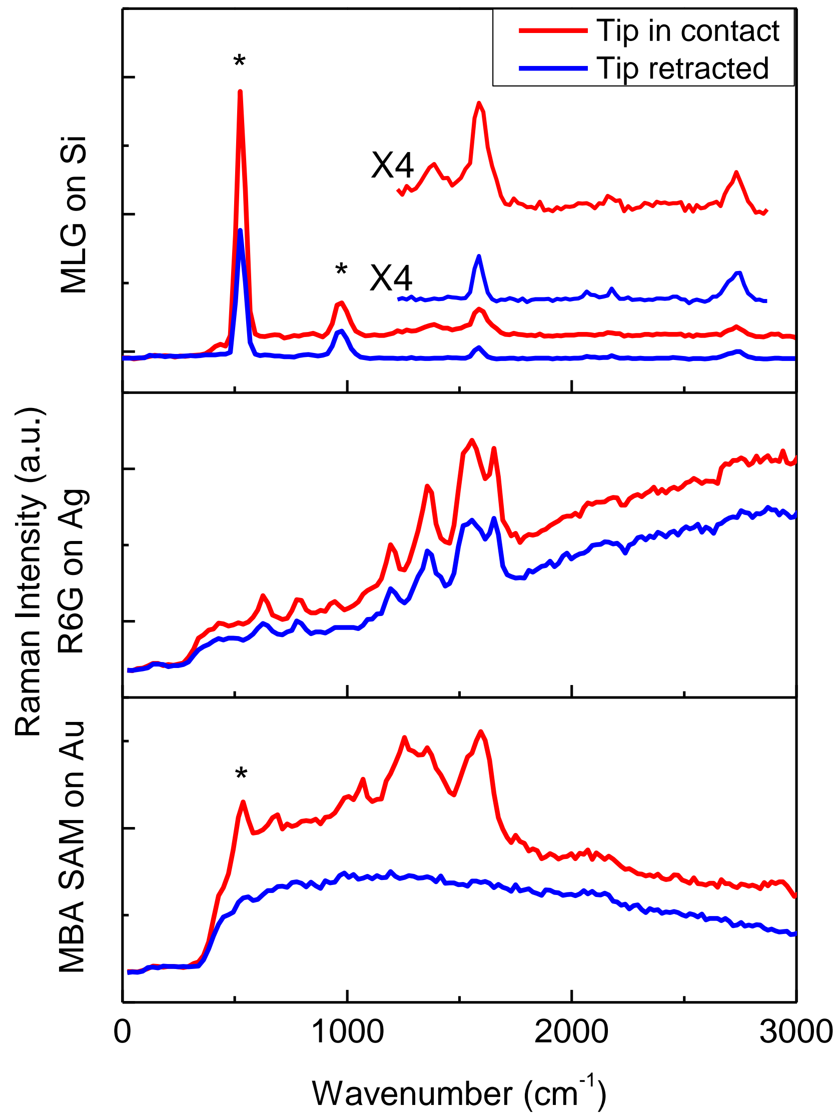

Figure 25. TERS (red line) and Raman spectra without tip enhancement (blue line) of MLG on Si, R6G on Ag, and MBA SAM on Au. * indicates the peaks from silicon wafer.

The tip enhancement was estimated based on the intensity ratio on both the tip-enhanced spectrum and the spectrum without the enhancement, as shown below:

$$Enhancement = \frac{I_{near}}{I_{far}} \times \frac{A_{far}}{A_{near}} = \frac{I_{total} - I_{far}}{I_{far}} \times \frac{A_{far}}{A_{near}},$$

where I_{near} is the near-field Raman intensity from the tip-substrate gap, I_{far} is the far-field Raman intensity from the laser focused region, I_{total} is the total Raman intensity from the near and far field, A_{near} is the area in which RS can be enhanced by tip-substrate coupling, and A_{far} is the area of the focused laser spot. I_{far} is obtained directly from the Raman intensity of the spectra (Figure 25 blue spectra) when the tip is retracted, and I_{total} is from the TERS intensity (Figure 25 red spectra). A_{near} was calculated based on the tip radius obtained from the SEM images (Figure 23), and A_{far} was determined from fitting the beam profile of the focused laser spot. The calculation of the tip enhancement (Table 3) was based on the assumptions: first, the local thickness of the analyte thin film is uniform; second, A_{near} is much smaller than A_{far}. According to the AFM analysis and the SEM images mentioned above, the assumptions here are generally valid. Because the Raman spectra for MBA SAMs without the enhancement were below our detection limit, the tip enhancement can only be estimated by replacing I_{far} with the noise level in the MBA spectrum.

Table 3. Tip enhancement calculation of MLG on Si, R6G on Ag, and MBA SAM on Au.

Sample	Tip enhancement
MLG on Si	6.5×10^3
R6G on Ag	3.1×10^3
MBA SAM on Au	2.9×10^5*

* indicates that the enhancement is estimated by replacing the far-field Raman intensity with the noise level in the MBA spectrum.

Among these samples, MBA SAMs on Au shows the highest enhancement ratio. It should be noted that the enhancement calculation was an underestimation, because the signal level of the Raman spectrum from the MBA SAMs was under our detection limit. Compared with the other samples, MBA SAMs on Au had the smallest gap, only spaced by a monolayer of MBA molecules. The plasmonic coupling between the silver-coated tip and the gold-coated substrate is strongly dependent on the tip-substrate distance.[127] Moreover, the gold film itself does not provide such a strong enhancement compared with a silver film. It should be noted that the enhancement ratios calculated here are the intensity ratio between tip-substrate enhancement and substrate enhancement, rather than the factor between tip-substrate enhancement and molecules without any enhancement. Therefore, the ratios are lower than the reported enhancement factors (10^6-10^8) on similar TERS arrangement.[137,138]

Monitoring modification induced by AFM tip bias

To demonstrate that the modification induced by AFM tip bias can be detected, the TERS spectra were continuously monitored before an electric bias was applied between silver-coated tips and conductive sample substrates. The detection of the chemical modification by AFM nanolithography is shown in Figure 26. The on/off ratio in Figure 26 is defined as:

$$I_{on/off} = \frac{I_{on}}{I_{off}},$$

where $I_{on/off}$ is the TERS intensity ratio, I_{off} is the TERS intensity when the bias between the tips and the sample substrates was turned off, and I_{on} is the TERS intensity when the bias was on. Theoretically, the ratio will maintain unity if there is no change due to the electric bias or current. Among all samples, the on/off ratios of analyte molecules (MLG, R6G, and MBA) were lower than 1 (in the range from 0.7 to 0.75). The possible reasons include: first, the electric bias and current caused evaporation or decomposition of the analyte molecules near the junction between the tip and the substrate; second, the enhanced laser near the tip apex caused decomposition due to photobleaching; last, the tip lost its activity of Raman enhancement. The further reference experiments confirmed that the tip was still TERS-active, and thus the last reason is less possible. In order to make sure that the TERS intensity drops were not caused by photobleaching, the applied bias was gradually increased from 2 V to 7 V on the sample of R6G on Ag. Figure 26b shows

an obvious drop in the on/off ratio when the bias reach 7 V. The Raman intensity due to photobleaching should decay gradually instead of suddenly drop at 7 V, and it should be dependent on the exposure time and the laser power density rather than the applied bias. In addition, the power of the laser before the objective was always controlled at a relatively low level. Therefore, the drop of the TERS signal was attributed to the local removal of the analyte molecules induced by the bias. The AFM scanning (Figure 27) also indicated the local removal of the analyte molecules. In the case of MLG on Si, a small pit was generated after a bias of 7 V was applied for 10 sec by comparing the original AFM image (Figure 23b spot A) with the image after bias (Fig. 6a. spot A). The cross-sectional profile (Figure 27b) across the spot A in Figure 23b shows that the size of the etched pit was comparable to the size of the tip. For MBA SAM on Au, the local modification after the bias was also observed in the AFM friction images (Figure 27c and Figure 27d).

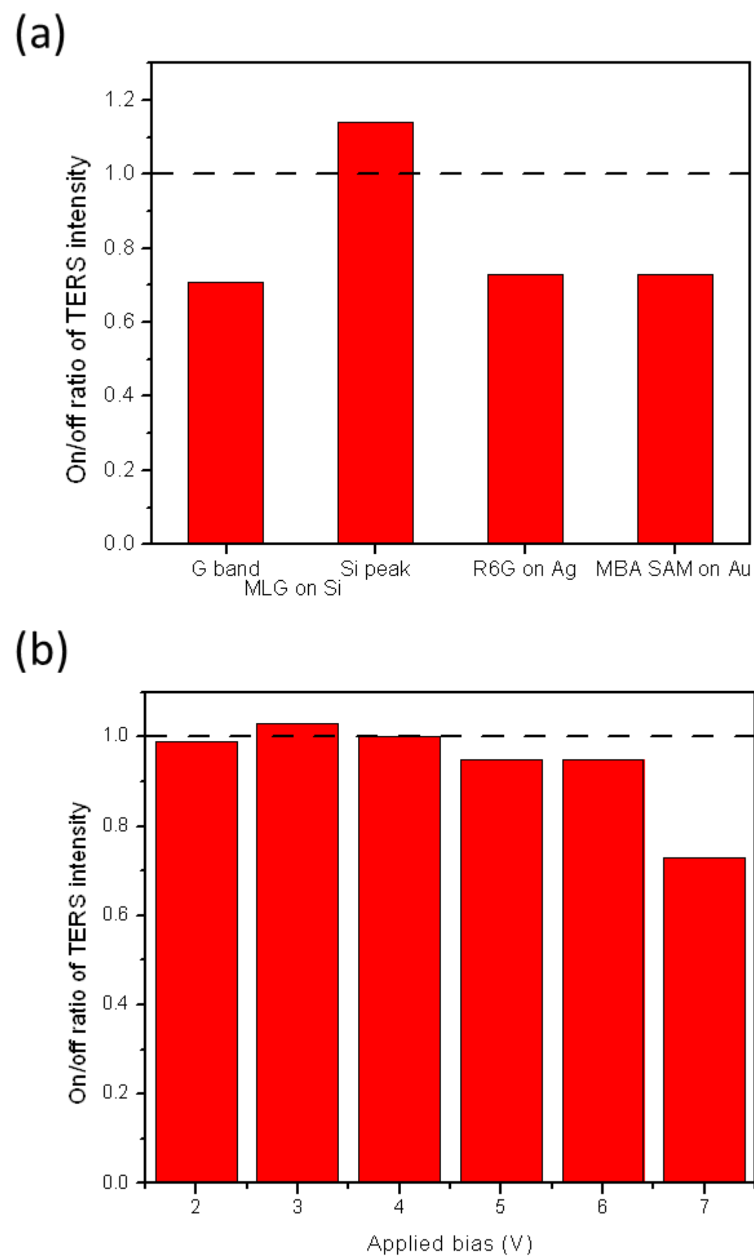

Figure 26. Bias on/off ratio of TERS intensity of (a) MLG on Si wafer, R6G on Ag film, and MBA on Ag film, and (b) R6G on Ag film over various biases applied between the tip and the Ag film. Dash line indicates the unity ratio.

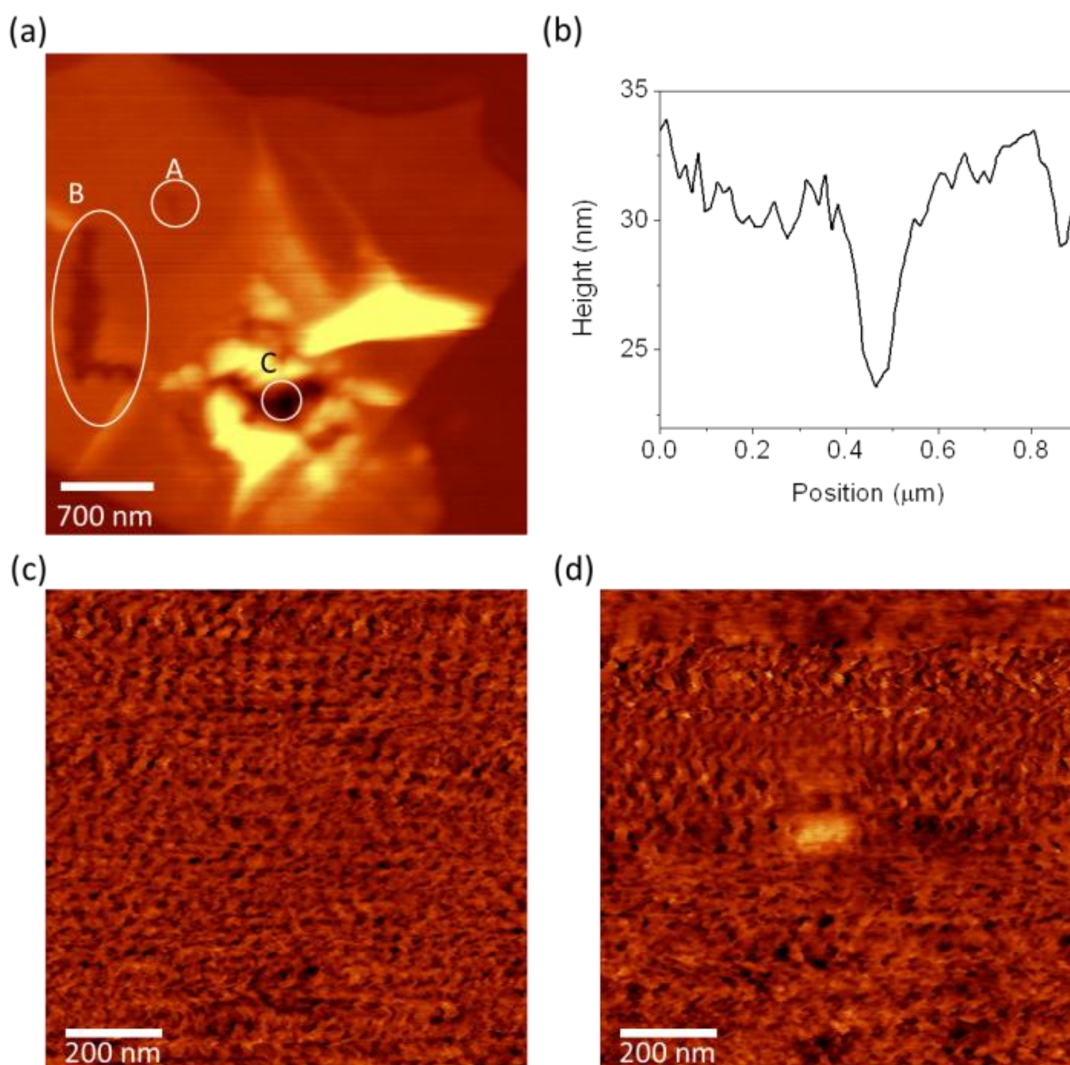

Figure 27. Sample characterization: (a) AFM topographic image of MLG on Si wafer after several nanolithographic steps (the spots A, B, and C indicate the positions for the AFM nanolithography.), (b) cross-sectional profile in the spot A in (a), (c) AFM friction image of MBA SAM on Au film before nanolithography, and (d) AFM friction image of MBA SAM on Au film after nanolithography.

Alternatively, the on/off ratio of Si Raman peak of MLG on Si also suggests the local removal due the tip bias. The local removal of carbon atoms near the tip apex

shortened the distance between the tip apex and the surface of the Si wafer. As such, Si Raman intensity can be further enhanced due to the TERS distance dependance,[127] which caused the Si on/off ratio higher than 1. Another two experiments further demonstrated that only the carbon atoms below the tip apex were locally removed. First, after a bias was turned on, the tip was moved downward for 1 μm and then moved to the right for 0.5 μm to write a letter, "L". The L-shaped groove shown at the spot B in Figure 27a matched the path of the tip, indicating only the carbon atoms below the apex were removed. Second, the tip was maintained at the spot C in Figure 27a for 160 sec after a bias was turned on. After 160 sec, Figure 27a shows a large hole is etched at the spot C. The local structure of MLG near the spot C is deformed, because the hole is large enough to allow the tip touching the lower surface of Si wafer and locally oxidizing Si. As such, the Si surface is locally altered as well as the MLG surface.

The chemical information detected from TERS provides a useful feedback to monitor the modification processes during AFM nanolithography. To fully understand the processes, the TERS collection speed has to be faster than the rates of AFM nanolithography, which can be realized by optimize the tip enhancement. Due to their strong dependence on the tip enhancement, this optimization may involve tip size and shape[59], local dielectric constant,[31] matching laser wavelength with TERS plasmonic resonance[39], etc. Considering several studies with a similar TERS setup report the tip enhancements in the range from 10^7 to 10^8,[32,137] the monitoring speed can be greatly improved. On the other hand, metal tends to oxidize in air, especially in the case of utilizing silver to obtain Raman enhancement. Silver and gold, used to obtain TERS

activity are softer than many common substrates, such as glass. Recent investigation suggests that adding a thin protecting layer on metal may extend the active lifetime of tips.[139] As a result, this approach can be fully integrated with AFM nanolithography with higher sensitivity and better durability.

4.4 Conclusion

This work demonstrates that the modification made from AFM nanolithography can be simultaneously detected on the same platform. The local decomposition for a single nanolithography step was successfully observed from our combined system among several analytes including MLG, R6G, and MBA. The instant chemical information provided from the system immediately exhibits the nanolithography progress without the need of AFM post-scanning. The silver-coated tip can enhanced Raman signals in the range from 10^3 to 10^5, which provides reasonable sensitivity and spatial resolution. In addition, the combined system should be able to be easily adapted to other types of AFM nanolithography, and has a great potential on various research fields, such as nanotechnology, material science, and nanobiology.

CHAPTER V

NOVEL AND EASY-TO-USE TIP-ENHANCED RAMAN SPECTROSCOPY ON OPAQUE SUBSTRATES WITH A MICRO-SIZED MIRROR AND A SILVER-NANOWIRE TIP

5.1 Introduction

Tip-enhanced Raman spectroscopy (TERS) is a useful tool for chemical analysis with high sensitivity[30-32] and high spatial resolution[33-35] at vacuum, ambient condition, or even in liquid environment[36] without any sample treatments. The potential applications in TERS have been demonstrated in various fields, such as biochemistry,[140,141] chemistry[142,143], material science[33,34], etc. The integration of optical spectroscopy and scanning probe microscopy allows structural information in nanoscale on sample surface to be obtained simultaneously. Among scanning probe microscopic methods, atomic force microscope (AFM) is frequently used due to the compatibility with both conductive and nonconductive samples. The strong Raman enhancement is tightly confined within a tip-sample junction due to the tip sharpness and dramatic distance-dependence.[127,144] Similar to the mechanism of surface-enhanced Raman spectroscopy (SERS), the electromagnetic field strength is greatly increased at close proximity to nanoscale structures or junctions of noble metals, such as silver or gold, when the field couples with localized surface plasmon of the metals.[145] The terminal structure of a metal tip used in TERS, therefore, plays an important role responsible for localized Raman enhancement, and thus detection sensitivity as well as spatial resolution.[59,146]

However, typical methods for AFM tip preparation, such as physical vapor deposition, don't yield a consistent result in controlling tip-shape in nanometer scale and thus tip-enhancement.[38,45]

Several sample limitations exist in terms of TERS instrumental arrangement of laser excitation reported in literature, including: 1) bottom illumination,[60,61] 2) side illumination,[62,63] and 3) parabolic mirror illumination.[64,65] In the bottom illumination setup, the laser is tightly focused by a high NA objective of an inverted microscope, and used to excite a metal tip from the bottom of the tip and samples. Obviously, the sample transparency is required and the sample thickness is limited within the distance between the tip and the objective. In the side illumination configuration, a long-working-distance objective is generally used to excite the tip from the side with an angle of 40º - 60º relative to the tip axis. The sample dimension is still limited to the available space between the tip and the objective. In addition, the tilted optical path increases much complexity in the arrangement and the alignment of the optical components in this configuration. For the parabolic mirror illumination, a collimated laser beam with a large diameter is brought to a focusing parabolic mirror from the bottom of the sample, and focused to the tip-sample junction. Therefore, the sample lateral dimension has to be much smaller than the collimated beam size.

Here, we proposed a tip preparation method and a TERS configuration that overcome the issues mentioned above. A micro-sized mirror was introduced in the configuration under an objective lens to reflect the laser onto the side of the tip, which allows the main optical path parallel to the AFM tip axis. For the tip preparation, silver

nanowires suspension solution was obtained through a polyol synthesis at first, and a suitable nanowire chosen under optical microscope was mounted on an AFM tip by suitable adhesive. The performance of the TERS configuration and the silver nanowire tip were investigated in this paper.

5.2 Experimental

TERS configuration.

This TERS system was obtained by modifying a commercially available AFM (WITec alpha 300). The setup is illustrated in Figure 28a, and its side-view is shown in Figure 28b. Two laser systems for Raman excitation and AFM force feedback were introduced into the TERS configuration through fiber optics. The collected Raman signals were filtered by an edge filter (RazorEdge LP02-488RE-25) and sent through fiber optics to a spectrometer and equipped with a thermoelectrically cooled CCD (Andor DV401-BV). An infinity-corrected objective lens with a working distance of 3.9 mm (Nikon 20X, NA=0.4) was used to focus excitation laser and to collect Raman scattering. Within the distance, a micro-sized mirror mounted on a mechanical arm was inserted close to sample surface at an angle of 25º under the objective, which reflects the incident laser to 50º relative to the sample surface normal. The mirror was made from a typical used chip of AFM tips with a front-side coating of aluminum, where the tips and cantilevers on the chip were manually removed prior the coating processes. The trapezoidal cross-section allows the mirror to be placed very close to sample surface (less than 30 μm). Therefore, reflected laser focused spot would be close enough to be

observed within the same field of view under the microscope. The polarization of the laser can be arranged in any direction. For all the TERS experiments in this paper, the excitation laser was kept in the p-polarized direction relative to the AFM tip axis for a better enhancement coupling. A silver nanowire mounted on an AFM tip was held by another mechanical arm and brought to the reflected laser focus. While the tip was in contact with a sample, the AFM feedback laser was focused and collected by the same objective to maintain a constant force between the tip and the sample. The wavelength of the feedback laser was chosen in the near-infrared region to avoid any influence on the Raman excitation laser in the visible range (488 nm). The focused position under the objective was arranged at the place away from the focus of the Raman excitation laser by nearly 100 μm. As such, both the lasers can be well separated, which allows the tip and the mirror to be arranged properly within the separation. During AFM and TERS measurements, only the sample was being scanned, while the rest of the components remained at the same relative positions.

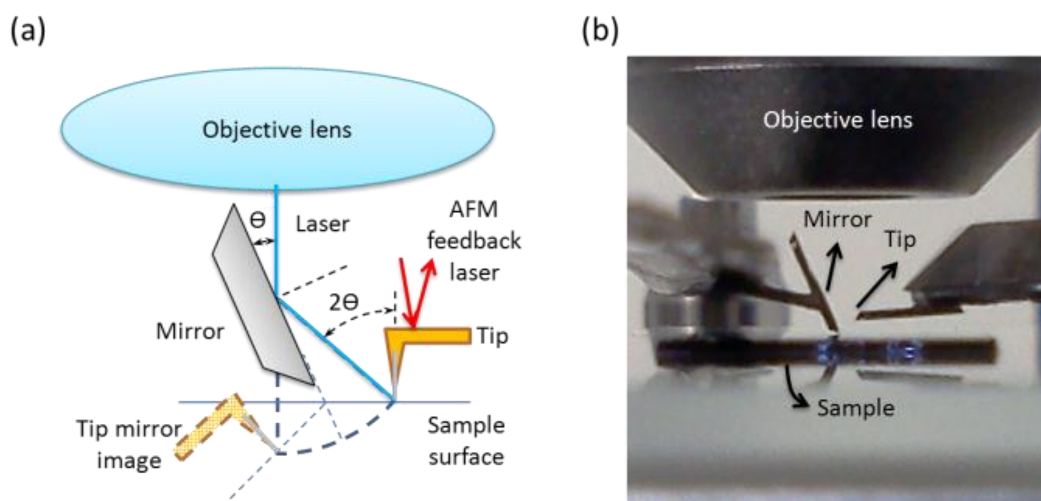

Figure 28. (a) Instrumental setup under objective lens, and (b) optical picture of the setup.

Alignment processes.

The alignment processes involved adjusting suitable relative positions of the four major components, including the laser focus, the mirror, the tip, and the sample surface. The aligned TERS system is shown in Figure 29a under white light illumination and in Figure 29b under laser illumination. Considering the mirror image of the tip and the sample surface, the arrangement is equivalent to the side-illumination configuration. The sample was first placed on the AFM scanning stage and the surface was used as a reference plane. Since all the components were visible under the microscope, the mirror was then arranged in a place on the laser focusing path with a vertical distance of 20~30 µm to the sample surface. Meanwhile, the reflected laser focus position was recorded by the microscope. The sample surface was temporally lowered below the reference plane

to enable the tip to be moved to the reflected laser focus position on the reference plane. Afterward, the tip and the sample were brought into contact based on the AFM force feedback.

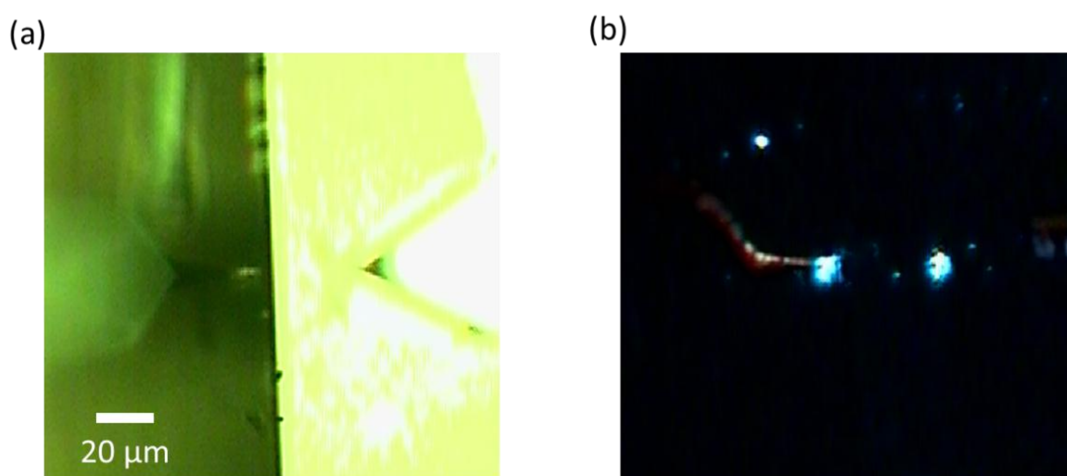

Figure 29. Optical images of a tip, a micro-sized mirror, and a sample under (a) white light illumination, and (b) laser illumination.

TERS tip preparation

A silver nanowire suspension solution was first filtered on an alumina membrane (Whatman Anodisc 25) and followed by washing with plenty of ethanol through the membrane. The membrane downstream was evacuated to expedite the filtering processes. The membrane with silver nanowires was cut into two pieces by bending to expose the nanowires on the cracking edges. An AFM tip controlled by a mechanical arm was

dipped into a small droplet of viscous adhesive, and pulled out of the adhesive immediately. The tip coated with adhesive was brought into contact with a part of a chosen silver nanowire on the edge of the membrane. When the nanowire was stuck on the tip, the tip with the nanowire was pulled away from the membrane. Before the adhesive was fully cured, the protruding length and the tilting angle of the nanowire were adjusted. For a typical condition, the nanowire were kept parallel to the tip with a protruding length of 1~2 μm. The whole processes were operated under an optical microscope with a resolving power of ~0.5 μm. Avoiding operation under scanning electron microscope (SEM) may prevent nanowires from carbon contamination induced by electron beam.[147] Several types of adhesive including PDMS, five-min epoxy, and Norman optical adhesive were successfully used to mount nanowires on AFM tips. The adhesive may need to be partially cured if it's not viscous enough.

Synthesis of silver nanowire suspension

The synthetic procedures for the silver nanowire suspension were modified from the previous literature.[148] In brief, 5 ml of ethylene glycol with low Fe and Cl content (J.T. Baker) was first heated at 152 ºC for an hour, 10 μL of 50 mM $CuCl_2 \cdot 2H_2O$ (Aldrich) ethylene glycol solution was added and heated for additional 15 min. 1.5 mL of 147 mM polyvinylpyrrolidone (Aldrich, average MW = 5000) ethylene glycol solution and 1.5 mL of $AgNO_3$ ethylene glycol solution were then added. The concentration of polyvinylpyrrolidone was calculated according to its repeating unit. The

whole solution was stirred and heated at 152 ºC constantly for 1~2 hours. The resulting opaque solution was cooled and stored at room temperature for the later use.

5.3 Results and discussion

Preparation and characterization of silver nanowire tip

Nanowires were synthesized via a wet chemistry method due to its reproducibility, apex controllability, and convenience. Figure 30a shows the UV-Vis spectrum of silver nanowires in aqueous solution. Silver nanowires were transferred from original ethylene glycol solution to acetone and then to aqueous solution through centrifuging-sonication cycles. A broad peak of the combination between transverse mode of nanowires and surface plasmon of nanoparticles was observed at nearly 400 nm, indicating that a small portion of nanoparticles form in the early stage did not fully develop into nanowire structures. A SEM picture of nanowires on an alumina membrane shown in Figure 30b further confirmed that the majority of the silver precursor formed nanowires. All nanowires had pentagon cross-sections with uniform diameters along their body, cone shapes near their terminals, and nearly spherical apexes.[148] The nanowire lengths ranged typically from 5 to 20 µm. Depositing nanowires on the alumina membrane provided a useful method to remove the synthetic by-products and to arrange nanowires especially on the cracking edge for TERS tip preparation. These nanowires on the edge may be easily picked up by an AFM tip pre-coated with adhesive, because the tip can form desired contact with the exposed nanowire without touching the membrane.

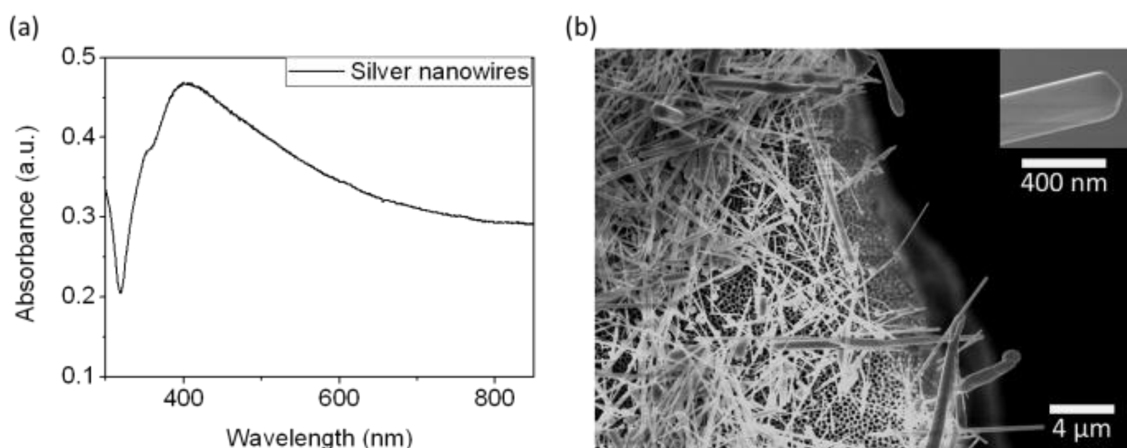

Figure 30. (a) UV-Vis spectrum of silver nanowires suspended in aqueous solution, and (b) silver nanowires deposited on a filter.

The key parameters to the successful attachment of a silver nanowire onto an AFM tip includes: 1) adhesion between the nanowire and the tip, 2) length of the protruding part of the nanowire relative to the tip, and 3) orientation relative to a sample surface normal. The attaching processes on a new AFM tip or a used tip are shown in Figure 31. We found that the apex radius of an AFM tip had almost no effect on the nanowire attaching processes. In general, nanowires chosen in the attachment have lengths in the range of 5~10 μm due to a typical AFM tip height of ~15 μm. As such, the contact area was enough to provide a proper adhesion force for the nanowire fixation. Once a desired nanowire was transferred onto an AFM tip, the protruding part of the nanowire was shortened to a length of 1~2 μm by pushing the nanowire backward. This adjustment had to be done before adhesive was cured. A shortened protruding length provided better mechanical stability, because a torque on the nanowire created from a

friction force was reduced when it was scanned on a sample. In addition, the threshold of the normal force to buckle the nanowire was also increased due to its shorter length. For Raman spectrum background, the protruding nanowire can prevent Raman scattering of AFM tip material or adhesive from being excited and collected, especially useful when a sample has similar Raman features to the tip material or the adhesive. In terms of the orientation of the nanowire, the nanowire angle was kept as parallel as possible relative to the sample surface normal. It should be taken into account during the attaching processes that most AFM design contains a tilting angle of 10º~15º for AFM tips. As such, the sharper end of the nanowire was able to contact the sample surface, and a torque on the nanowire created from a normal force was minimized when it was in contact with the sample. Most importantly, control over these parameters in the attaching processes allows optimization for TERS integration of different AFM and optical systems.

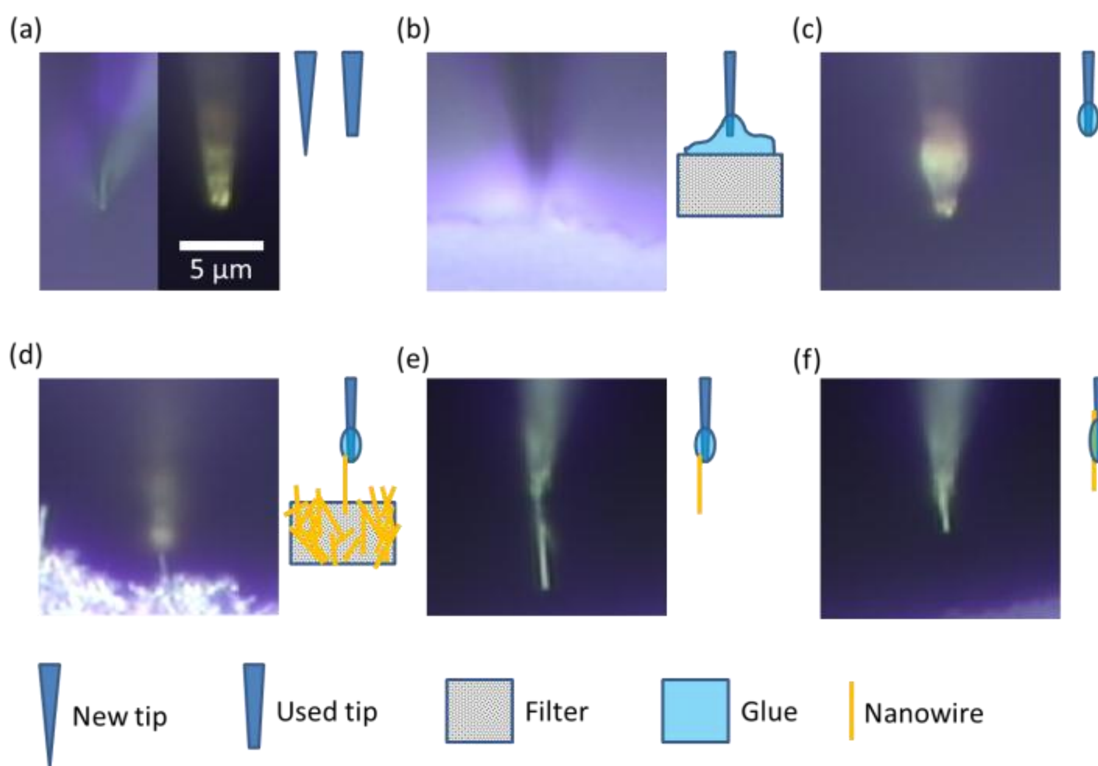

Figure 31. Optical microscopic pictures of nanowire attachment: (a) a sharp and a blunt AFM tip, (b) a tip dipped into a thin layer of glue, (c) a tip coated with a small amount of glue, (d) a silver nanowire in contact with a tip pre-coated with glue, (e) a silver nanowire transferred on a tip, and (f) a silver nanowire fixed on a tip after adjustment. The inset next to the pictures indicates the attaching processes in the pictures and the symbols are explained in the bottom.

AFM scanning by the nanowire apex on a test grating standard for AFM tip calibration (NT-MDT TGT01) was performed to confirm the mechanical strength of the nanowire attachment. The grating contains an array of sharp spikes with a curvature radius less than 10 nm and a cone angle about 50º. AFM Scanning around the spike cone can provide force interaction tests in all the lateral directions. The scanning on one of these spikes is shown in Figure 32a and the cross-sectional profile across the highest

point in Figure 32a was shown in Figure 32b. The smooth scanning contours indicated that the nanowire and its fixation were stable enough when these normal and lateral loads were applied. Meanwhile, the radius of a nanowire apex near a nanowire-sample junction was able to be estimated by the reverse imaging reconstruction. The image (Figure 32a) had a cone shape with a round top due to the nanowire-spike convolution. The region with a height difference less than 15 nm to the highest point was treated as a reversed image of the nanowire apex, considering the much sharper spike had little contribution to the convolution in the region. The resulting radius was estimated to be 127 nm, and the fitting curve is shown in Figure 32b.

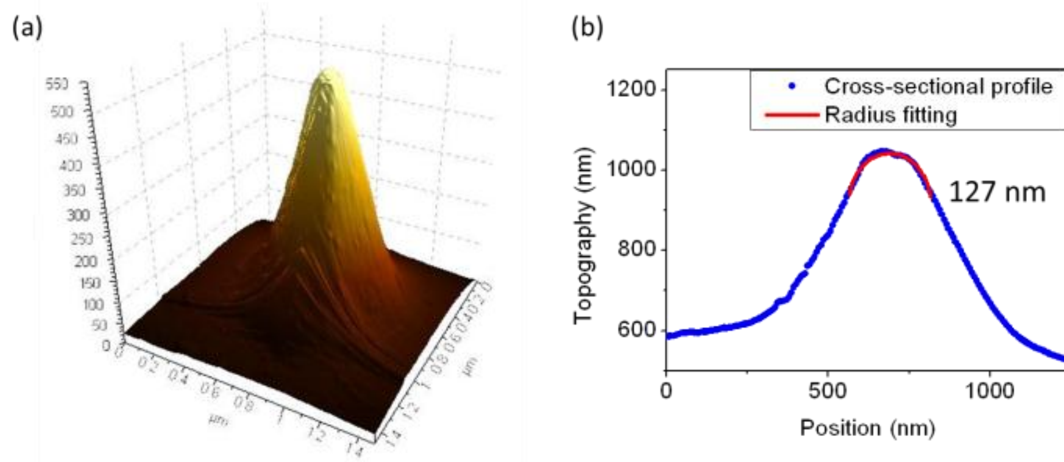

Figure 32. (a) AFM scanning on a calibration standard by a nanowire, and (b) its cross-sectional profile across the highest point.

The fluidity and the viscosity of adhesive play crucial roles in the attaching processes. When the fluidity is too high and the viscosity is too low, it will be difficult to pick up a nanowire, and the nanowire apex will be contaminated by the glue. The orientation and the protruding length of a nanowire on AFM will not be able to control, even if the nanowire is transferred onto a tip. Most importantly, the apex of the nanowire responsible for localized Raman enhancement may be contaminated by adhesive. In our experience, semi-cured adhesive mostly gave a better performance. A nanowire attached on a new AFM tip is shown in Figure 33a. The nanowire apex observed in the SEM picture agreed well with the previous result of the radius calibration. The nanowire was placed along the side wall on the tips, in which the contact area was maximized to ensure their rigid attachment. No adhesive residue was observed on the protruding part of the nanowire. Therefore, the attaching processes didn't introduce any influence to TERS background. In fact, no noticeable Raman scattering related to adhesive was observed in any TERS measurement. As mentioned above, the protruding nanowire can not only prevent Raman scattering of AFM tip material or adhesive from being excited and collected, but also protect nanowire apex against adhesive contamination due to a 1~2 μm separation from the tip. We found that the protruding part of a nanowire attached on an AFM tip can be broken by applying an extremely large torque, and another nanowire was able to be attached on this broken tip. Figure 33b shows a protruding nanowire on a recycled tip with several broken nanowires on the tip cone. The breaking-reattaching processes were repeated several times, and thus several broken nanowires were observed in the picture. As mentioned earlier, the apex of an AFM tip does not affect the attaching

processes. The tip in this case had a blunt apex with a radius of 50 nm. As the SEM picture shows, all the nanowires were tilted a little off the central axis of the AFM tip. This was done on purposes to observe the nanowires and the tip apex under SEM at the same time without covering each other. However, a nanowire generally used for TERS measurement was placed along the central axis of an AFM tip, and its orientation was kept as parallel as possible relative to the sample surface normal.

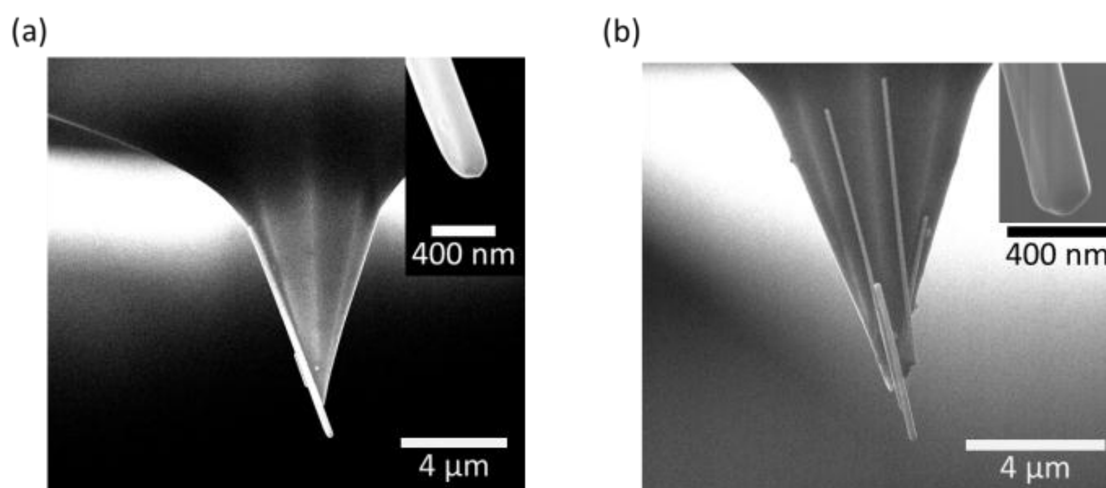

Figure 33. SEM pictures of a nanowire fixed on (a) a new tip, and (b) an old tip recycled several times. The inset shows the zoom-in picture near the nanowire apex.

Tip enhancement and TERS scanning

The Raman enhancement due to the coupling between a nanowire apex and a sample was demonstrated. Rhodamine 6g (R6g) was used for the tip enhancement

studies, because its properties are well-understood, and extensively investigated in TERS and SERS literature. A typical Raman spectrum of R6g absorbed on silver thin film on glass is shown in Figure 34a. The Raman signal was collected over 100 sec with a spectral resolution of 2 cm^{-1} under a total excitation power of 122. The silver thin film with a thickness of 50 nm was deposited on a glass slide through thermal evaporation, and A 25 μM R6g ethanol solution was spin-coated on the silver thin film. Even under a weak power of laser excitation, R6g exhibited a serious of distinct Raman scattering peaks, because the silver film as a SERS substrate provided a moderate enhancement already. The R6g fluorescence under laser excitation was substantially suppressed due to the quenching from the silver film. From the strong quenching, the R6g layer absorbed on the silver film was estimated to be less than 2 nm. However, it is difficult to precisely measure the thickness even under AFM measurement due to the nature roughness of the silver film. We will discuss the thickness further in the next section. The tip enhancement is shown in Figure 34b. Comparing the spectra when the nanowire was in contact to the R6g sample on the silver film (red line) with the spectra without the contact (blue line), it is obvious that the Raman intensity was increased by 2~3 folds. Due to the need of a short collection time (1~10 sec), the spectral resolution among these spectra was reduced to 20 cm^{-1} to achieve reasonable signal-to-noise ratios. To ensure that the tips did not influence the collection of normal Raman spectra, the tip was retracted for at least 100 μm away from the sample surface, when the Raman spectra without the nanowire enhancement were collected. During the removal of the tip, the

AFM force feedback was turned off to maintain the same alignment among the sample, the mirror, and the laser focus.

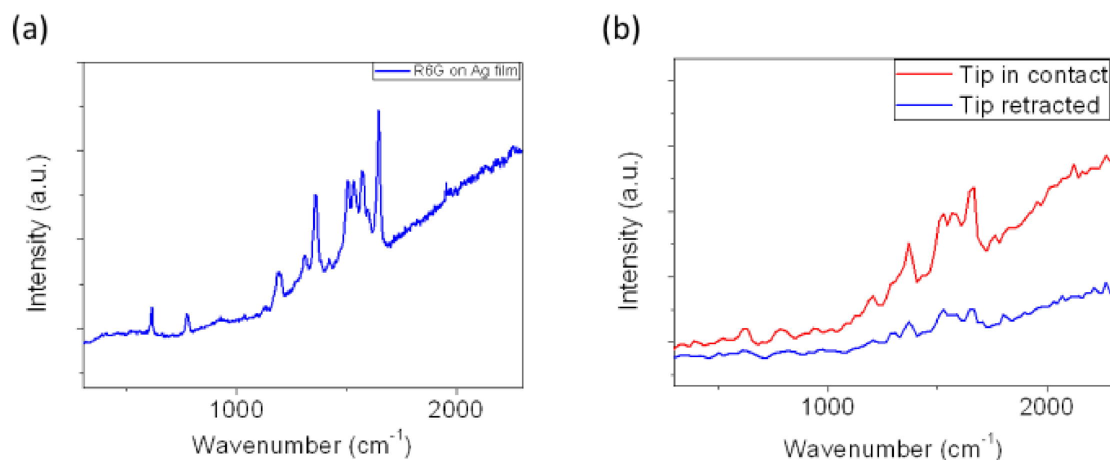

Figure 34. Raman spectra of R6g on silver film (a) at high spectral resolution, and (b) at a reduced resolution with and without tip enhancement.

To correlate the Raman enhancement in the nanowire-silver film junction over a regular Raman reference, the spectra of R6g on silver film and R6g on glass (as shown in Figure 35) were compared. A 25 μM R6g ethanol solution was spin-coated on a silver film on a glass slide containing slits with a width about 100 μm. The spectrum of R6g on glass was collected near the center of a slit, where glass was exposed. The collection time between these two spectra was not able to be kept the same, because the intensity difference was beyond the dynamic range of our spectrometer. These spectra were

mathematically normalized according to their collection time. The intensity on silver film was much stronger than that on glass by 100~200 folds. The R6g film thickness was assumed to be the same or similar on both area, because the wettability of ethanol is good at both surface of the silver film and the glass. The enhancement factor (E. F.) was estimated based on the integrated intensity of the major scattering peaks in the range between 1000 and 1800 cm^{-1} among the enhanced Raman spectra and the non-enhanced spectra. The calculation is shown below:

$$\mathrm{E.\,F.} = \frac{I_{Nanowire} - I_{Ag}}{I_{Ag}} \times \frac{A_{Laser}}{A_{Nanowire}} \times \frac{I_{Ag'}}{I_{Glass}},$$

where $I_{Nanowire}$ is the Raman intensity (Figure 34b red line) from the laser focused region with the nanowire in contact, I_{Ag} is the intensity (Figure 34b blue line) without the contact, $A_{Nanowire}$ is the enhancement area corresponding to the nanowire-silver film coupling, and A_{Laser} is the area of the focused laser spot, $I_{Ag'}$ is the Raman intensity (Figure 35 red line) from the laser focused region on the silver film, and I_{glass} is the intensity (Figure 35 blue line) from the laser focused region on the glass. $A_{Nanowire}$ was estimated based on the apex radius of the nanowire obtained from the reverse imaging reconstruction and the SEM picture mentioned above. To determine A_{Laser}, a photoresist thin film was prepared on a glass slide exposed to the focused laser spot. The pattern related to the focused profile was developed through a standard photolithography processes. The AFM scanning over the focused spot shown in Figure 36 had an ellipse shape with a major radius of 3.9 μm and a minor radius of 1.9 μm. The asymmetric shape was caused by the tilted incident angle. Thus, A_{Laser} was estimated to be 23.5 μm^2. The enhancement factor of 1.6×10^5 was obtained in the calculation. The calculation of

the tip enhancement was based on the assumptions: first, the thickness of the R6g thin film is uniform; second, $A_{Nanowire}$ is much smaller than A_{Laser}. According to the AFM and SEM analyses, the assumptions here are generally valid.

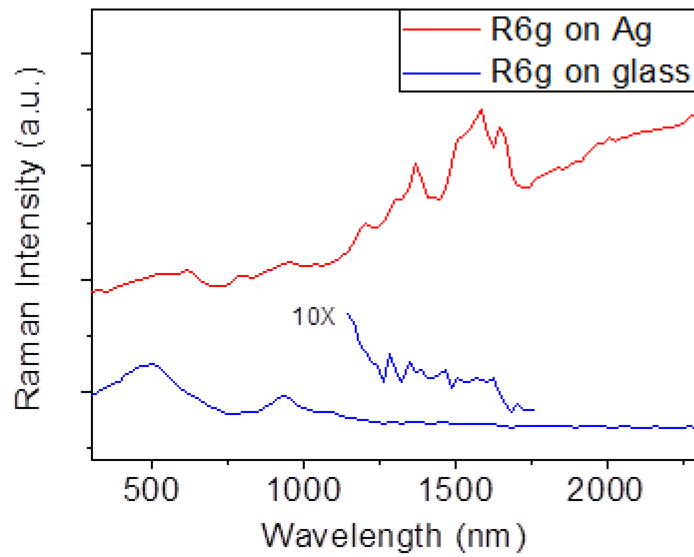

Figure 35. Raman spectra of R6g on silver film and on glass.

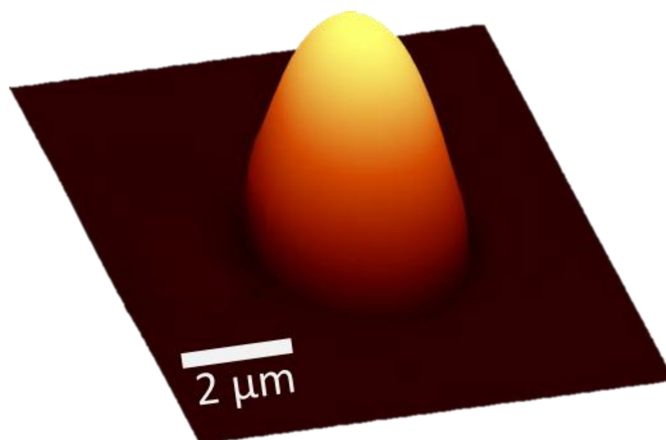

Figure 36. Beam profile of a focused laser.

A sample containing several parallel stripes was prepared to demonstrate the scanning ability of our TERS system. The same as the sample used for the calculation of the enhancement factor, R6g was spin-coated on a silver thin film, thermally evaporated on a glass slide. The surface morphology was characterized by the AFM scanning and shown in Figure 37a for the topography and in Figure 37b for the lateral force image. The silver film had a homogeneous and complete coverage with a fine granular structure. Except for topographic artifact due to grain boundaries, the lateral force image also show exhibited a uniform distribution, indicating the silver thin film was coated with R6g entirely. Local oxidation nanolithography was performed with a contact mode AFM with additional electrical bias applied between tip and sample. The electrochemical reaction confined in a water meniscus forming near a tip-sample junction locally decomposed some R6g molecules and created a modified spot. Four parallel stripes were drawn by assembling these spots. The linear feature was visualized by the AFM scanning and

shown in Figure 37c for the topography and in Figure 37d for the lateral force image. Each stripe had a width of 1.2 μm, and two adjacent stripes were spaced by a gap of 800 nm. Compared with the background region, the region where the local oxidation was performed had a high difference of 0.4 nm in average, which is less than the noise level of 1 nm in our AFM. In addition, the root-mean-square roughness of the oxidation region was increased slightly from 4.1 nm to 4.9 nm based on a sampling area of 48 μm^2. On the contrary, the lateral force image showed the significant contrast, indicating that the R6g coating was altered considerably. As such, it is highly possible that the thickness of the R6g coating was thinner than 1~2 nm. Therefore, the decomposition of R6g did not cause a noticeable difference in height or roughness. Moreover, the silver film underneath the R6g coating might be oxidized slightly, and thus the oxidation might partially compensate the height difference.

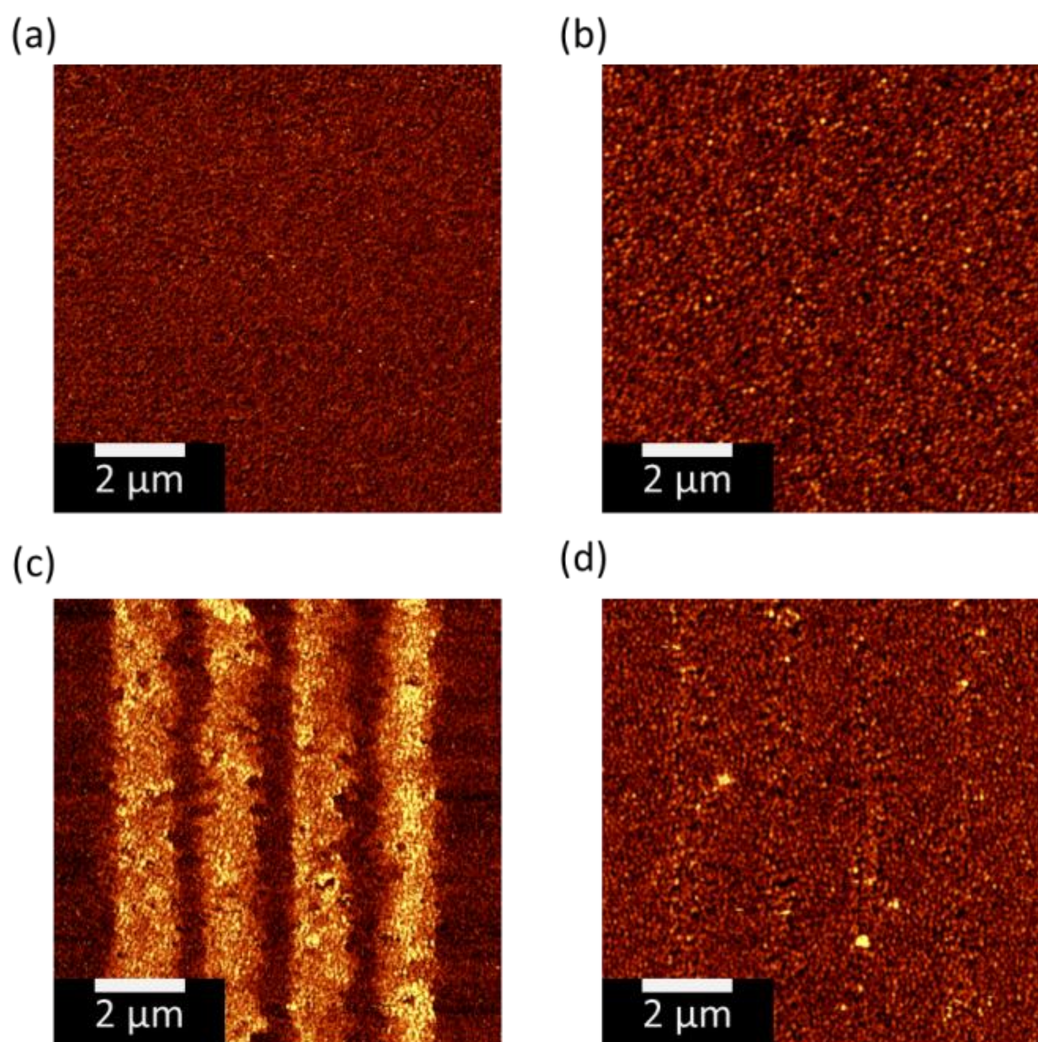

Figure 37. (a) Lateral force image of R6g on silver film, (b) topographic image of R6g on silver film, (c) lateral force image of R6g on silver film after local oxidation nanolithography, and (d) topographic image of R6g on silver film after local oxidation nanolithography.

The TERS and Raman scanning were performed in the vertical direction relative to the nanolithographic stripes. The regular Raman (Figure 38a) scanning without a nanowire in contact with the stripe sample was performed under the same condition as

the following TERS scanning with a nanowire in contact (Figure 38b). The integrated intensity of the major scattering peaks in the range between 1000 and 1800 cm^{-1} was plotted as a function of the nanowire position. For the regular Raman scanning, the Raman signals decreased near the nanolithographic stripes. A decline in number of the R6g molecules was expected, and the corresponding intensity of Raman scattering would be reduced as well. The affected region and the unaffected gap were designed to have similar dimension (2 μm) to the laser focus. The regular Raman signals were collected from both the regions at every sampling position near the stripes. As such, the nanolithographic features of these stripes and gaps were not able to be resolved individually. For the TERS scanning, the enhanced region was confined near the apex of the nanowire, which was much smaller than the nanolithographic patterns. Therefore, the TERS scanning showed the same features as the AFM lateral force image.

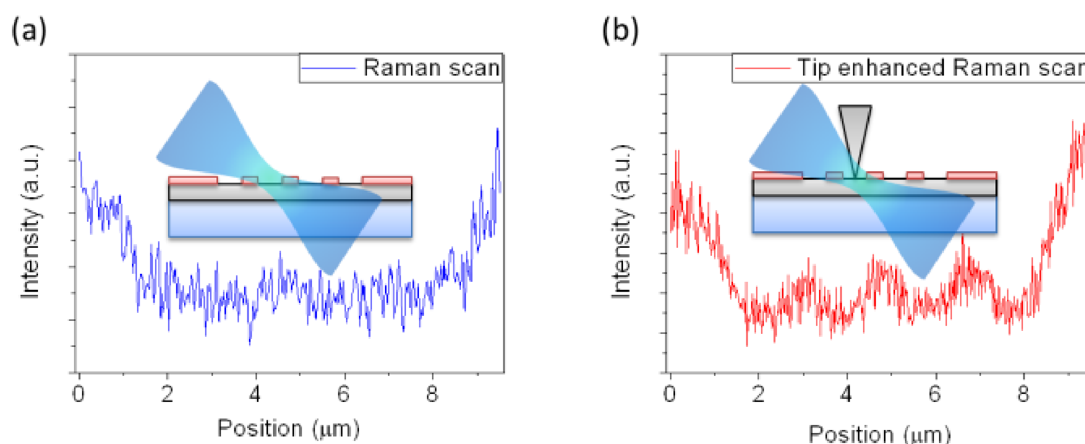

Figure 38. (a) Confocal Raman line-scanning across the nanolithographic region, and (b) tip-enhanced Raman line-scanning across the same region.

5.4 Conclusion

The introduction of a micro-sized mirror and the use of a nanowire in the proposed TERS setup successfully overcame the issues in terms of sample limitation, instrumental complexity, and tip preparation. The sensitivity and the resolution of in this system were demonstrated by the use of R6g molecules and local oxidation nanolithography. This combination of the setup and the tip preparation may also be applied in the other TERS geometry, separately. The enhancement factor may be further improved by the optimization in nanowire geometry and wavelength matching between laser excitation and localized surface plasmon of nanowire.

CHAPTER VI

CONCLUSIONS AND OUTLOOK

In this work, a patterning technique based on scanning probe lithography was demonstrated to guide molecular assembly and to realize further pattern transferring onto metallic layers and graphene layers. A photo-response was observed on graphene-based transistors with porphyrin molecules self-assembled on graphene channels. The phenomenon of molecular decomposition during charge transport has been proven practical via a non-destructive optical TERS method. The TERS system was improved further by introducing a micro-sized mirror and a nanowire. The new TERS setup successfully overcame long-existing issues of sample limitation, instrumental complexity, and tip preparation.

The patterning technique not only offers a simple, flexible, and low-cost method to create complex patterns for graphene FETs without using expensive e-beam or photolithographic equipment, but more importantly, it provides a platform for the systematic study of the molecular assembly built upon the FETs. The reliable contact between each layer ensured device stability even under a large current density. The minimum line width (~100 nm) might be improved further by increasing etching selectivity on ODT SAMs, because the width was mainly limited by the wet etching steps. This can be achieved by healing defects or disorder in ODT SAMs.[149] In addition, the electrical properties of the single-layer graphene FET and porphyrin-graphene composite FET made by this approach were studied. As such, the technique may provide

a versatile platform for further investigation of devices with graphene-molecular contacts and for building up higher order structures.

To clarify the influence of the surrounding chemical environment on the graphene channel, two directions will be explored: 1) substrate effects and 2) absorbate effects. The main impacts introduced from substrates include carrier doping, charged surface state or impurities, and surface phonons. Recently, the effects from several supporting materials have been discussed, such as boron nitride,[92] and free-standing graphene.[91] However, in general, these substrates are impractical or very challenging for future large-scale applications. Recently, surface modification has been proposed to functionalize substrates with desired properties by using octadecyltrichlorosilane[150] and hexamethyldisilazane.[151] Both of these reports showed hysteresis behavior of graphene in the gate field could be suppressed, even under ambient conditions. To understand fully each of the impacts mentioned above, the surface of the substrate used in the dissertation, SiO_2/Si, will be systematically modified with various silane SAMs and mixed SAMs. Here, a series of silane molecules will be examined, including alkylsilane, aminosilanes, partially oxidized alkylsilane, and phenyl-terminated organosilane, to study Coulomb and pi-pi interaction. The interaction strength will be controlled by their density in the mixed SAMs, which can be tuned during the assembling formation of the corresponding molecules.

Effects related to absorbate will be the second direction of exploration. The absorbate may absorb on the graphene surface through intermolecular forces and covalent bonding. The former interactions include van der Waals, dipole-dipole forces,

and so on, which are similar to the effects contributed by the substrates. In contrast, covalent bonding creates influences that are more complex. A short-range potential can be introduced, which alters the energy band structure for control of energy dispersion and band gap engineering. For example, the absorption of atomic hydrogen[152] and nitrophenyl radicals[153] on graphene has shown evidence of band gap opening, which was exhibited by current-voltage characteristics and angle-resolved photoemission spectroscopy. The chemical functionalization provides a simple but CMOS-compatible method to form relatively stable absorbates due to the stronger interaction compared with intermolecular forces. Through oxygen plasma treatment, oxygen species, including hydroxyl and epoxide functional groups, will be introduced into the graphene structure to examine the influence between grafting density and electronic properties. The distribution of the oxygen species will also be considered as an important factor, which can be nucleated through using biased AFM lithography. These results will be useful in understanding their interwoven relationships. In addition, the oxygen functional groups can be seen as chemical linkers to attach further active components. A serious of ligands, ranging from electron donating to withdrawing, will be inserted onto the linkers, such as amino, phenyl, arkyl, and nitro groups. Their weakening or strengthening ability will be evaluated by their impact on the charge transporting behaviors of graphene by current-voltage characterizations.

The local chemical sensing was demonstrated by a combined system of side-illuminated TERS and conductive-probe AFM. The modification made from AFM-based nanolithography can be detected simultaneously on the platform. The local

decomposition was observed under a harsh condition. The silver-coated tip can enhance Raman signals in the range from 10^3 to 10^5, which provides reasonable sensitivity and spatial resolution. For the newly proposed TERS setup, the use of a silver nanowire provides various advantages over the typical metal evaporation methods for TERS tip preparation, such as a consistent enhancing ability and the tuneability of resonance frequency. The surface plasmon polaritons of these crystalline nanowires have consistent resonance wavelength relative to their dimensions, which is important for matching the excitation wavelength to improve the Raman enhancement.

To understand further the structure-changing processes of active chemical components during charge transport, the key is the ability to monitor the species in real time. This goal will be explored with the two aims: 1) optimization of the ultimate sensitivity, and 2) extension into the time resolution. The sensitivity will be improved by increasing the near-field enhancing power and decreasing the far-field background noise. Du *et al*.[146] concluded that the Raman enhancing power of a silver nanowire is related to the tip geometry, and the wavelength and the polarization of the incident laser. Therefore, the Raman enhancement can be optimized by adjusting the physical parameters of nanowires regarding end shape, diameter, and length during synthetic processes. Further improvement will be focused on wavelength matching between localized surface plasmons and the excitation laser to provide higher enhancement. Another factor that limits the sensitivity is the background noise in the far field, which is generated by the direction laser excitation. The spectral background not only hinders the detection of low-level Raman signals, but also restricts overall TERS spatial resolution due to laser

focusing limitations in the far field. To suppress intrinsic far-field Raman background, the positions of the laser excitation and the near-field enhancing have to be separated, and the laser excitation energy has to be transferred between the positions. Fang *et al.*[154] revealed the possibility of using plasmonic propagation as a remote excitation source of SERS along a single silver nanowire. The waveguiding properties of nanowires[155] allows excitation of surface plasmon polaritons on one terminal and plasmonic propagation to the other. In principle, these crystalline silver nanowires with an optimized dimension can transfer the energy with minimal ohmic losses and focus it at the terminal. As such, the far-field background may be reduced or even removed due to the indirect remote excitation.[37] This improvement and the related modification in optics will be implemented in the TERS system to extend further the sensitivity and resolution. However, some issues related to tip contamination and deformation limit the overall sensitivity and resolution. Similar to other SPM techniques, the contamination on the tip may generate suspicious artifacts. The non-contact scanning mode may mitigate the situation due to the separation between the tip and a target sample, but the trade-off is the degradation in the TERS sensitivity and resolution. Compared with typical SPM tip materials, such as silicon, silver is a relatively soft substance. Therefore, extremely thin silver nanowire is not suitable to be used in the TERS system here. In addition, silver tends to oxidize in ambient conditions, which decreases the Raman enhancement. Although Barrios *et al.*[139] suggested that a thin Al_2O_3 coating on silver may improve the mechanical strength and the chemical stability, it still remains in challenge to fully overcome these issues.

To depict a full picture of how an active component in a molecular device transforms from one state into another during charge transport, the target component will be tracked step-by-step using variable short electric pulses. The pulse duration will be systematically increased and the corresponding effects will be observed by the optimized TERS sensing system mentioned above. This system will require a sophisticated synchronizer to control the timing between each elemental instrument, including the pulse generator, AFM, and spectrometer. A typical pulse generator can vary the duration in the range from seconds down to picoseconds. Therefore, a similar time resolution to track a reaction path of active molecules may be achieved. All the improvements will lead to a deeper knowledge and greater insight into molecular behaviors and roles during charge transport, which will guide device design and fabrication, to enable newer functionality and better performance.

REFERENCES

(1) Thompson, S. E.; Parthasarathy, S. *Mater Today* **2006**, *9*, 20.

(2) Jurvetson, S. *Nanotechnology: Societal Implications II - Individual Perspectives* **2007**, 43.

(3) Banine, V. Y.; Koshelev, K. N.; Swinkels, G. H. P. M. *J Phys D Appl Phys* **2011**, *44*.

(4) Heath, J. R.; Ratner, M. A. *Phys Today* **2003**, *56*, 43.

(5) Kauffman, D. R.; Star, A. *Angew Chem Int Edit* **2008**, *47*, 6550.

(6) Weitz, R. T.; Zschieschang, U.; Forment-Aliaga, A.; Kalblein, D.; Burghard, M.; Kern, K.; Klauk, H. *Nano Lett* **2009**, *9*, 1335.

(7) Chen, Y. S.; Hong, M. Y.; Huang, G. S. *Nat Nanotechnol* **2012**, *7*, 197.

(8) Green, J. E.; Choi, J. W.; Boukai, A.; Bunimovich, Y.; Johnston-Halperin, E.; DeIonno, E.; Luo, Y.; Sheriff, B. A.; Xu, K.; Shin, Y. S.; Tseng, H. R.; Stoddart, J. F.; Heath, J. R. *Nature* **2007**, *445*, 414.

(9) Wong, H.; Filip, V.; Wong, C. K.; Chung, P. S. *Microelectron Reliab* **2007**, *47*, 1.

(10) Palmer, L. C.; Stupp, S. I. *Accounts Chem Res* **2008**, *41*, 1674.

(11) Sortino, S. *Chem Soc Rev* **2010**, *39*, 2903.

(12) Hutin, M.; Long, D. L.; Cronin, L. *Isr J Chem* **2011**, *51*, 205.

(13) Raynor, J. E.; Capadona, J. R.; Collard, D. M.; Petrie, T. A.; Garcia, A. J. *Biointerphases* **2009**, *4*, Fa3.

(14) Shankar, S. P.; Chen, I. I.; Keselowsky, B. G.; Garcia, A. J.; Babensee, J. E. *J Biomed Mater Res A* **2010**, *92A*, 1329.

(15) Gooding, J. J.; Mearns, F.; Yang, W. R.; Liu, J. Q. *Electroanal* **2003**, *15*, 81.

(16) Mandler, D.; Turyan, I. *Electroanal* **1996**, *8*, 207.

(17) Kobayashi, S.; Nishikawa, T.; Takenobu, T.; Mori, S.; Shimoda, T.; Mitani, T.; Shimotani, H.; Yoshimoto, N.; Ogawa, S.; Iwasa, Y. *Nat Mater* **2004**, *3*, 317.

(18) DiBenedetto, S. A.; Facchetti, A.; Ratner, M. A.; Marks, T. J. *Adv Mater* **2009**, *21*, 1407.

(19) Srinivasan, M. P.; Ratto, T. V.; Stroeve, P.; Longo, M. L. *Langmuir* **2001**, *17*, 7951.

(20) Jiang, X. Y.; Ferrigno, R.; Mrksich, M.; Whitesides, G. M. *J Am Chem Soc* **2003**, *125*, 2366.

(21) Wang, G.; Kim, Y.; Choe, M.; Kim, T. W.; Lee, T. *Adv Mater* **2011**, *23*, 755.

(22) Chen, F.; He, J.; Nuckolls, C.; Roberts, T.; Klare, J. E.; Lindsay, S. *Nano Lett* **2005**, *5*, 503.

(23) Nacci, C.; Lagoute, J.; Liu, X.; Folsch, S. *Phys Rev B* **2008**, *77*.

(24) Lauhon, L. J.; Ho, W. *Phys Rev Lett* **2000**, *84*, 1527.

(25) Huang, Z. F.; Xu, B. Q.; Chen, Y. C.; Di Ventra, M.; Tao, N. J. *Nano Lett* **2006**, *6*, 1240.

(26) Xie, X. N.; Chung, H. J.; Sow, C. H.; Wee, A. T. S. *Mat Sci Eng R* **2006**, *54*, 1.

(27) Katano, S.; Kim, Y.; Hori, M.; Trenary, M.; Kawai, M. *Science* **2007**, *316*, 1883.

(28) Kudelski, A. *Vib Spectrosc* **2005**, *39*, 200.

(29) Komeda, T. *Prog Surf Sci* **2005**, *78*, 41.

(30) Bailo, E.; Deckert, V. *Angew Chem Int Edit* **2008**, *47*, 1658.

(31) Domke, K. F.; Zhang, D.; Pettinger, B. *J Am Chem Soc* **2006**, *128*, 14721.

(32) Zhang, W. H.; Yeo, B. S.; Schmid, T.; Zenobi, R. *J Phys Chem C* **2007**, *111*, 1733.

(33) Georgi, C.; Hartschuh, A. *Appl Phys Lett* **2010**, *97*.

(34) Marquestaut, N.; Talaga, D.; Servant, L.; Yang, P.; Pauzauskie, P.; Lagugne-Labarthet, F. *Journal of Raman Spectroscopy* **2009**, *40*, 1441.

(35) Stadler, J.; Schmid, T.; Zenobi, R. *Nano Lett* **2010**, *10*, 4514.

(36) Schmid, T.; Yeo, B. S.; Leong, G.; Stadler, J.; Zenobi, R. *Journal of Raman Spectroscopy* **2009**, *40*, 1392.

(37) Berweger, S.; Atkin, J. M.; Olmon, R. L.; Raschke, M. B. *J Phys Chem Lett* **2012**, *3*, 945.

(38) Yeo, B. S.; Stadler, J.; Schmid, T.; Zenobi, R.; Zhang, W. H. *Chem. Phys. Lett.* **2009**, *472*, 1.

(39) Domke, K. F.; Pettinger, B. *Chemphyschem* **2010**, *11*, 1365.

(40) Picardi, G.; Nguyen, Q.; Schreiber, J.; Ossikovski, R. *Eur Phys J-Appl Phys* **2007**, *40*, 197.

(41) Peica, N.; Rohrig, S.; Rudiger, A.; Brose, K.; Thomsen, C.; Maultzsch, J. *Phys Status Solidi B* **2009**, *246*, 2708.

(42) Diziain, S.; Bijeon, J. L.; Adam, P. M.; de la Chapelle, M. L.; Thomas, B.; Deturche, R.; Royer, P. *Ultramicroscopy* **2007**, *107*, 16.

(43) Kharintsev, S. S.; Hoffmann, G. G.; Dorozhkin, P. S.; de With, G.; Loos, J. *Nanotechnology* **2007**, *18*.

(44) Williams, C.; Roy, D. *J Vac Sci Technol B* **2008**, *26*, 1761.

(45) Saito, Y.; Murakami, T.; Inouye, Y.; Kawata, S. *Chem Lett* **2005**, *34*, 920.

(46) Rasmussen, A.; Deckert, V. *Journal of Raman Spectroscopy* **2006**, *37*, 311.

(47) Gullekson, C.; Lucas, L.; Hewitt, K.; Kreplak, L. *Biophys J* **2011**, *100*, 1837.

(48) Budich, C.; Neugebauer, U.; Popp, J.; Deckert, V. *Journal of Microscopy-Oxford* **2008**, *229*, 533.

(49) Hermann, P.; Hermelink, A.; Lausch, V.; Holland, G.; Moller, L.; Bannert, N.; Naumann, D. *Analyst* **2011**, *136*, 1148.

(50) Bohme, R.; Mkandawire, M.; Krause-Buchholz, U.; Rosch, P.; Rodel, G.; Popp, J.; Deckert, V. *Chem Commun* **2011**, *47*, 11453.

(51) Neugebauer, U.; Rosch, P.; Schmitt, M.; Popp, J.; Julien, C.; Rasmussen, A.; Budich, C.; Deckert, V. *Chemphyschem* **2006**, *7*, 1428.

(52) Chaigneau, M.; Picardi, G.; Ossikovski, R. *Surf Sci* **2010**, *604*, 701.

(53) Tarun, A.; Hayazawa, N.; Motohashi, M.; Kawata, S. *Review of Scientific Instruments* **2008**, *79*.

(54) Domke, K. F.; Pettinger, B. *Journal of Raman Spectroscopy* **2009**, *40*, 1427.

(55) Anderson, N.; Anger, P.; Hartschuh, A.; Novotny, L. *Nano Lett* **2006**, *6*, 744.

(56) Hoffmann, G. G.; de With, G.; Loos, J. *Macromol Symp* **2008**, *265*, 1.

(57) Pettinger, B.; Picardi, G.; Schuster, R.; Ertl, G. *Single Mol* **2002**, *3*, 285.

(58) Steidtner, J.; Pettinger, B. *Phys Rev Lett* **2008**, *100*, 236101.

(59) Yang, Z. L.; Aizpurua, J.; Xu, H. X. *Journal of Raman Spectroscopy* **2009**, *40*, 1343.

(60) Hayazawa, N.; Inouye, Y.; Sekkat, Z.; Kawata, S. *Opt Commun* **2000**, *183*, 333.

(61) Stockle, R. M.; Suh, Y. D.; Deckert, V.; Zenobi, R. *Chem. Phys. Lett.* **2000**, *318*, 131.

(62) Hayazawa, N.; Tarun, A.; Inouye, Y.; Kawata, S. *Journal of Applied Physics* **2002**, *92*, 6983.

(63) Mehtani, D.; Lee, N.; Hartschuh, R. D.; Kisliuk, A.; Foster, M. D.; Sokolov, A. P.; Maguire, J. F. *Journal of Raman Spectroscopy* **2005**, *36*, 1068.

(64) Stanciu, C.; Sackrow, M.; Meixner, A. J. *Journal of Microscopy-Oxford* **2008**, *229*, 247.

(65) Steidtner, J.; Pettinger, B. *Review of Scientific Instruments* **2007**, *78*.

(66) Seo, S.; Lee, J.; Choi, S. Y.; Lee, H. *J Mater Chem* **2012**, *22*, 1868.

(67) Di, C. A.; Wei, D. C.; Yu, G.; Liu, Y. Q.; Guo, Y. L.; Zhu, D. B. *Adv Mater* **2008**, *20*, 3289.

(68) Jo, G.; Choe, M.; Cho, C. Y.; Kim, J. H.; Park, W.; Lee, S.; Hong, W. K.; Kim, T. W.; Park, S. J.; Hong, B. H.; Kahng, Y. H.; Lee, T. *Nanotechnology* **2010**, *21*.

(69) Wang, X.; Zhi, L. J.; Mullen, K. *Nano Lett* **2008**, *8*, 323.

(70) Geim, A. K.; Novoselov, K. S. *Nat Mater* **2007**, *6*, 183.

(71) Knox, K. R.; Locatelli, A.; Yilmaz, M. B.; Cvetko, D.; Mentes, T. O.; Nino, M. A.; Kim, P.; Morgante, A.; Osgood, R. M. *Phys Rev B* **2011**, *84*.

(72) Du, X.; Skachko, I.; Barker, A.; Andrei, E. Y. *Nat Nanotechnol* **2008**, *3*, 491.

(73) Nair, R. R.; Blake, P.; Grigorenko, A. N.; Novoselov, K. S.; Booth, T. J.; Stauber, T.; Peres, N. M. R.; Geim, A. K. *Science* **2008**, *320*, 1308.

(74) Koh, Y. K.; Bae, M. H.; Cahill, D. G.; Pop, E. *Nano Lett* **2010**, *10*, 4363.

(75) Lee, C.; Wei, X. D.; Kysar, J. W.; Hone, J. *Science* **2008**, *321*, 385.

(76) Novoselov, K. S.; Geim, A. K.; Morozov, S. V.; Jiang, D.; Zhang, Y.; Dubonos, S. V.; Grigorieva, I. V.; Firsov, A. A. *Science* **2004**, *306*, 666.

(77) Emtsev, K. V.; Bostwick, A.; Horn, K.; Jobst, J.; Kellogg, G. L.; Ley, L.; McChesney, J. L.; Ohta, T.; Reshanov, S. A.; Rohrl, J.; Rotenberg, E.; Schmid, A. K.; Waldmann, D.; Weber, H. B.; Seyller, T. *Nat Mater* **2009**, *8*, 203.

(78) Lee, S.; Lee, K.; Zhong, Z. H. *Nano Lett* **2010**, *10*, 4702.

(79) Liu, L.; Zhang, L.; Niu, L.; Xu, M.; Mao, X. B.; Yang, Y. L.; Wang, C. *Acs Nano* **2011**, *5*, 6001.

(80) Bae, S.; Kim, H.; Lee, Y.; Xu, X. F.; Park, J. S.; Zheng, Y.; Balakrishnan, J.; Lei, T.; Kim, H. R.; Song, Y. I.; Kim, Y. J.; Kim, K. S.; Ozyilmaz, B.; Ahn, J. H.; Hong, B. H.; Iijima, S. *Nat Nanotechnol* **2010**, *5*, 574.

(81) Cheng, Z. G.; Li, Q.; Li, Z. J.; Zhou, Q. Y.; Fang, Y. *Nano Lett* **2010**, *10*, 1864.

(82) Lin, Y. M.; Dimitrakopoulos, C.; Jenkins, K. A.; Farmer, D. B.; Chiu, H. Y.; Grill, A.; Avouris, P. *Science* **2010**, *327*, 662.

(83) Ishigami, M.; Chen, J. H.; Cullen, W. G.; Fuhrer, M. S.; Williams, E. D. *Nano Lett* **2007**, *7*, 1643.

(84) Wallace, P. R. *Phys Rev* **1947**, *71*, 622.

(85) Dan, Y. P.; Lu, Y.; Kybert, N. J.; Luo, Z. T.; Johnson, A. T. C. *Nano Lett* **2009**, *9*, 1472.

(86) Chen, J. H.; Jang, C.; Adam, S.; Fuhrer, M. S.; Williams, E. D.; Ishigami, M. *Nat Phys* **2008**, *4*, 377.

(87) Lohmann, T.; von Klitzing, K.; Smet, J. H. *Nano Lett* **2009**, *9*, 1973.

(88) Bostwick, A.; McChesney, J. L.; Emtsev, K. V.; Seyller, T.; Horn, K.; Kevan, S. D.; Rotenberg, E. *Phys Rev Lett* **2009**, *103*.

(89) Weitz, R. T.; Allen, M. T.; Feldman, B. E.; Martin, J.; Yacoby, A. *Science* **2010**, *330*, 812.

(90) Park, J.; Jo, S. B.; Yu, Y. J.; Kim, Y.; Yang, W.; Lee, W. H.; Kim, H. H.; Hong, B. H.; Kim, P.; Cho, K.; Kim, K. S. *Adv Mater* **2012**, *24*, 407.

(91) Bolotin, K. I.; Sikes, K. J.; Jiang, Z.; Klima, M.; Fudenberg, G.; Hone, J.; Kim, P.; Stormer, H. L. *Solid State Commun* **2008**, *146*, 351.

(92) Dean, C. R.; Young, A. F.; Meric, I.; Lee, C.; Wang, L.; Sorgenfrei, S.; Watanabe, K.; Taniguchi, T.; Kim, P.; Shepard, K. L.; Hone, J. *Nat Nanotechnol* **2010**, *5*, 722.

(93) Wouters, D.; Schubert, U. S. *Angew Chem Int Edit* **2004**, *43*, 2480.

(94) Teweldebrhan, D.; Balandin, A. A. *Appl Phys Lett* **2009**, *94*.

(95) Xu, S.; Liu, G. Y. *Langmuir* **1997**, *13*, 127.

(96) Liu, M.; Amro, N. A.; Liu, G. Y. *Annu Rev Phys Chem* **2008**, *59*, 367.

(97) Piner, R. D.; Zhu, J.; Xu, F.; Hong, S. H.; Mirkin, C. A. *Science* **1999**, *283*, 661.

(98) Maoz, R.; Frydman, E.; Cohen, S. R.; Sagiv, J. *Adv Mater* **2000**, *12*, 424.

(99) Vettiger, P.; Cross, G.; Despont, M.; Drechsler, U.; Durig, U.; Gotsmann, B.; Haberle, W.; Lantz, M. A.; Rothuizen, H. E.; Stutz, R.; Binnig, G. K. *Ieee T Nanotechnol* **2002**, *1*, 39.

(100) Rosa, L. G.; Liang, J. *Journal of physics. Condensed matter : an Institute of Physics journal* **2009**, *21*, 483001.

(101) Salaita, K.; Wang, Y. H.; Mirkin, C. A. *Nat Nanotechnol* **2007**, *2*, 145.

(102) Xu, S.; Laibinis, P. E.; Liu, G. Y. *J Am Chem Soc* **1998**, *120*, 9356.

(103) Huo, F. W.; Zheng, Z. J.; Zheng, G. F.; Giam, L. R.; Zhang, H.; Mirkin, C. A. *Science* **2008**, *321*, 1658.

(104) Sun, S. Q.; Mendes, P.; Critchley, K.; Diegoli, S.; Hanwell, M.; Evans, S. D.; Leggett, G. J.; Preece, J. A.; Richardson, T. H. *Nano Lett* **2006**, *6*, 345.

(105) Larsson, A.; Du, C. X.; Liedberg, B. *Biomacromolecules* **2007**, *8*, 3511.

(106) Mendes, P. M.; Jacke, S.; Critchley, K.; Plaza, J.; Chen, Y.; Nikitin, K.; Palmer, R. E.; Preece, J. A.; Evans, S. D.; Fitzmaurice, D. *Langmuir* **2004**, *20*, 3766.

(107) Bruckbauer, A.; Zhou, D. J.; Kang, D. J.; Korchev, Y. E.; Abell, C.; Klenerman, D. *J Am Chem Soc* **2004**, *126*, 6508.

(108) Singhvi, R.; Kumar, A.; Lopez, G. P.; Stephanopoulos, G. N.; Wang, D. I. C.; Whitesides, G. M.; Ingber, D. E. *Science* **1994**, *264*, 696.

(109) Fan, Z. Y.; Ho, J. C.; Jacobson, Z. A.; Yerushalmi, R.; Alley, R. L.; Razavi, H.; Javey, A. *Nano Lett* **2008**, *8*, 20.

(110) Hoff, J. D.; Cheng, L. J.; Meyhofer, E.; Guo, L. J.; Hunt, A. J. *Nano Lett* **2004**, *4*, 853.

(111) Binnig, G.; Quate, C. F.; Gerber, C. *Phys Rev Lett* **1986**, *56*, 930.

(112) Nuzzo, R. G.; Dubois, L. H.; Allara, D. L. *J Am Chem Soc* **1990**, *112*, 558.

(113) Yang, G. H.; Amro, N. A.; Liu, G. Y. *P Soc Photo-Opt Ins* **2003**, *5220*, 52.

(114) Kim, S.; Nah, J.; Jo, I.; Shahrjerdi, D.; Colombo, L.; Yao, Z.; Tutuc, E.; Banerjee, S. K. *Appl Phys Lett* **2009**, *94*.

(115) Xu, M. S.; Fujita, D.; Sagisaka, K.; Watanabe, E.; Hanagata, N. *Acs Nano* **2011**, *5*, 1522.

(116) Masubuchi, S.; Ono, M.; Yoshida, K.; Hirakawa, K.; Machida, T. *Appl Phys Lett* **2009**, *94*.

(117) Wang, W. M.; Stander, N.; Stoltenberg, R. M.; Goldhaber-Gordon, D.; Bao, Z. A. *Acs Nano* **2010**, *4*, 6409.

(118) Bao, W. Z.; Liu, G.; Zhao, Z.; Zhang, H.; Yan, D.; Deshpande, A.; LeRoy, B. J.; Lau, C. N. *Nano Res* **2010**, *3*, 98.

(119) Girit, C. O.; Zettl, A. *Appl Phys Lett* **2007**, *91*.

(120) Blake, P.; Hill, E. W.; Neto, A. H. C.; Novoselov, K. S.; Jiang, D.; Yang, R.; Booth, T. J.; Geim, A. K. *Appl Phys Lett* **2007**, *91*.

(121) Ferrari, A. C.; Meyer, J. C.; Scardaci, V.; Casiraghi, C.; Lazzeri, M.; Mauri, F.; Piscanec, S.; Jiang, D.; Novoselov, K. S.; Roth, S.; Geim, A. K. *Phys Rev Lett* **2006**, *97*.

(122) Geissler, M.; Wolf, H.; Stutz, R.; Delamarche, E.; Grummt, U. W.; Michel, B.; Bietsch, A. *Langmuir* **2003**, *19*, 6301.

(123) Koch, R. *J Phys-Condens Mat* **1994**, *6*, 9519.

(124) Saha, S. K.; Culpepper, M. L. *Appl Phys Lett* **2010**, *96*.

(125) Rosa, L. G.; Liang, J. *J Phys-Condens Mat* **2009**, *21*, 483001.

(126) Tian, Z. Q.; Ren, B.; Li, J. F.; Yang, Z. L. *Chem Commun* **2007**, 3514.

(127) Pettinger, B.; Domke, K. F.; Zhang, D.; Picardi, G.; Schuster, R. *Surf Sci* **2009**, *603*, 1335.

(128) Poborchii, V.; Tada, T.; Kanayama, T.; Geshev, P. *Journal of Raman Spectroscopy* **2009**, *40*, 1377.

(129) Taguchi, A.; Hayazawa, N.; Furusawa, K.; Ishitobi, H.; Kawata, S. *Journal of Raman Spectroscopy* **2009**, *40*, 1324.

(130) Hartschuh, A.; Anderson, N.; Novotny, L. *Journal of Microscopy-Oxford* **2003**, *210*, 234.

(131) Yi, K. J.; He, X. N.; Zhou, Y. S.; Xiong, W.; Lu, Y. F. *Review of Scientific Instruments* **2008**, *79*, 073706.

(132) Berweger, S.; Raschke, M. B. *Anal Bioanal Chem* **2010**, *396*, 115.

(133) Kudelski, A. *Surf Sci* **2009**, *603*, 1328.

(134) Hayazawa, N.; Inouye, Y.; Sekkat, Z.; Kawata, S. *Chem. Phys. Lett.* **2001**, *335*, 369.

(135) Orendorff, C. J.; Gole, A.; Sau, T. K.; Murphy, C. J. *Anal Chem* **2005**, *77*, 3261.

(136) Shim, S.; Stuart, C. M.; Mathies, R. A. *Chemphyschem* **2008**, *9*, 697.

(137) Neacsu, C. C.; Dreyer, J.; Behr, N.; Raschke, M. B. *Phys Rev B* **2006**, *73*, 193406.

(138) Pettinger, B.; Ren, B.; Picardi, G.; Schuster, R.; Ertl, G. *Phys Rev Lett* **2004**, *92*, 096101.

(139) Barrios, C. A.; Malkovskiy, A. V.; Kisliuk, A. M.; Sokolov, A. P.; Foster, M. D. *J Phys Chem C* **2009**, *113*, 8158.

(140) Richter, M.; Hedegaard, M.; Deckert-Gaudig, T.; Lampen, P.; Deckert, V. *Small* **2011**, *7*, 209.

(141) Krasnoslobodtsev, A. V.; Portillo, A. M.; Deckert-Gaudig, T.; Deckert, V.; Lyubchenko, Y. L. *Prion* **2010**, *4*, 265.

(142) Pan, D. H.; Klymyshyn, N.; Hu, D. H.; Lu, H. P. *Appl Phys Lett* **2006**, *88*.

(143) Berweger, S.; Neacsu, C. C.; Mao, Y. B.; Zhou, H. J.; Wong, S. S.; Raschke, M. B. *Nat Nanotechnol* **2009**, *4*, 496.

(144) Yano, T. A.; Ichimura, T.; Taguchi, A.; Hayazawa, N.; Verma, P.; Inouye, Y.; Kawata, S. *Appl Phys Lett* **2007**, *91*.

(145) Willets, K. A.; Van Duyne, R. P. In *Annu Rev Phys Chem* 2007; Vol. 58, p 267.

(146) Du, C. L.; Du, C. J.; You, Y. M.; Zhu, Y.; Jin, S. L.; He, C. J.; Shi, D. N. *Appl Optics* **2011**, *50*, 4922.

(147) Lau, D.; Hughes, A. E.; Muster, T. H.; Davis, T. J.; Glenn, A. M. *Microsc Microanal* **2010**, *16*, 13.

(148) Korte, K. E.; Skrabalak, S. E.; Xia, Y. N. *J Mater Chem* **2008**, *18*, 437.

(149) Geissler, M.; Schmid, H.; Bietsch, A.; Michel, B.; Delamarche, E. *Langmuir* **2002**, *18*, 2374.

(150) Chen, S. Y.; Ho, P. H.; Shiue, R. J.; Chen, C. W.; Wang, W. H. *Nano Lett* **2012**, *12*, 964.

(151) Lafkioti, M.; Krauss, B.; Lohmann, T.; Zschieschang, U.; Klauk, H.; von Klitzing, K.; Smet, J. H. *Nano Lett* **2010**, *10*, 1149.

(152) Balog, R.; Jorgensen, B.; Nilsson, L.; Andersen, M.; Rienks, E.; Bianchi, M.; Fanetti, M.; Laegsgaard, E.; Baraldi, A.; Lizzit, S.; Sljivancanin, Z.; Besenbacher, F.; Hammer, B.; Pedersen, T. G.; Hofmann, P.; Hornekaer, L. *Nat Mater* **2010**, *9*, 315.

(153) Zhang, H.; Bekyarova, E.; Huang, J. W.; Zhao, Z.; Bao, W. Z.; Wang, F. L.; Haddon, R. C.; Lau, C. N. *Nano Lett* **2011**, *11*, 4047.

(154) Fang, Y. R.; Wei, H.; Hao, F.; Nordlander, P.; Xu, H. X. *Nano Lett* **2009**, *9*, 2049.

(155) Kusar, P.; Gruber, C.; Hohenau, A.; Krenn, J. R. *Nano Lett* **2012**, *12*, 661.

APPENDIX A

SOURCE CODES OF NANOSHAVING PATTERNING

The following source codes are to generate a script to control WITec AFM, which would make a graphene pattern for graphene transistors. The codes can be compiled by Microsoft QuickBASIC, and run under DOS environment.

```
DEF FNround (Num)
  IF INSTR(STR$(Num), "E") = 0 THEN
    IF MID$(STR$(Num), INSTR(STR$(Num), ".") + 4, 1) > "5" THEN
      FNround = VAL(MID$(STR$(Num + SGN(Num) * .001), 1, INSTR(STR$(Num +
SGN(Num) * .001), ".") + 3))
    ELSE
      FNround = VAL(MID$(STR$(Num), 1, INSTR(STR$(Num), ".") + 3))
    END IF
  ELSE
    FNround = VAL(MID$(STR$(Num), 1, INSTR(STR$(Num), ".") + 2) + MID$(STR$(Num),
INSTR(STR$(Num), "E")))
  END IF
END DEF

INPUT "1st point (um,um): ", x1, y1
INPUT "2nd point (um,um): ", x2, y2
INPUT "Channel width (3 um): ", w
INPUT "Output filename (T.txt): ", F$
IF F$ = "" THEN F$ = "T.txt"
IF w = 0 THEN w = 3
Ax = x2 - x1
Ay = y2 - y1
Axn = Ax / SQR(Ax ^ 2 + Ay ^ 2)
Ayn = Ay / SQR(Ax ^ 2 + Ay ^ 2)
Bx = y2 - y1
By = x1 - x2
IF By < 0 THEN
  Bx = -Bx
  By = -By
END IF
Bxn = Bx / SQR(Bx ^ 2 + By ^ 2)
Byn = By / SQR(Bx ^ 2 + By ^ 2)

OPEN F$ FOR OUTPUT AS #1
PRINT #1, "dm ("; CHR$(34); "Gain setting delay."; CHR$(34); ");"
PRINT #1, "sl (10000);"
PRINT #1, "ms (20);"
PRINT #1, "sp (0.1);"
```

```
PRINT #1, "mz (20);"
PRINT #1, ""
PRINT #1, "ma ("; FNround(x1 + (w / 2) * Bxn+(SQR(Ax ^ 2 + Ay ^ 2)-3)/2*Axn); ",";
FNround(y1 + (w / 2) * Byn+(SQR(Ax ^ 2 + Ay ^ 2)-3)/2*Ayn); ");"
PRINT #1, "ms (1);"
PRINT #1, "mz (-20);"
PRINT #1, "ms (20);"
PRINT #1, "wpos ();"
PRINT #1, "sp (9.5);"
PRINT #1, "wpos ();"
' 1X3 rect in the top
PRINT #1, "dm ("; CHR$(34); "1X3 rect in the top"; CHR$(34); ");"
FOR n = 0 TO 1 STEP .02
  IF n <> 0 THEN PRINT #1, "mr ("; FNround(.02 * Bxn); ","; FNround(.02 * Byn); ");"
  FOR m = 1 TO 8
    PRINT #1, "mr ("; FNround(3*Axn); ","; FNround(3*Ayn); ");";
    PRINT #1, "mr ("; FNround(-3*Axn); ","; FNround(-3*Ayn); ");";
  NEXT
NEXT
' Gap
PRINT #1, "dm ("; CHR$(34); "Gap rect in the middle"; CHR$(34); ");"

FOR n = 0 TO SQR(Ax ^ 2 + Ay ^ 2) STEP .02
  IF n = 0 THEN
    PRINT #1, "mr ("; FNround((3-SQR(Ax ^ 2 + Ay ^ 2))/2*Axn); ","; FNround((3-SQR(Ax ^ 2
+ Ay ^ 2))/2*Ayn); ");";
  ELSE
    PRINT #1, "mr ("; FNround(.02 * Axn); ","; FNround(.02 * Ayn); ");"
  END IF
  FOR m = 1 TO 8
    PRINT #1, "mr ("; FNround(-(w+2)*Bxn); ","; FNround(-(w+2)*Byn); ");";
    PRINT #1, "mr ("; FNround((w+2)*Bxn); ","; FNround((w+2)*Byn); ");";
  NEXT
NEXT
' 1X3 rect in the bottom
PRINT #1, "dm ("; CHR$(34); "1X3 rect in the bottom"; CHR$(34); ");"

FOR n = 0 TO 1 STEP .02
  IF n = 0 THEN
    PRINT #1, "mr ("; FNround(-(w+1)*Bxn); ","; FNround(-(w+1)*Byn); ");"
    PRINT #1, "mr ("; FNround((-SQR(Ax ^ 2 + Ay ^ 2)-3)/2*Axn); ","; FNround((-SQR(Ax ^ 2
+ Ay ^ 2)-3)/2*Ayn); ");";
  ELSE
    PRINT #1, "mr ("; FNround(-.02 * Bxn); ","; FNround(-.02 * Byn); ");"
  END IF
  FOR m = 1 TO 8
    PRINT #1, "mr ("; FNround(3*Axn); ","; FNround(3*Ayn); ");";
    PRINT #1, "mr ("; FNround(-3*Axn); ","; FNround(-3*Ayn); ");";
  NEXT
NEXT
```

```
PRINT #1, "ma ("; FNround(x1 - (w / 2) * Bxn+(SQR(Ax ^ 2 + Ay ^ 2)-1)/2*Axn); ",";
FNround(y1 - (w / 2) * Byn+(SQR(Ax ^ 2 + Ay ^ 2)-1)/2*Ayn); ");"
PRINT #1, "ms (100);"
PRINT #1, "wpos ();"
PRINT #1, "sp (9.5);"
PRINT #1, "wpos ();"

IF Bxn >= 0 THEN
  ' Line to the lower edge
  PRINT #1, "dm ("; CHR$(34); "Line to the lower edge."; CHR$(34); ");"
  FOR n = 0 TO 1 STEP .02
    IF Bxn <> 0 THEN kx = -(-49.9 - ((x1 - (w / 2) * Bxn+(SQR(Ax ^ 2 + Ay ^ 2)-1)/2*Axn) + n
* Axn)) / Bxn ELSE kx = 1000
    IF Byn <> 0 THEN ky = -(-49.9 - ((y1 - (w / 2) * Byn+(SQR(Ax ^ 2 + Ay ^ 2)-1)/2*Ayn) + n
* Ayn)) / Byn ELSE ky = 1000
    IF ky > kx THEN k = kx ELSE k = ky
    IF n <> 0 THEN PRINT #1, "mr ("; FNround(.02 * Axn); ","; FNround(.02 * Ayn); ");"
    FOR m = 1 TO 4
      PRINT #1, "mr ("; FNround(-k * Bxn); ","; FNround(-k * Byn); ");";
      PRINT #1, "mr ("; FNround(k * Bxn); ","; FNround(k * Byn); ");";
    NEXT
  NEXT

  ' Line to the lower corner
  PRINT #1, "dm ("; CHR$(34); "Line to the lower corner."; CHR$(34); ");"
  PRINT #1, "sp (0.1);"
  PRINT #1, "mz (20);"
  IF Bxn <> 0 THEN kx = -(-49.9 - ((x1 - (w / 2) * Bxn+(SQR(Ax ^ 2 + Ay ^ 2)-1)/2*Axn) + Ax
/ 2)) / Bxn ELSE kx = 1000
  IF Byn <> 0 THEN ky = -(-49.9 - ((y1 - (w / 2) * Byn+(SQR(Ax ^ 2 + Ay ^ 2)-1)/2*Ayn) + Ay
/ 2)) / Byn ELSE ky = 1000
  IF ky > kx THEN k = kx ELSE k = ky
  x = x1 - (2 + w / 2 + k) * Bxn + Ax / 2
  y = y1 - (2 + w / 2 + k) * Byn + Ay / 2
  IF y > -49.89 THEN
    PRINT #1, "ma (-49 ,"; FNround(y + 1); ");"
    PRINT #1, "ms (1);"
    PRINT #1, "mz (-20);"
    PRINT #1, "ms (100);"
    PRINT #1, "wpos ();"
    PRINT #1, "sp (9.5);"
    PRINT #1, "wpos ();"
    FOR n = 0 TO .9 STEP .02
    IF n <> 0 THEN PRINT #1, "mr (-0.02,0);"
      FOR m = 1 TO 4
        PRINT #1, "mr ( 0 ,"; FNround(-49.9 - y - 1); ");";
        PRINT #1, "mr ( 0 ,"; FNround(49.9 + y + 1); ");";
      NEXT
    NEXT
  ELSE
    PRINT #1, "ma ("; FNround(x + 1); ", -49 );"
    PRINT #1, "ms (1);"
    PRINT #1, "mz (-20);"
```

```
    PRINT #1, "ms (100);"
    PRINT #1, "wpos ();"
    PRINT #1, "sp (9.5);"
    PRINT #1, "wpos ();"
    FOR n = 0 TO .9 STEP .02
    IF n <> 0 THEN PRINT #1, "mr (0,-0.02);"
      FOR m = 1 TO 4
        PRINT #1, "mr ("; FNround(-49.9 - x - 1); ", 0 );";
        PRINT #1, "mr ("; FNround(49.9 + x + 1); ", 0 );";
      NEXT
    NEXT
  END IF

  PRINT #1, ""
  PRINT #1, "ms (10);"
  PRINT #1, "sp (0.1);"
  PRINT #1, "mz (20);"
  PRINT #1, "ma ("; FNround(x1 + (w / 2) * Bxn+(SQR(Ax ^ 2 + Ay ^ 2)-1)/2*Axn); ",";
FNround(y1 + (w / 2) * Byn+(SQR(Ax ^ 2 + Ay ^ 2)-1)/2*Ayn); ");"
  PRINT #1, "ms (1);"
  PRINT #1, "mz (-20);"
  PRINT #1, "ms (100);"
  PRINT #1, "wpos ();"
  PRINT #1, "sp (9.5);"
  PRINT #1, "wpos ();"
  ' Line to the upper edge
  PRINT #1, "dm ("; CHR$(34); "Line to the upper edge."; CHR$(34); ");"
  FOR n = 0 TO 1 STEP .02
    IF Bxn <> 0 THEN kx = (49.9 - ((x1 + (w / 2) * Bxn+(SQR(Ax ^ 2 + Ay ^ 2)-1)/2*Axn) + n *
Axn)) / Bxn ELSE kx = 1000
    IF Byn <> 0 THEN ky = (49.9 - ((y1 + (w / 2) * Byn+(SQR(Ax ^ 2 + Ay ^ 2)-1)/2*Ayn) + n *
Ayn)) / Byn ELSE ky = 1000
    IF ky > kx THEN k = kx ELSE k = ky
    IF n <> 0 THEN PRINT #1, "mr ("; FNround(.02 * Axn); ","; FNround(.02 * Ayn); ");"
    FOR m = 1 TO 4
      PRINT #1, "mr ("; FNround(k * Bxn); ","; FNround(k * Byn); ");";
      PRINT #1, "mr ("; FNround(-k * Bxn); ","; FNround(-k * Byn); ");";
    NEXT
  NEXT

  ' Line to the upper corner
  PRINT #1, "dm ("; CHR$(34); "Line to the upper corner."; CHR$(34); ");"
  PRINT #1, "sp (0.1);"
  PRINT #1, "mz (20);"
  IF Bxn <> 0 THEN kx = (49.9 - ((x1 + (w / 2) * Bxn+(SQR(Ax ^ 2 + Ay ^ 2)-1)/2*Axn) + Ax /
2)) / Bxn ELSE kx = 1000
  IF Byn <> 0 THEN ky = (49.9 - ((y1 + (w / 2) * Byn+(SQR(Ax ^ 2 + Ay ^ 2)-1)/2*Ayn) + Ay /
2)) / Byn ELSE ky = 1000
  IF ky > kx THEN k = kx ELSE k = ky
  x = x1 + (2 + w / 2 + k) * Bxn + Ax / 2
  y = y1 + (2 + w / 2 + k) * Byn + Ay / 2
  IF y < 49.89 THEN
    PRINT #1, "ma (49 ,"; FNround(y - 1); ");"
```

```
    PRINT #1, "ms (1);"
    PRINT #1, "mz (-20);"
    PRINT #1, "ms (100);"
    PRINT #1, "wpos ();"
    PRINT #1, "sp (9.5);"
    PRINT #1, "wpos ();"
    FOR n = 0 TO .9 STEP .02
      IF n <> 0 THEN PRINT #1, "mr (0.02, 0);"
      FOR m = 1 TO 4
        PRINT #1, "mr ( 0 ,"; FNround(49.9 - y + 1); ");";
        PRINT #1, "mr ( 0 ,"; FNround(-49.9 + y - 1); ");";
      NEXT
    NEXT
  ELSE
    PRINT #1, "ma ("; FNround(x - 1); ", 49 );"
    PRINT #1, "ms (1);"
    PRINT #1, "mz (-20);"
    PRINT #1, "ms (100);"
    PRINT #1, "wpos ();"
    PRINT #1, "sp (9.5);"
    PRINT #1, "wpos ();"
    FOR n = 0 TO .9 STEP .02
      IF n <> 0 THEN PRINT #1, "mr (0, 0.02);"
      FOR m = 1 TO 4
        PRINT #1, "mr ("; FNround(49.9 - x + 1); ", 0 );";
        PRINT #1, "mr ("; FNround(-49.9 + x - 1); ", 0 );";
      NEXT
    NEXT
  END IF

ELSE
  ' Line to the lower edge
  PRINT #1, "dm ("; CHR$(34); "Line to the lower edge."; CHR$(34); ");"
  FOR n = 0 TO 1 STEP .02
    kx = -(49.9 - ((x1 - (w / 2) * Bxn+(SQR(Ax ^ 2 + Ay ^ 2)-1)/2*Axn) + n * Axn)) / Bxn
    IF Byn <> 0 THEN ky = -(-49.9 - ((y1 + (w / 2) * Byn+(SQR(Ax ^ 2 + Ay ^ 2)-1)/2*Ayn) + n
* Ayn)) / Byn ELSE ky = 1000
    IF ky > kx THEN k = kx ELSE k = ky
    IF n <> 0 THEN PRINT #1, "mr ("; FNround(.02 * Axn); ","; FNround(.02 * Ayn); ");"
    FOR m = 1 TO 4
      PRINT #1, "mr ("; FNround(-k * Bxn); ","; FNround(-k * Byn); ");";
      PRINT #1, "mr ("; FNround(k * Bxn); ","; FNround(k * Byn); ");";
    NEXT
  NEXT

  ' Line to the lower corner
  PRINT #1, "dm ("; CHR$(34); "Line to the lower corner."; CHR$(34); ");"
  PRINT #1, "sp (0.1);"
  PRINT #1, "mz (20);"
  kx = -(49.9 - ((x1 - (w / 2) * Bxn+(SQR(Ax ^ 2 + Ay ^ 2)-1)/2*Axn) + Ax / 2)) / Bxn
  IF Byn <> 0 THEN ky = -(-49.9 - ((y1 - (w / 2) * Byn+(SQR(Ax ^ 2 + Ay ^ 2)-1)/2*Ayn) + Ay
/ 2)) / Byn ELSE ky = 1000
  IF ky > kx THEN k = kx ELSE k = ky
```

```
  x = x1 - (2 + w / 2 + k) * Bxn + Ax / 2
  y = y1 - (2 + w / 2 + k) * Byn + Ay / 2
  IF y > -49.89 THEN
    PRINT #1, "ma (49 ,"; FNround(y + 1); ");"
    PRINT #1, "ms (1);"
    PRINT #1, "mz (-20);"
    PRINT #1, "ms (100);"
    PRINT #1, "wpos ();"
    PRINT #1, "sp (9.5);"
    PRINT #1, "wpos ();"
    FOR n = 0 TO .9 STEP .02
      IF n <> 0 THEN PRINT #1, "mr (0.02,0);"
      FOR m = 1 TO 4
        PRINT #1, "mr ( 0 ,"; FNround(-49.9 - y - 1); ");";
        PRINT #1, "mr ( 0 ,"; FNround(49.9 + y + 1); ");";
      NEXT
    NEXT
  ELSE
    PRINT #1, "ma ("; FNround(x - 1); ", -49 );"
    PRINT #1, "ms (1);"
    PRINT #1, "mz (-20);"
    PRINT #1, "ms (100);"
    PRINT #1, "wpos ();"
    PRINT #1, "sp (9.5);"
    PRINT #1, "wpos ();"
    FOR n = 0 TO .9 STEP .02
      IF n <> 0 THEN PRINT #1, "mr (0,-0.02);"
      FOR m = 1 TO 4
        PRINT #1, "mr ("; FNround(49.9 - x + 1); ", 0 );";
        PRINT #1, "mr ("; FNround(-49.9 + x - 1); ", 0 );";
      NEXT
    NEXT
  END IF

  PRINT #1, ""
  PRINT #1, "ms (10);"
  PRINT #1, "sp (0.1);"
  PRINT #1, "mz (20);"
  PRINT #1, "ma ("; FNround((x1 + (w / 2) * Bxn+(SQR(Ax ^ 2 + Ay ^ 2)-1)/2*Axn)); ",";
FNround((y1 + (w / 2) * Byn+(SQR(Ax ^ 2 + Ay ^ 2)-1)/2*Ayn)); ");"
  PRINT #1, "ms (1);"
  PRINT #1, "mz (-20);"
  PRINT #1, "ms (100);"
  PRINT #1, "wpos ();"
  PRINT #1, "sp (9.5);"
  PRINT #1, "wpos ();"
  ' Line to the upper edge
  PRINT #1, "dm ("; CHR$(34); "Line to the upper edge."; CHR$(34); ");"
  FOR n = 0 TO 1 STEP .02
    IF Bxn <> 0 THEN kx = (-49.9 - (((x1 + (w / 2) * Bxn+(SQR(Ax ^ 2 + Ay ^ 2)-1)/2*Axn)) + n
* Axn)) / Bxn ELSE kx = 1000
    IF Byn <> 0 THEN ky = (49.9 - (((y1 + (w / 2) * Byn+(SQR(Ax ^ 2 + Ay ^ 2)-1)/2*Ayn)) + n
* Ayn)) / Byn ELSE ky = 1000
```

```
    IF ky > kx THEN k = kx ELSE k = ky
    IF n <> 0 THEN PRINT #1, "mr ("; FNround(.02 * Axn); ","; FNround(.02 * Ayn); ");"
    FOR m = 1 TO 4
      PRINT #1, "mr ("; FNround(k * Bxn); ","; FNround(k * Byn); ");";
      PRINT #1, "mr ("; FNround(-k * Bxn); ","; FNround(-k * Byn); ");";
    NEXT
  NEXT

  ' Line to the upper corner
  PRINT #1, "dm ("; CHR$(34); "Line to the upper corner."; CHR$(34); ");"
  PRINT #1, "sp (0.1);"
  PRINT #1, "mz (20);"
  IF Bxn <> 0 THEN kx = (-49.9 - (((x1 + (w / 2) * Bxn+(SQR(Ax ^ 2 + Ay ^ 2)-1)/2*Axn)) +
Ax / 2)) / Bxn ELSE kx = 1000
  IF Byn <> 0 THEN ky = (49.9 - (((y1 + (w / 2) * Byn+(SQR(Ax ^ 2 + Ay ^ 2)-1)/2*Ayn)) + Ay
/ 2)) / Byn ELSE ky = 1000
  IF ky > kx THEN k = kx ELSE k = ky
  x = x1 + (2 + w / 2 + k) * Bxn + Ax / 2
  y = y1 + (2 + w / 2 + k) * Byn + Ay / 2
  IF y < 49.89 THEN
    PRINT #1, "ma (-49 ,"; FNround(y - 1); ");"
    PRINT #1, "ms (1);"
    PRINT #1, "mz (-20);"
    PRINT #1, "ms (100);"
    PRINT #1, "wpos ();"
    PRINT #1, "sp (9.5);"
    PRINT #1, "wpos ();"
    FOR n = 0 TO .9 STEP .02
      IF n <> 0 THEN PRINT #1, "mr (-0.02,0);"
      FOR m = 1 TO 4
        PRINT #1, "mr ( 0 ,"; FNround(49.9 - y + 1); ");";
        PRINT #1, "mr ( 0 ,"; FNround(-49.9 + y - 1); ");";
      NEXT
    NEXT
  ELSE
    PRINT #1, "ma ("; FNround(x + 1); ", 49 );"
    PRINT #1, "ms (1);"
    PRINT #1, "mz (-20);"
    PRINT #1, "ms (100);"
    PRINT #1, "wpos ();"
    PRINT #1, "sp (9.5);"
    PRINT #1, "wpos ();"
    FOR n = 0 TO .9 STEP .02
      IF n <> 0 THEN PRINT #1, "mr (0, 0.02);"
      FOR m = 1 TO 4
        PRINT #1, "mr ("; FNround(-49.9 - x - 1); ", 0 );";
        PRINT #1, "mr ("; FNround(49.9 + x + 1); ", 0 );";
      NEXT
    NEXT
  END IF

END IF
```

```
PRINT #1, "sp (0.1);"
PRINT #1, "mz (20);"
```

APPENDIX B

SOURCE CODES OF ELECTRIC MEASUREMENTS

The following codes are to generate a controller for electric measurements for the lock-in amplifier (Stanford Research Systems SR830).. The codes consist of three main parts: a header, a resource script file, and a main body. In the header, all the variables and constants are defined. The resource file contains the information about dialog windows and related objects on the windows. The main body controls the amplifier and performs IV, gate effect, and time serious measurements. These codes can be compiled by FreeBASIC, and run under Microsoft Windows XP.

The header is listed in the following:

```
#Define IDD_DLG1 1000
#define IDC_BTN1 1001
#define IDC_BTN2 1002
#define IDC_SHP1 1003
#define IDC_BTN3 1004
#define IDC_BTN4 1005
#define IDC_BTN5 1006
#define IDC_BTN8 1007
#define IDD_DLG2 1100
#define IDC_BTN6 1103
#define IDC_BTN7 1104
#define IDC_GRP1 1119
#define IDC_EDT3 1107
#define IDC_STC3 1108
#define IDC_STC4 1109
#define IDC_EDT4 1110
#define IDC_EDT7 1115
#define IDC_STC7 1116
#define IDC_STC8 1117
#define IDC_EDT8 1118
#define IDC_GRP2 1120
#define IDC_STC1 1101
#define IDC_EDT1 1102
#define IDC_EDT2 1105
#define IDC_STC2 1106
#define IDC_EDT9 1121
```

```
#define IDC_STC9 1122
#define IDC_GRP3 1123
#define IDC_STC5 1111
#define IDC_EDT5 1112
#define IDC_EDT6 1113
#define IDC_STC6 1114
#define IDC_EDT10 1124
#define IDC_STC10 1125
#define IDC_STC11 1126
#define IDC_EDT11 1127
#define IDC_EDT14 1133
#define IDC_STC14 1134
#define IDC_EDT13 1131
#define IDC_STC13 1132
#define IDC_EDT12 1129
#define IDC_STC12 1130

#define IDT_Timer1 2000

Const szNULL=!"\0"
Const szFilter      = "Text Files" & szNULL & "*.txt" & szNULL & "Excel Files" & szNULL &
"*.csv" & szNULL


#Define MTIMER            10          ' Speed
#Define WaitComm          30          ' Waiting time in ms. after query sent
#Define WaitTras0.003     ' Waiting time in sec. after a byte read
#define DefBoundaryPass  0.001     ' Tolerance of data collecting
Dim Shared BoundaryPass As Double
#Define Margin   20          ' Margin

Dim Shared Comport As Integer, FileNum As Integer
Dim Shared hInstance As HMODULE
Dim Shared hWinTimer As HWND, hWinPara As HWND
Dim Shared hShp As HWND
Dim Shared mDC As HDC
Dim Shared hOldBmp As HBITMAP
Dim Shared lpOldBoardProc As Any Ptr
Dim Shared Pause As BOOLEAN   ' if pause
Dim Shared IVorIGorTS As integer'           0:IV; 1:IG; 2:TS
Dim Shared Filename As String

#define DefRate   10          ' Sample rate (4~13: 1~512 Hz)
Dim Shared Rate As Integer
#define DefDepthxBuff     30          ' Depth of xBuff (32 at most)
Dim Shared DepthxBuff As Integer
Dim Shared xBuff(32) As Double
Dim Shared yBuff(32) As Double
Dim Shared xi As Integer, MaxValue As Double, MinValue As Double, Avg As Double,
Boundary As Double

#define DefStepLIV          72          ' Num of steps for Linear IV (999 at most)
Dim Shared StepLIV As Integer
```

```
#Define DefSleepTime      500       ' Time to sleep after setting a new Volt
Dim Shared SleepTime As Integer
#define DefVBound         0.71      'HBound of Linear IV
Dim Shared VBound As Double

#Define PointSize         2         ' Size of a point

#define DefGIBound        10.5      ' Initial Bound of IG
Dim Shared GIBound As Double
#define DefGFBound        -10.5     ' Final Bound of IG
Dim Shared GFBound As Double
#define DefStepIG         43        ' Num of steps for Linear IV (999 at most)
Dim Shared StepIG As Integer

#define DefFreq   16888    ' Frequency
Dim Shared Freq As Double

#define DefGBias0          ' Gate bias when doing IV curve
Dim Shared GBias As Double
#define DefDSBias         0.1       ' DS bias when doing Gate curve
Dim Shared DSBias As Double

#define DefStepTS         999       ' Num of steps for TimeSerious (999 at most)
Dim Shared StepTS As Integer
#define DefTSGBias        0         ' Gate bias when doing TimeSerious
Dim Shared TSGBias As Double
#Define DefTSDSBias       0.1       ' DS bias when doing TimeSerious
Dim Shared TSDSBias As Double

Dim Shared VStep(999) As Double, xResult(999) As Double, yResult(999) As Double, HResult
As Double
Dim Shared vi As Integer
```

The resource script is listed in the following:

```
#define IDD_DLG1 1000
#define IDC_BTN1 1001
#define IDC_BTN2 1002
#define IDC_SHP1 1003
#define IDC_BTN3 1004
#define IDC_BTN4 1005
#define IDC_BTN5 1006
#define IDC_BTN8 1007
#define IDD_DLG2 1100
#define IDC_BTN6 1103
#define IDC_BTN7 1104
#define IDC_GRP1 1119
#define IDC_EDT3 1107
#define IDC_STC3 1108
```

```
#define IDC_STC4 1109
#define IDC_EDT4 1110
#define IDC_EDT7 1115
#define IDC_STC7 1116
#define IDC_STC8 1117
#define IDC_EDT8 1118
#define IDC_GRP2 1120
#define IDC_STC1 1101
#define IDC_EDT1 1102
#define IDC_EDT2 1105
#define IDC_STC2 1106
#define IDC_EDT9 1121
#define IDC_STC9 1122
#define IDC_GRP3 1123
#define IDC_STC5 1111
#define IDC_EDT5 1112
#define IDC_EDT6 1113
#define IDC_STC6 1114
#define IDC_EDT10 1124
#define IDC_STC10 1125
#define IDC_EDT11 1127
#define IDC_STC11 1126
#define IDC_GRP4 1128
#define IDC_EDT12 1129
#define IDC_STC12 1130
#define IDC_EDT13 1131
#define IDC_STC13 1132
#define IDC_EDT14 1133
#define IDC_STC14 1134

IDD_DLG1 DIALOGEX 6,5,312,282
CAPTION "Electric Measurement"
FONT 8,"MS Sans Serif",400,0,0
STYLE 0x10CE0800
BEGIN
  CONTROL "Parameters",IDC_BTN1,"Button",0x50010000,261,258,47,19
  CONTROL "Linear IV",IDC_BTN2,"Button",0x50010000,6,258,47,19
  CONTROL "",IDC_SHP1,"Static",0x50000004,3,3,306,249
  CONTROL "Pause",IDC_BTN3,"Button",0x50010000,159,258,47,19
  CONTROL "Gate curve",IDC_BTN4,"Button",0x50010000,57,258,47,19
  CONTROL "Save File...",IDC_BTN5,"Button",0x50010000,210,258,47,19
  CONTROL "Time serious",IDC_BTN8,"Button",0x50010000,108,258,47,19
END

IDD_DLG2 DIALOGEX 6,3,189,429
CAPTION "Parameters"
FONT 8,"MS Sans Serif",0,0,0
STYLE 0x10CF0000
BEGIN
  CONTROL "Update",IDC_BTN6,"Button",0x50010000,99,396,81,24
  CONTROL "Set default values",IDC_BTN7,"Button",0x50010000,6,396,81,24
  CONTROL "Data Collecting",IDC_GRP1,"Button",0x50000007,6,3,177,99
  CONTROL "",IDC_EDT3,"Edit",0x50010000,96,78,66,12,0x00000200
```

```
  CONTROL "Sample rate (Hz):",IDC_STC3,"Static",0x50000201,24,79,72,9
  CONTROL "Average:",IDC_STC4,"Static",0x50000201,24,59,72,9
  CONTROL "",IDC_EDT4,"Edit",0x50010000,96,58,66,12,0x00000200
  CONTROL "",IDC_EDT7,"Edit",0x50010000,96,38,66,12,0x00000200
  CONTROL "Fluctuation (%):",IDC_STC7,"Static",0x50000201,24,39,72,9
  CONTROL "Pause (ms):",IDC_STC8,"Static",0x50000201,24,19,72,9
  CONTROL "",IDC_EDT8,"Edit",0x50010000,96,18,66,12,0x00000200
  CONTROL "IV Curve",IDC_GRP2,"Button",0x50000007,6,105,177,84
  CONTROL "Number of Steps:",IDC_STC1,"Static",0x50000201,24,147,72,9
  CONTROL "",IDC_EDT1,"Edit",0x50010000,96,146,66,12,0x00000200
  CONTROL "",IDC_EDT2,"Edit",0x50010000,96,126,66,12,0x00000200
  CONTROL "Bias Range (V):",IDC_STC2,"Static",0x50000201,24,127,72,9
  CONTROL "",IDC_EDT9,"Edit",0x50010000,96,166,66,12,0x00000200
  CONTROL "Gate Bias (V):",IDC_STC9,"Static",0x50000201,24,167,72,9
  CONTROL "Gate Curve",IDC_GRP3,"Button",0x50000007,6,195,177,102
  CONTROL "Initial Gate Bias (V):",IDC_STC5,"Static",0x50000201,24,214,72,9
  CONTROL "",IDC_EDT5,"Edit",0x50010000,96,213,66,12,0x00000200
  CONTROL "",IDC_EDT6,"Edit",0x50010000,96,253,66,12,0x00000200
  CONTROL "Number of Steps:",IDC_STC6,"Static",0x50000201,24,254,72,9
  CONTROL "",IDC_EDT10,"Edit",0x50010000,96,273,66,12,0x00000200
  CONTROL "DS Bias (V):",IDC_STC10,"Static",0x50000201,24,274,72,9
  CONTROL "",IDC_EDT11,"Edit",0x50010000,96,233,66,12,0x00000200
  CONTROL "Final Gate Bias (V):",IDC_STC11,"Static",0x50000201,24,234,72,9
  CONTROL "Time Serious",IDC_GRP4,"Button",0x50000007,6,306,177,81
  CONTROL "",IDC_EDT12,"Edit",0x50010000,96,364,66,12,0x00000200
  CONTROL "Number of Steps:",IDC_STC12,"Static",0x50000201,24,365,72,9
  CONTROL "",IDC_EDT13,"Edit",0x50010000,96,344,66,12,0x00000200
  CONTROL "Gate Bias (V):",IDC_STC13,"Static",0x50000201,24,345,72,9
  CONTROL "",IDC_EDT14,"Edit",0x50010000,96,324,66,12,0x00000200
  CONTROL "DS Bias (V):",IDC_STC14,"Static",0x50000201,24,325,72,9
END
```

The main body is listed in the following:

```
/'
Dialog Example, by fsw

compile with:     fbc -s gui dialog.rc dialog.bas

'/

#Include Once "windows.bi"
#Include Once "win/winuser.bi"
#Include Once "win/commdlg.bi"
#Include "Elec.bi"

Declare Function DlgProc(ByVal hWin As HWND, ByVal uMsg As UINT, ByVal wParam As
WPARAM, ByVal lParam As LPARAM) As Integer
```

```
Declare Function DlgProc2(ByVal hWin As HWND, ByVal uMsg As UINT, ByVal wParam As
WPARAM, ByVal lParam As LPARAM) As Integer
Declare Sub Query OverLoad (Comm As String, v1 As String)
Declare Sub Query OverLoad (Comm As String, ByRef v1 As Double)
Declare Sub Query OverLoad (Comm As String, ByRef v1 As Double, ByRef v2 As Double)
Declare Sub Query OverLoad (Comm As String, ByRef v1 As Double, ByRef v2 As Double,
ByRef v3 As Double)
Declare Sub Query OverLoad (Comm As String, ByRef v1 As Double, ByRef v2 As Double,
ByRef v3 As Double, ByRef v4 As Double)
Declare Sub Query OverLoad (Comm As String, pBuff As Double Pointer, num As Integer)
Declare Sub SendComm(Comm As String, Pause As Integer)
Declare Sub TimerProc(ByVal hWin As HWND,ByVal uMsg As UINT,ByVal wParam As
WPARAM,ByVal lParam As LPARAM)
Declare Function BoardProc(ByVal hWin As HWND,ByVal uMsg As UINT,ByVal wParam As
WPARAM,ByVal lParam As LPARAM) As Integer
Declare Sub UpodateIVBoard(ByVal hWin As HWND,ByVal hDC As HDC)
Declare Function SaveFile(ByVal hWin As HWND) As String
Declare Function Digi(a As Double, b As Integer) As String

Dim Shared BlackThickPen As HPEN
Dim Shared BlackDashPen As HPEN
Dim Shared BlackPen As HPEN
BlackThickPen=CreatePen(PS_SOLID, 3, &H0)
BlackDashPen=CreatePen(PS_DASH, 1, &H0)
BlackPen=CreatePen(PS_SOLID, 1, &H0)
'''
''' Program start
'''
Dim As Integer i, j, k
Dim reading As String
Comport=FreeFile()
i=Open Com ("Com1: 19200, N, 8, 1, CS0, DS0, CD0", As Comport)
'SendComm "*RST", 2000
Query "OUTX0; *IDN?", reading
If i<>0 Or Len(reading)=0 Then
ScreenRes 300,100,16
Paint (0,0),RGB(230,230,230)
Color RGB(0, 0, 0), RGB(230,230,230)
Print i, reading
Print "Lock-in Amp is not connected"
For i=5 To 0 Step -1
Print i
Sleep 999
Locate 3,1
Print "     "
Locate 3,1
Next
End
EndIf
For i =0 To DefStepLIV-1
VStep(i)=DefVBound*i/(DefStepLIV-1)
Next
SendComm "FREQ"+Str(DefFreq), DefSleepTime
```

```
SendComm "SLVL"+Str(VStep(1)), DefSleepTime
Query "FREQ ?", Freq
vi=0
For i =0 To DepthxBuff-1
xBuff(i)=0
Next
Avg=1
Boundary=Avg*BoundaryPass
''
'' Create the Dialog
''

hInstance=GetModuleHandle(NULL)
DialogBoxParam(hInstance, Cast(ZString Ptr,IDD_DLG1), NULL, @DlgProc, NULL)
''
'' Program has ended
''

ExitProcess(0)
Close
End

'''
''' Program end
'''
Sub UpodateIVBoard(ByVal hWin As HWND,ByVal hDC As HDC)
Dim rect As RECT
Dim num As Integer

If StepLIV>DepthxBuff Then num=StepLIV-1 Else num=DepthxBuff-1
Dim pArray(num) As Point
Dim pBox(5) As Point
Dim i As Integer


'Clean the whole thing
GetClientRect(hWin,@rect)
FillRect(mDC,@rect,GetStockObject(WHITE_BRUSH))

'Draw the instant buffer output
For i =0 To DepthxBuff-1
pArray(i).x=i*(rect.right-rect.left)/(DepthxBuff-1)+rect.left
pArray(i).y=(xBuff(i)-Avg-Boundary)/(-2*Boundary)*(rect.bottom-
((rect.bottom+rect.top)/2+20)-2*Margin-4)+((rect.bottom+rect.top)/2+Margin)+Margin+2
Next


SelectObject(mDC, BlackThickPen)
pBox(0).x=rect.left
pBox(0).y=((rect.bottom+rect.top)/2+Margin)+Margin
pBox(1).x=rect.right
pBox(1).y=pBox(0).y
Polyline(mDC, @pBox(0), 2)
```

```
TextOut(mDC, 0,((rect.bottom+rect.top)/2+Margin),Str(Boundary/avg*100)+"%",
Len(Str(Boundary/avg*100)+"%"))

pBox(0).y=rect.Bottom-Margin
pBox(1).y=pBox(0).y
Polyline(mDC, @pBox(0), 2)
TextOut(mDC, 0,pBox(0).y+3,Str(-Boundary/avg*100)+"%", Len(Str(-
Boundary/avg*100)+"%"))

SelectObject(mDC, BlackDashPen)
pBox(0).y=(rect.bottom-((rect.bottom+rect.top)/2+Margin)-2*Margin-
4)/2+((rect.bottom+rect.top)/2+Margin)+Margin+2
pBox(1).y=pBox(0).y
Polyline(mDC, @pBox(0), 2)
TextOut(mDC, 0,pBox(0).y+3,Str(Avg), Len(Str(Avg)))

SelectObject(mDC, BlackPen)
Polyline(mDC, @pArray(0), DepthxBuff)


' Draw the IV result
SelectObject(mDC, BlackThickPen)
TextOut(mDC, rect.left+3,rect.top+4,Str(HResult), Len(Str(HResult)))
Rectangle(mDC, rect.left+3, rect.top+Margin+2, rect.right-3, (rect.bottom+rect.top)/2-Margin)
TextOut(mDC, rect.left, (rect.bottom+rect.top)/2-Margin+2, "0", 1)
TextOut(mDC, rect.right-3-8*Len(Str(VBound)), (rect.bottom+rect.top)/2-Margin+2,
Str(VBound), Len(Str(VBound)))

SelectObject(mDC, BlackPen)
For i =1 To vi-1
pArray(i).x=i*(rect.right-5-rect.left-5)/(StepLIV-1)+rect.left+5
pArray(i).y=(       xResult(i)-HResult)/(-HResult)*((rect.bottom+rect.top)/2-Margin-rect.top-
Margin-2-4)+rect.top+Margin+2+1
Ellipse(mDC, pArray(i).x-PointSize, pArray(i).y-PointSize, pArray(i).x+PointSize,
pArray(i).y+PointSize)
Next
Polyline(mDC, @pArray(1), vi-1)

SelectObject(mDC, BlackDashPen)
pBox(0).x=rect.left+5
pBox(1).x=rect.right-5
pBox(0).y=(rect.top+Margin+2+(rect.bottom+rect.top)/2-Margin)/2
pBox(1).y=pBox(0).y
Polyline(mDC, @pBox(0), 2)
TextOut(mDC, pBox(0).x+2,pBox(0).y+3,Str(HResult/2), Len(Str(HResult/2)))
pBox(0).x=(rect.left+3+ rect.right-3)/2
pBox(1).x=pBox(0).x
pBox(0).y=rect.top+Margin+4
pBox(1).y=(rect.bottom+rect.top)/2-Margin-2
Polyline(mDC, @pBox(0), 2)
TextOut(mDC, pBox(0).x-4*Len(Str(VBound/2)), (rect.bottom+rect.top)/2-Margin+2,
Str(VBound/2), Len(Str(VBound/2)))
```

```
BitBlt(hDC,0,0,rect.right,rect.bottom,mDC,0,0,SRCCOPY)

End Sub

Sub UpodateIGBoard(ByVal hWin As HWND,ByVal hDC As HDC)
Dim rect As RECT
Dim num As Integer

If StepLIV>DepthxBuff Then num=StepLIV-1 Else num=DepthxBuff-1
Dim pArray(num) As Point
Dim pBox(5) As Point
Dim i As Integer


'Clean the whole thing
GetClientRect(hWin,@rect)
FillRect(mDC,@rect,GetStockObject(WHITE_BRUSH))

'Draw the instant buffer output
For i =0 To DepthxBuff-1
pArray(i).x=i*(rect.right-rect.left)/(DepthxBuff-1)+rect.left
pArray(i).y=(xBuff(i)-Avg-Boundary)/(-2*Boundary)*(rect.bottom-
((rect.bottom+rect.top)/2+20)-2*Margin-4)+((rect.bottom+rect.top)/2+Margin)+Margin+2
Next


SelectObject(mDC, BlackThickPen)
pBox(0).x=rect.left
pBox(0).y=((rect.bottom+rect.top)/2+Margin)+Margin
pBox(1).x=rect.right
pBox(1).y=pBox(0).y
Polyline(mDC, @pBox(0), 2)
TextOut(mDC, 0,((rect.bottom+rect.top)/2+Margin),Str(Boundary/avg*100)+"%",
Len(Str(Boundary/avg*100)+"%"))

pBox(0).y=rect.Bottom-Margin
pBox(1).y=pBox(0).y
Polyline(mDC, @pBox(0), 2)
TextOut(mDC, 0,pBox(0).y+3,Str(-Boundary/avg*100)+"%", Len(Str(-
Boundary/avg*100)+"%"))

SelectObject(mDC, BlackDashPen)
pBox(0).y=(rect.bottom-((rect.bottom+rect.top)/2+Margin)-2*Margin-
4)/2+((rect.bottom+rect.top)/2+Margin)+Margin+2
pBox(1).y=pBox(0).y
Polyline(mDC, @pBox(0), 2)
TextOut(mDC, 0,pBox(0).y+3,Str(Avg), Len(Str(Avg)))

SelectObject(mDC, BlackPen)
Polyline(mDC, @pArray(0), DepthxBuff)
```

```
' Draw the IG result
SelectObject(mDC, BlackThickPen)

Rectangle(mDC, rect.left+3, rect.top+Margin+2, rect.right-3, (rect.bottom+rect.top)/2-Margin)
TextOut(mDC, rect.left, (rect.bottom+rect.top)/2-Margin+2, Str(GIBound), Len(Str(GIBound)))
TextOut(mDC, rect.right-3-8*Len(Str(GFBound)), (rect.bottom+rect.top)/2-Margin+2,
Str(GFBound), Len(Str(GFBound)))

SelectObject(mDC, BlackPen)
For i =0 To vi-1
pArray(i).x=i*(rect.right-5-rect.left-5)/(StepIG-1)+rect.left+5
pArray(i).y=(       xResult(i)-HResult)/(-HResult)*((rect.bottom+rect.top)/2-Margin-rect.top-
Margin-2-4)+rect.top+Margin+2+1
Ellipse(mDC, pArray(i).x-PointSize, pArray(i).y-PointSize, pArray(i).x+PointSize,
pArray(i).y+PointSize)
Next
Polyline(mDC, @pArray(0), vi)

SelectObject(mDC, BlackDashPen)
pBox(0).x=rect.left+5
pBox(1).x=rect.right-5
pBox(0).y=(rect.top+Margin+2+(rect.bottom+rect.top)/2-Margin)/2
pBox(1).y=pBox(0).y
Polyline(mDC, @pBox(0), 2)
TextOut(mDC, (rect.left+3+ rect.right-3)/2+3,pBox(0).y+3,Str(HResult/2), Len(Str(HResult/2)))
pBox(0).x=(rect.left+3+ rect.right-3)/2
pBox(1).x=pBox(0).x
pBox(0).y=rect.top+Margin+4
pBox(1).y=(rect.bottom+rect.top)/2-Margin-2
Polyline(mDC, @pBox(0), 2)
TextOut(mDC, pBox(0).x-4, (rect.bottom+rect.top)/2-Margin+2, "0", 1)
TextOut(mDC, pBox(0).x+3,rect.top+4,Str(HResult), Len(Str(HResult)))

BitBlt(hDC,0,0,rect.right,rect.bottom,mDC,0,0,SRCCOPY)

End Sub

Sub UpodateTSBoard(ByVal hWin As HWND,ByVal hDC As HDC)
Dim rect As RECT
Dim num As Integer

If StepTS>DepthxBuff Then num=StepTS-1 Else num=DepthxBuff-1
Dim pArray(num) As Point
Dim pBox(5) As Point
Dim i As Integer


'Clean the whole thing
GetClientRect(hWin,@rect)
FillRect(mDC,@rect,GetStockObject(WHITE_BRUSH))

'Draw the instant buffer output
For i =0 To DepthxBuff-1
```

```
pArray(i).x=i*(rect.right-rect.left)/(DepthxBuff-1)+rect.left
pArray(i).y=(xBuff(i)-Avg-Boundary)/(-2*Boundary)*(rect.bottom-
((rect.bottom+rect.top)/2+20)-2*Margin-4)+((rect.bottom+rect.top)/2+Margin)+Margin+2
Next


SelectObject(mDC, BlackThickPen)
pBox(0).x=rect.left
pBox(0).y=((rect.bottom+rect.top)/2+Margin)+Margin
pBox(1).x=rect.right
pBox(1).y=pBox(0).y
Polyline(mDC, @pBox(0), 2)
TextOut(mDC, 0,((rect.bottom+rect.top)/2+Margin),Str(Boundary/avg*100)+"%",
Len(Str(Boundary/avg*100)+"%"))

pBox(0).y=rect.Bottom-Margin
pBox(1).y=pBox(0).y
Polyline(mDC, @pBox(0), 2)
TextOut(mDC, 0,pBox(0).y+3,Str(-Boundary/avg*100)+"%", Len(Str(-
Boundary/avg*100)+"%"))

SelectObject(mDC, BlackDashPen)
pBox(0).y=(rect.bottom-((rect.bottom+rect.top)/2+Margin)-2*Margin-
4)/2+((rect.bottom+rect.top)/2+Margin)+Margin+2
pBox(1).y=pBox(0).y
Polyline(mDC, @pBox(0), 2)
TextOut(mDC, 0,pBox(0).y+3,Str(Avg), Len(Str(Avg)))

SelectObject(mDC, BlackPen)
Polyline(mDC, @pArray(0), DepthxBuff)


' Draw the TS result
SelectObject(mDC, BlackThickPen)

Rectangle(mDC, rect.left+3, rect.top+Margin+2, rect.right-3, (rect.bottom+rect.top)/2-Margin)
TextOut(mDC, rect.left, (rect.bottom+rect.top)/2-Margin+2, Str(0), Len(Str(0)))
TextOut(mDC, rect.right-3-8*Len(Str(VStep(vi-1)-VStep(0))), (rect.bottom+rect.top)/2-
Margin+2, Str(VStep(vi-1)-VStep(0)), Len(Str(VStep(vi-1)-VStep(0))))

SelectObject(mDC, BlackPen)
For i =0 To vi-1
pArray(i).x=i*(rect.right-5-rect.left-5)/vi+rect.left+5
pArray(i).y=(	xResult(i)-HResult)/(-HResult)*((rect.bottom+rect.top)/2-Margin-rect.top-
Margin-2-4)+rect.top+Margin+2+1
Ellipse(mDC, pArray(i).x-PointSize, pArray(i).y-PointSize, pArray(i).x+PointSize,
pArray(i).y+PointSize)
Next
Polyline(mDC, @pArray(0), vi)

SelectObject(mDC, BlackDashPen)
pBox(0).x=rect.left+5
pBox(1).x=rect.right-5
```

```
pBox(0).y=(rect.top+Margin+2+(rect.bottom+rect.top)/2-Margin)/2
pBox(1).y=pBox(0).y
Polyline(mDC, @pBox(0), 2)
TextOut(mDC, pBox(0).x+2,pBox(0).y+3,Str(HResult/2), Len(Str(HResult/2)))
TextOut(mDC, pBox(0).x+2,rect.top+3,Str(HResult), Len(Str(HResult)))
pBox(0).x=(rect.left+3+ rect.right-3)/2
pBox(1).x=pBox(0).x
pBox(0).y=rect.top+Margin+4
pBox(1).y=(rect.bottom+rect.top)/2-Margin-2
Polyline(mDC, @pBox(0), 2)

BitBlt(hDC,0,0,rect.right,rect.bottom,mDC,0,0,SRCCOPY)

End Sub

Sub UpodateTSBoardInstant(ByVal hWin As HWND,ByVal hDC As HDC)
Dim rect As RECT
Dim num As Integer

Dim pArray(vi-1) As Point
Dim pBox(5) As Point
Dim i As Integer


'Clean the whole thing
GetClientRect(hWin,@rect)
FillRect(mDC,@rect,GetStockObject(WHITE_BRUSH))

'Draw the instant buffer output
For i =0 To vi-1
pArray(i).x=i*(rect.right-rect.left)/(vi-1)+rect.left
pArray(i).y=(xResult(i)-Avg-Boundary)/(-2*Boundary)*(rect.bottom-
((rect.bottom+rect.top)/2+20)-2*Margin-4)+((rect.bottom+rect.top)/2+Margin)+Margin+2
Next


SelectObject(mDC, BlackThickPen)
pBox(0).x=rect.left
pBox(0).y=((rect.bottom+rect.top)/2+Margin)+Margin
pBox(1).x=rect.right
pBox(1).y=pBox(0).y
Polyline(mDC, @pBox(0), 2)
TextOut(mDC, 0,((rect.bottom+rect.top)/2+Margin),Str(Boundary/avg*100)+"%",
Len(Str(Boundary/avg*100)+"%"))

pBox(0).y=rect.Bottom-Margin
pBox(1).y=pBox(0).y
Polyline(mDC, @pBox(0), 2)
TextOut(mDC, 0,pBox(0).y+3,Str(-Boundary/avg*100)+"%", Len(Str(-
Boundary/avg*100)+"%"))

SelectObject(mDC, BlackDashPen)
```

```
pBox(0).y=(rect.bottom-((rect.bottom+rect.top)/2+Margin)-2*Margin-
4)/2+((rect.bottom+rect.top)/2+Margin)+Margin+2
pBox(1).y=pBox(0).y
Polyline(mDC, @pBox(0), 2)
TextOut(mDC, 0,pBox(0).y+3,Str(Avg), Len(Str(Avg)))

SelectObject(mDC, BlackPen)
Polyline(mDC, @pArray(0), vi)

BitBlt(hDC,0,0,rect.right,rect.bottom,mDC,0,0,SRCCOPY)

End Sub


Function BoardProc(ByVal hWin As HWND,ByVal uMsg As UINT,ByVal wParam As
WPARAM,ByVal lParam As LPARAM) As Integer
Dim ps As PAINTSTRUCT

If uMsg=WM_PAINT Then
BeginPaint(hWin,@ps)
Select Case IVorIGorTS
Case 0 ' IV
UpodateIVBoard(hWin,ps.hdc)

Case 1 ' IG
UpodateIGBoard(hWin,ps.hdc)

Case 2 ' TS
UpodateTSBoardInstant(hWin,ps.hdc)

End Select
EndPaint(hWin,@ps)
Return 0
EndIf
Return CallWindowProc(lpOldBoardProc,hWin,uMsg,wParam,lParam)

End Function

Sub TimerProc(ByVal hWin As HWND,ByVal uMsg As UINT,ByVal wParam As
WPARAM,ByVal lParam As LPARAM)
If Pause=TRUE Then Exit Sub
Dim i As Integer, temp As Double, TimeTemp As Double
Static count As Integer
'(GetForegroundWindow())
SendComm "REST", WaitComm
SendComm "SRAT"+Str(Rate), WaitComm '            Rate=CInt(Log(Actual rate)/Log(2))+4
SendComm "STRT", CInt(DepthxBuff*1000/2^(Rate-4.5))
TimeTemp=Timer
SendComm "PAUS", WaitComm
TimeTemp=(Timer+TimeTemp)/2
Query "SPTS?", temp

'hWin=GetForegroundWindow()
```

```
'KillTimer(hWin, IDT_Timer1)
'MessageBox (hWin, ("TRCL? 1,"+Str(CInt(temp-DepthxBuff))+","+Str(CInt(DepthxBuff))),
"Debug", MB_OK)


Query ("TRCL? 1,"+Str(CInt(temp-DepthxBuff))+","+Str(CInt(DepthxBuff)), @xBuff(0),
DepthxBuff)

MaxValue=xBuff(0)
MinValue=MaxValue
Avg=MaxValue

For i =1 To DepthxBuff-1
If MinValue>xBuff(i) Then MinValue=xBuff(i)
If MaxValue<xBuff(i) Then MaxValue=xBuff(i)
Avg+=xBuff(i)
Next
Avg/=DepthxBuff

If MaxValue=MinValue Then
Boundary=Avg*BoundaryPass*0.1
ElseIf (MaxValue-Avg)>=(Avg-MinValue) Then
Boundary=(MaxValue-Avg)
Else
Boundary=(Avg-MinValue)
EndIf

InvalidateRect(hShp,NULL,TRUE)

Select Case IVorIGorTS
Case 0 ' IV
If Boundary<=Avg*BoundaryPass Then
If vi>0 Then
xResult(vi)=Avg
If HResult<xResult(vi) Then HResult=xResult(vi)
Query ("TRCL? 2,"+Str(CInt(temp-DepthxBuff))+","+Str(CInt(DepthxBuff)), @yBuff(0),
DepthxBuff)
yResult(vi)=0
For i =1 To DepthxBuff-1
yResult(vi)+=yBuff(i)
Next
yResult(vi)/=DepthxBuff
EndIf

vi=vi+1
If vi=StepLIV Then
' Collection is done
Pause=TRUE
Do
Query "SLVL?", temp
If Abs(VStep(1)-temp)>0.1 Then SendComm "SLVL"+Str(temp+Sgn(VStep(1)-temp)*0.1),
SleepTime
Loop Until Abs(VStep(1)-temp)<=0.1
```

```
SendComm "SLVL"+Str(VStep(1)), SleepTime
Else ' NextV
If vi=1 Then
Do
Query "SLVL?", temp
If Abs(VStep(vi)-temp)>0.1 Then SendComm "SLVL"+Str(temp+Sgn(VStep(vi)-temp)*0.1),
SleepTime
Loop Until Abs(VStep(vi)-temp)<=0.1
End If
SendComm "SLVL"+Str(VStep(vi)), SleepTime
EndIf
EndIf

Case 1 ' IG
If Boundary<=Avg*BoundaryPass Then
If vi>=0 Then
xResult(vi)=Avg
If HResult<xResult(vi) Then HResult=xResult(vi)
Query ("TRCL? 2,"+Str(CInt(temp-DepthxBuff))+","+Str(CInt(DepthxBuff)), @yBuff(0),
DepthxBuff)
yResult(vi)=0
For i =1 To DepthxBuff-1
yResult(vi)+=yBuff(i)
Next
yResult(vi)/=DepthxBuff
EndIf
vi=vi+1

If vi=StepIG Then
' Collection is done
Pause=TRUE
Do
Query "AUXV? 1", temp
If Abs(0-temp)>0.5 Then SendComm "AUXV 1,"+Str(temp+Sgn(0-temp)*0.5), SleepTime
Loop Until Abs(0-temp)<0.5
SendComm "AUXV 1,0", SleepTime
Else ' NextV
If vi=0 Then
Do
Query "AUXV? 1", temp
If Abs(VStep(vi)-temp)>0.5 Then SendComm "AUXV 1,"+Str(temp+Sgn(VStep(vi)-temp)*0.5),
SleepTime
Loop Until Abs(VStep(vi)-temp)<=0.5
End If
SendComm "AUXV 1,"+Str(VStep(vi)), SleepTime
EndIf
EndIf

Case 2 ' TS
If Boundary<=Avg*BoundaryPass Then
If vi>=0 Then
VStep(vi)=TimeTemp
xResult(vi)=Avg
```

```
If HResult<xResult(vi) Then HResult=xResult(vi)
Query ("TRCL? 2,"+Str(CInt(temp-DepthxBuff))+","+Str(CInt(DepthxBuff)), @yBuff(0),
DepthxBuff)
yResult(vi)=0
For i =1 To DepthxBuff-1
yResult(vi)+=yBuff(i)
Next
yResult(vi)/=DepthxBuff
EndIf

If vi=StepTS Then
' Collection is done
Pause=TRUE
Else
vi=vi+1
EndIf
EndIf
End Select

End Sub

Sub TimerProcTS(ByVal hWin As HWND,ByVal uMsg As UINT,ByVal wParam As
WPARAM,ByVal lParam As LPARAM)
If Pause=TRUE Then Exit Sub
Pause=TRUE
Dim i As Integer, temp As Double, TimeTemp As Double
Static count As Integer
'(GetForegroundWindow())
SendComm "REST", WaitComm
SendComm "SRAT"+Str(Rate), WaitComm '            Rate=CInt(Log(Actual rate)/Log(2))+4
SendComm "STRT", CInt(1+StepTS*1000/2^(Rate-4))
SendComm "PAUS", WaitComm
Query "SPTS?", temp

'hWin=GetForegroundWindow()
'KillTimer(hWin, IDT_Timer1)
'MessageBox (hWin, ("TRCL? 1,"+Str(CInt(temp-DepthxBuff))+","+Str(CInt(DepthxBuff))),
"Debug", MB_OK)
If temp >= StepTS Then temp =StepTS

Query ("TRCL? 1,0,"+Str(temp-1), @xResult(0), temp-1)

MaxValue=xResult(0)
MinValue=MaxValue
Avg=MaxValue

For i =0 To temp-1
If MinValue>xResult(i) Then MinValue=xResult(i)
If MaxValue<xResult(i) Then MaxValue=xResult(i)
Avg+=xResult(i)
Next
Avg/=temp
```

```
If MaxValue=MinValue Then
Boundary=Avg*BoundaryPass*0.1
ElseIf (MaxValue-Avg)>=(Avg-MinValue) Then
Boundary=(MaxValue-Avg)
Else
Boundary=(Avg-MinValue)
EndIf


Query ("TRCL? 2,0,"+Str(temp-1), @yResult(0), temp-1)
For i = 0 To temp-2
VStep(i)=i/2.0^(Rate-4)
Next
vi=temp-1

InvalidateRect(hShp,NULL,TRUE)
KillTimer(hWinTimer, IDT_Timer1)

End Sub

Function DlgProc(ByVal hWin As HWND,ByVal uMsg As UINT,ByVal wParam As
WPARAM,ByVal lParam As LPARAM) As Integer
Dim As Long id, Event, x, y
Dim hBtn As HWND
Dim hBmp As HBITMAP
Dim hDC As HDC
Dim rect As RECT
Dim i As Integer, l As Integer, h As Integer
Dim TempString As String
Dim temp As Double


Select Case uMsg
Case WM_INITDIALOG
hShp=GetDlgItem(hWin,IDC_SHP1)
hDC=GetDC(hShp)
mDC=CreateCompatibleDC(hDC)
GetClientRect(hShp,@rect)
hBmp=CreateCompatibleBitmap(hDC,rect.right,rect.bottom)
hOldBmp=SelectObject(mDC,hBmp)
lpOldBoardProc=Cast(Any
Ptr,SetWindowLong(hShp,GWL_WNDPROC,Cast(Integer,@BoardProc)))        'SetupBoard
IVorIGorTS=0
VBound=DefVBound
StepLIV=DefStepLIV
SleepTime=DefSleepTime
GIBound=DefGIBound
GFBound=DefGFBound
StepIG=DefStepIG
BoundaryPass=DefBoundaryPass
DepthxBuff=DefDepthxBuff
Rate=DefRate
GBias=DefGBias
```

```
DSBias=DefDSBias
TSDSBias=DefTSDSBias
TSGBias=DefTSGBias
StepTS=DefStepTS
'
Case WM_CLOSE
EndDialog(hWinPara, 0)
EndDialog(hWin, 0)
'
Case WM_COMMAND
id=LoWord(wParam)
Event=HiWord(wParam)
Select Case id
Case IDC_BTN1
DialogBoxParam(hInstance, Cast(ZString Ptr,IDD_DLG2), NULL, @DlgProc2, NULL)

'
Case IDC_BTN2
If hWinTimer<>0 Then
KillTimer(hWinTimer, IDT_Timer1)
hWinTimer=0
EndIf
For i =0 To StepLIV-1
VStep(i)=VBound*i/(StepLIV-1)
Next
For i =0 To DepthxBuff-1
xBuff(i)=0
Next
Avg=1
Boundary=Avg*BoundaryPass
IVorIGorTS=0
HResult=0
vi=0
Pause=FALSE
hWinTimer=hWin
Do
Query "AUXV? 1", temp
If Abs(GBias-temp)>0.5 Then SendComm "AUXV 1,"+Str(temp+Sgn(GBias-temp)*0.5),
SleepTime
Loop Until Abs(GBias-temp)<=0.5
SendComm "AUXV 1,"+Str(GBias), SleepTime
SetTimer(hWin,IDT_Timer1,MTIMER,Cast(Any Ptr,@TimerProc))
'
Case IDC_BTN3
If Pause=TRUE Then Pause=FALSE Else Pause=TRUE
'
Case IDC_BTN4
If hWinTimer<>0 Then
KillTimer(hWinTimer, IDT_Timer1)
hWinTimer=0
EndIf
For i =0 To StepIG-1
VStep(i)=i*(GFBound-GIBound)/(StepIG-1)+GIBound
```

```
Next
For i =0 To DepthxBuff-1
xBuff(i)=0
Next
Avg=1
Boundary=Avg*BoundaryPass
IVorIGorTS=1
HResult=0
vi=-1
Pause=FALSE
hWinTimer=hWin
Do
Query "SLVL?", temp
If Abs(DSBias-temp)>0.1 Then SendComm "SLVL"+Str(temp+Sgn(DSBias-temp)*0.1),
SleepTime
Loop Until Abs(DSBias-temp)<=0.1
SendComm "SLVL"+Str(DSBias), SleepTime
SetTimer(hWin,IDT_Timer1,MTIMER,Cast(Any Ptr,@TimerProc))
'
Case IDC_BTN5
If (IVorIGorTS=0 And vi=StepLIV) Or (IVorIGorTS=1 And vi=StepIG) Or (IVorIGorTS=2 And
Pause=TRUE)Then
'If hWinTimer<>0 Then
'           KillTimer(hWinTimer, IDT_Timer1)
'           hWinTimer=0
'EndIf
Filename=SaveFile(GetForegroundWindow())
Select Case IVorIGorTS
Case 0 ' IV
l=1:h=StepLIV-1
TempString="DS Bias (Vrms):"

Case 1 ' IG
l=0:h=StepIG-1
TempString="Gate DC Bias (V):"
Case 2 ' TS
l=0:h=vi-1
TempString="Time (sec):"

End Select

'
FileNum=FreeFile()
Open Filename For Output As #FileNum
Print #FileNum, "Data Collecting";!"\t\t\t\t";"IV Curve";!"\t\t\t";"Gate Curve";!"\t\t\t\t";"Time
Serious"
Print #FileNum, "Pause (ms):";!"\t";"Fluctuation (%):";!"\t";"Average:";!"\t";"Sample rate
(Hz):";!"\t";"DS Bias Range (V):";!"\t";"Number of Steps:";!"\t";"Gate Bias (V):";!"\t";"Initial
Gate Bias (V):";!"\t";"Final Gate Bias (V):";!"\t";"Number of Steps:";!"\t";"DS Bias
(V):";!"\t";"DS Bias (V):";!"\t";"Gate Bias (V):";!"\t";"Number of Steps:";!"\t";"Frequency"
Print #FileNum,
Str(SleepTime);!"\t";Str(BoundaryPass*100)+"%";!"\t";Str(DepthxBuff);!"\t";Str(2^(Rate-
4));!"\t";Str(VBound);!"\t";Str(StepLIV);!"\t";Str(GBias);!"\t";Str(GIBound);!"\t";Str(GFBound);!
```

```
"\t";Str(StepIG);!"\t";Str(DSBias);!"\t";Str(TSDSBias);!"\t";Str(TSGBias);!"\t";Str(StepTS);!"\t";
Str(Freq)
Print #FileNum, ""
Print #FileNum, TempString;!"\t";
Query("DDEF? 1", TempString)
Select Case Mid(TempString,1,1)
Case "0": TempString="X"
Case "1": TempString="R"
Case "2": TempString="X noise"
Case "3": TempString="Aux In 1"
Case "4": TempString="Aux In 2"
Case Else: TempString="Unknown"
End Select
Print #FileNum, TempString;!"\t";
Query("DDEF? 2", TempString)
Select Case Mid(TempString,1,1)
Case "0": TempString="Y"
Case "1": TempString="Angle"
Case "2": TempString="Y noise"
Case "3": TempString="Aux In 1"
Case "4": TempString="Aux In 2"
Case Else: TempString="Unknown"
End Select
Print #FileNum, TempString
For i=l To h
Print #FileNum, Str(VStep(i));!"\t";Str(xResult(i));!"\t";Str(yResult(i))
Next
Close #FileNum
Else
MessageBox (hWin, "Recording is not done yet or not even started yet.", "Error:", MB_OK)
EndIf
'
Case IDC_BTN8
If hWinTimer<>0 Then
KillTimer(hWinTimer, IDT_Timer1)
hWinTimer=0
EndIf
Avg=1
Boundary=Avg*BoundaryPass
IVorIGorTS=2
vi=0
Pause=FALSE
hWinTimer=hWin
Do
Query "SLVL?", temp
If Abs(TSDSBias-temp)>0.1 Then SendComm "SLVL"+Str(temp+Sgn(TSDSBias-temp)*0.1),
SleepTime
Loop Until Abs(TSDSBias-temp)<=0.1
SendComm "SLVL"+Str(TSDSBias), SleepTime
Do
Query "AUXV? 1", temp
If Abs(TSGBias-temp)>0.5 Then SendComm "AUXV 1,"+Str(temp+Sgn(TSGBias-temp)*0.5),
SleepTime
```

```
Loop Until Abs(TSGBias-temp)<=0.5
SendComm "AUXV 1,"+Str(TSGBias), SleepTime

SetTimer(hWin,IDT_Timer1,MTIMER,Cast(Any Ptr,@TimerProcTS))
'
End Select
Case WM_SIZE
/'GetClientRect(hWin,@rect)
hBtn=GetDlgItem(hWin,IDC_BTN1)
x=rect.right-100
y=rect.bottom-35
MoveWindow(hBtn,x,y,97,31,TRUE)'/
'
Case Else
Return FALSE
'
End Select
Return TRUE

End Function

Sub Query (Comm As String, pBuff As Double Pointer, num As Integer)
Dim i As Integer, m As Short, e As UShort, char As String*1, LastTimer As Double
Print #Comport , Comm
Sleep WaitComm
For i=0 To num-1
If Eof(Comport)=-1 Then
Exit Sub
End If
Get #Comport,,m
Get #Comport,,e
*(pBuff+i)=m*2^(e-124)
Next

Do While (Eof(Comport)=0)
Get #Comport,,char
LastTimer = Timer
Do
Loop Until Abs(Timer - LastTimer) > WaitTras
Loop
End Sub

Sub Query (Comm As String, v1 As String)
Dim t(3) As String, i As Integer, char As String*1, LastTimer As Double
Print #Comport , Comm
Sleep WaitComm
i=0
Do While (Eof(Comport)=0)
Do
Get #Comport,,char
Loop Until Len(char)<>0
If (char=Chr(13)) Then
i=i+1
```

```
If i > 1 Then
Do While (Eof(Comport)=0)
Get #Comport,,char
Loop
EndIf
Else
t(i)=t(i)+char
LastTimer = Timer
Do
Loop Until Abs(Timer - LastTimer) > WaitTras
EndIf
Loop
v1=t(0)
End Sub
Sub Query (Comm As String, ByRef v1 As Double)
Dim t(3) As String, i As Integer, char As String*1, LastTimer As Double
Print #Comport , Comm
Sleep WaitComm
i=0
Do While (Eof(Comport)=0)
Do
Get #Comport,,char
Loop Until Len(char)<>0
If (char=Chr(13)) Then
i=i+1
If i > 1 Then
Do While (Eof(Comport)=0)
Get #Comport,,char
Loop
EndIf
Else
t(i)=t(i)+char
LastTimer = Timer
Do
Loop Until Abs(Timer - LastTimer) > WaitTras
EndIf
Loop
v1=Val(t(0))
End Sub
Sub Query (Comm As String, ByRef v1 As Double, ByRef v2 As Double)
Dim t(3) As String, i As Integer, char As String*1, LastTimer As Double
Print #Comport , Comm
Sleep WaitComm
i=0
Do While (Eof(Comport)=0)
Do
Get #Comport,,char
Loop Until Len(char)<>0
If (char=Chr(13)) Then
i=i+1
If i > 2 Then
Do While (Eof(Comport)=0)
Get #Comport,,char
```

```
Loop
EndIf
Else
t(i)=t(i)+char
LastTimer = Timer
Do
Loop Until Abs(Timer - LastTimer) > WaitTras
EndIf
Loop
v1=Val(t(0))
v2=Val(t(1))
End Sub
Sub Query (Comm As String, ByRef v1 As Double, ByRef v2 As Double, ByRef v3 As Double)
Dim t(3) As String, i As Integer, char As String*1, LastTimer As Double
Print #Comport , Comm
Sleep WaitComm
i=0
Do While (Eof(Comport)=0)
Do
Get #Comport,,char
Loop Until Len(char)<>0
If (char=Chr(13)) Then
i=i+1
If i > 3 Then
Do While (Eof(Comport)=0)
Get #Comport,,char
Loop
EndIf
Else
t(i)=t(i)+char
LastTimer = Timer
Do
Loop Until Abs(Timer - LastTimer) > WaitTras
EndIf
Loop
v1=Val(t(0))
v2=Val(t(1))
v3=Val(t(2))
End Sub
Sub Query (Comm As String, ByRef v1 As Double, ByRef v2 As Double, ByRef v3 As Double,
ByRef v4 As Double)
Dim t(3) As String, i As Integer, char As String*1, LastTimer As Double
Print #Comport , Comm
Sleep WaitComm
i=0
Do While (Eof(Comport)=0)
Do
Get #Comport,,char
Loop Until Len(char)<>0
If (char=Chr(13)) Then
i=i+1
If i > 4 Then
Do While (Eof(Comport)=0)
```

```
Get #Comport,,char
Loop
EndIf
Else
t(i)=t(i)+char
LastTimer = Timer
Do
Loop Until Abs(Timer - LastTimer) > WaitTras
EndIf
Loop
v1=Val(t(0))
v2=Val(t(1))
v3=Val(t(2))
v4=Val(t(3))
End Sub

Sub SendComm(Comm As String, Pause As Integer)
Print #Comport , Comm
If pause=0 Then Pause=1
Sleep Pause
End Sub

Function SaveFile(ByVal hWin As HWND) As String
Dim ofn As OPENFILENAME
Dim buff As ZString*260
'ZeroMemory(&ofn, sizeof(OPENFILENAME))
ofn.lStructSize=SizeOf(OPENFILENAME)
ofn.hwndOwner=hWin
ofn.hInstance=hInstance
'ofn.lpstrInitialDir=StrPtr("C:\")
buff=String(260,0)
ofn.lpstrFile=@buff
ofn.nMaxFile=260
ofn.lpstrFilter=StrPtr(szFilter)
Select Case IVorIGorTS
Case 0 ' IV
ofn.lpstrTitle=StrPtr("Save IV curve:")

Case 1 ' IG
ofn.lpstrTitle=StrPtr("Save Gate curve:")

Case 2 ' TS
ofn.lpstrTitle=StrPtr("Save Time Serious:")
End Select

ofn.Flags=OFN_PATHMUSTEXIST Or OFN_HIDEREADONLY Or OFN_EXPLORER
If GetSaveFileName(@ofn) Then
Return buff
EndIf
End Function

Function DlgProc2(ByVal hWin As HWND,ByVal uMsg As UINT,ByVal wParam As
WPARAM,ByVal lParam As LPARAM) As Integer
```

```
Dim As Long id, Event, x, y
Dim hBtn As HWND
Dim hBmp As HBITMAP
Dim hDC As HDC
Dim rect As RECT
Dim i As Integer, l As Integer, h As Integer
Dim buff As ZString*22


Select Case uMsg
Case WM_INITDIALOG
hWinPara=hWin
SetDlgItemText(hWin, IDC_EDT8, Str(SleepTime))
SetDlgItemText(hWin, IDC_EDT7, Digi(BoundaryPass*100, 2)+"%")
SetDlgItemText(hWin, IDC_EDT4, Str(DepthxBuff))
SetDlgItemText(hWin, IDC_EDT3, Str(2^(Rate-4)))
SetDlgItemText(hWin, IDC_EDT2, Str(VBound))
SetDlgItemText(hWin, IDC_EDT1, Str(StepLIV))
SetDlgItemText(hWin, IDC_EDT9, Str(GBias))
SetDlgItemText(hWin, IDC_EDT5, Str(GIBound))
SetDlgItemText(hWin, IDC_EDT11, Str(GFBound))
SetDlgItemText(hWin, IDC_EDT6, Str(StepIG))
SetDlgItemText(hWin, IDC_EDT10, Str(DSBias))
SetDlgItemText(hWin, IDC_EDT14, Str(TSDSBias))
SetDlgItemText(hWin, IDC_EDT13, Str(TSGBias))
SetDlgItemText(hWin, IDC_EDT12, Str(StepTS))
'
Case WM_CLOSE
EndDialog(hWin, 0)
'
Case WM_COMMAND
id=LoWord(wParam)
Event=HiWord(wParam)
Select Case id
Case IDC_BTN6
GetDlgItemText(hWin, IDC_EDT8, @buff, 22)
SleepTime=Val(buff)

GetDlgItemText(hWin, IDC_EDT7, @buff, 22)
BoundaryPass=Val(buff)/100
SetDlgItemText(hWin, IDC_EDT7, Digi(BoundaryPass*100, 2)+"%")

GetDlgItemText(hWin, IDC_EDT4, @buff, 22)
DepthxBuff=Val(buff)

GetDlgItemText(hWin, IDC_EDT2, @buff, 22)
VBound=Val(buff)

GetDlgItemText(hWin, IDC_EDT1, @buff, 22)
StepLIV=Val(buff)

GetDlgItemText(hWin, IDC_EDT9, @buff, 22)
GBias=Val(buff)
```

```
GetDlgItemText(hWin, IDC_EDT5, @buff, 22)
GIBound=Val(buff)

GetDlgItemText(hWin, IDC_EDT11, @buff, 22)
GFBound=Val(buff)

GetDlgItemText(hWin, IDC_EDT6, @buff, 22)
StepIG=Val(buff)

GetDlgItemText(hWin, IDC_EDT10, @buff, 22)
DSBias=Val(buff)

GetDlgItemText(hWin, IDC_EDT3, @buff, 22)
i=CInt(Log(Val(buff))/Log(2))+4
If i>13 Then i =13
If i<4 Then i=4
Rate=i
If Val(buff)<> 2^(Rate-4) Then SetDlgItemText(hWin, IDC_EDT3, Str(2^(Rate-4))) Else
EndDialog(hWin, 0)

GetDlgItemText(hWin, IDC_EDT14, @buff, 22)
TSDSBias=Val(buff)

GetDlgItemText(hWin, IDC_EDT13, @buff, 22)
TSGBias=Val(buff)

GetDlgItemText(hWin, IDC_EDT12, @buff, 22)
StepTS=Val(buff)

'MessageBox (hWin, @buff, "Display value of IDC_EDT1:", MB_OK)
'
Case IDC_BTN7
VBound=DefVBound
StepLIV=DefStepLIV
SleepTime=DefSleepTime
GIBound=DefGIBound
GFBound=DefGFBound
StepIG=DefStepIG
BoundaryPass=DefBoundaryPass
DepthxBuff=DefDepthxBuff
Rate=DefRate
GBias=DefGBias
DSBias=DefDSBias
TSDSBias=DefTSDSBias
TSGBias=DefTSGBias
StepTS=DefStepTS
SetDlgItemText(hWin, IDC_EDT8, Str(SleepTime))
SetDlgItemText(hWin, IDC_EDT7, Digi(BoundaryPass*100, 2)+"%")
SetDlgItemText(hWin, IDC_EDT4, Str(DepthxBuff))
SetDlgItemText(hWin, IDC_EDT3, Str(2^(Rate-4)))
SetDlgItemText(hWin, IDC_EDT2, Str(VBound))
SetDlgItemText(hWin, IDC_EDT1, Str(StepLIV))
```

```
SetDlgItemText(hWin, IDC_EDT9, Str(GBias))
SetDlgItemText(hWin, IDC_EDT5, Str(GIBound))
SetDlgItemText(hWin, IDC_EDT11, Str(GFBound))
SetDlgItemText(hWin, IDC_EDT6, Str(StepIG))
SetDlgItemText(hWin, IDC_EDT10, Str(DSBias))
SetDlgItemText(hWin, IDC_EDT14, Str(TSDSBias))
SetDlgItemText(hWin, IDC_EDT13, Str(TSGBias))
SetDlgItemText(hWin, IDC_EDT12, Str(StepTS))
'
End Select
Case WM_SIZE
Case Else
Return FALSE
'
End Select
Return TRUE
End Function

Function Digi(a As Double, b As Integer) As String
If Mid(Str(CInt(a*10^b)),Len(Str(CInt(a*10^b)))-b+1)="" Then
Return(Mid(Str(CInt(a*10^b)),1,Len(Str(CInt(a*10^b)))-b))
ElseIf Mid(Str(CInt(a*10^b)),Len(Str(CInt(a*10^b)))-b+1)=String(b,"0") Then
Return(Mid(Str(CInt(a*10^b)),1,Len(Str(CInt(a*10^b)))-b))
ElseIf Mid(Str(CInt(a*10^b)),1,Len(Str(CInt(a*10^b)))-b)="" Then
Return("0."+Mid(Str(CInt(a*10^b)),Len(Str(CInt(a*10^b)))-b+1))
Else
Return(Mid(Str(CInt(a*10^b)),1,Len(Str(CInt(a*10^b)))-
b)+"."+Mid(Str(CInt(a*10^b)),Len(Str(CInt(a*10^b)))-b+1))
End If
End Function
```